

AD-A257 291



WL-TR-92-2035

**HYDRODYNAMIC EFFECTS ON HEAT
TRANSFER FOR FILM-COOLED TURBINE BLADES**



DAVID G. BOGARD
KAREN A. THOLE
MICHAEL E. CRAWFORD
UNIVERSITY OF TEXAS
TURBULENCE & TURBINE COOLING RES. LAB.
AUSTIN, TX 78712

MAY 1992

FINAL REPORT FOR PERIOD 09/01/88--04/30-92

APPROVED FOR PUBLIC RELEASE; DISTRIBUTION IS UNLIMITED.

DTIC
S **E** **D**
ELECTE
OCT 29 1992

425717

92-28281



115
pg


AERO PROPULSION AND POWER DIRECTORATE
WRIGHT LABORATORY
AIR FORCE SYSTEMS COMMAND
WRIGHT-PATTERSON AFB OH 45433-6563

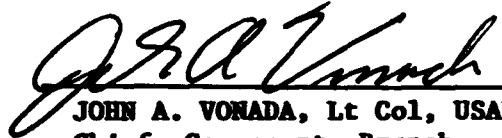
NOTICE

When Government drawings, specifications, or other data are used for any purpose other than in connection with a definitely Government-related procurement, the United States Government incurs no responsibility or any obligation whatsoever. The fact that the government may have formulated or in any way supplied the said drawings, specifications, or other data, is not to be regarded by implication, or otherwise in any manner construed, as licensing the holder, or any other person or corporation; or as conveying any rights or permission to manufacture, use, or sell any patented invention that may in any way be related thereto.

This report is releasable to the National Technical Information Service (NTIS). At NTIS, it will be available to the general public, including foreign nations.

This technical report has been reviewed and is approved for publication.


MATTHEW MEININGER
Project Engineer
Components Branch
Turbine Engine Division


JOHN A. VONADA, Lt Col, USAF
Chief, Components Branch
Turbine Engine Division
Aero Propulsion & Power
Directorate


ROBERT E. HENDERSON
Deputy for Technology
Turbine Engine Division
Aero Propulsion & Power Directorate

If your address has changed, if you wish to be removed from our mailing list, or if the addressee is no longer employed by your organization please notify WL/POTC, WPAFB, OH 45433-6563 to help us maintain a current mailing list.

Copies of this report should not be returned unless return is required by security considerations, contractual obligations, or notice on a specific document.

REPORT DOCUMENTATION PAGE			Form Approved OMB No. 0704-0188	
Public reporting burden for this collection of information is estimated to average 1 hour per response, including the time for reviewing instructions, searching existing data sources, gathering and maintaining the data needed, and completing and reviewing the collection of information. Send comments regarding this burden estimate or any other aspect of this collection of information, including suggestions for reducing this burden, to Washington Headquarters Services, Directorate for Information Operations and Reports, 1215 Jefferson Davis Highway, Suite 1204, Arlington, VA 22202-4302, and to the Office of Management and Budget, Paperwork Reduction Project (0704-0188), Washington, DC 20503.				
1. AGENCY USE ONLY (Leave blank)		2. REPORT DATE MAY 1992		3. REPORT TYPE AND DATES COVERED FINAL 09/01/88--04/30/92
4. TITLE AND SUBTITLE HYDRODYNAMIC EFFECTS ON HEAT TRANSFER FOR FILM-COOLED TURBINE BLADES			5. FUNDING NUMBERS C F33615-88-C-2830 PE 62203 PR 3066 TA 14 WU 17	
6. AUTHOR(S) DAVID G. BOGARD KAREN A. THOLE MICHAEL E. CRAWFORD				
7. PERFORMING ORGANIZATION NAME(S) AND ADDRESS(ES) UNIVERSITY OF TEXAS TURBULENCE & TURBINE COOLING RES. LAB. AUSTIN, TX 78712			8. PERFORMING ORGANIZATION REPORT NUMBER	
9. SPONSORING/MONITORING AGENCY NAME(S) AND ADDRESS(ES) AERO PROPULSION AND POWER DIRECTORATE WRIGHT LABORATORY WRIGHT PATTERSON AFB OH 45433 WL/POTC, Attn: MEININGER			10. SPONSORING/MONITORING AGENCY REPORT NUMBER WL-TR-92-2035	
11. SUPPLEMENTARY NOTES				
12a. DISTRIBUTION/AVAILABILITY STATEMENT APPROVED FOR PUBLIC RELEASE; DISTRIBUTION IS UNLIMITED.			12b. DISTRIBUTION CODE	
13. ABSTRACT (Maximum 200 words) <p>The objectives of this project were to develop a technique for generating very high freestream turbulence levels and to determine resulting effects on turbulent boundary layer and film cooling flows. Also, included in this project was the development of a simultaneous temperature/velocity measurement technique. All of these objectives were accomplished as described below; however, film cooling flows were studied only for minimal freestream turbulence levels.</p> <p>Several turbulence generating devices were studied to determine the maximum turbulence levels. Tests indicated that high velocity jets in cross-flow generated turbulence levels, Tu, which ranged from $Tu = 20\%$ to 11% over a 0.65 m distance. The turbulence integral length scales for this flow were on the order of boundary layer thickness.</p> <p>High freestream turbulence levels caused significant increases in surface heat flux. Various correlations for freestream turbulence affects on surface heat flux were evaluated. None of these correlations were adequate; however, with slight modifications two of the correlations reasonably collapsed the data.</p> <p>Thermal field measurements of simulated film cooling flows with a minimal freestream turbulence level indicated that the jet detachment/reattachment scaled with the momentum flux ratio.</p>				
14. SUBJECT TERMS TURBINES, FILM COOLING, TURBULENT FLOW, HEAT TRANSFER			15. NUMBER OF PAGES 115	
			16. PRICE CODE	
17. SECURITY CLASSIFICATION OF REPORT UNCLASSIFIED	18. SECURITY CLASSIFICATION OF THIS PAGE UNCLASSIFIED	19. SECURITY CLASSIFICATION OF ABSTRACT UNCLASSIFIED	20. LIMITATION OF ABSTRACT UL	

Table of Contents

	Page
List of Figures.....	iv
List of Tables.....	vii
Nomenclature	viii
Acknowledgements.....	x
1. Introduction.....	1
1.1 Air Force Turbine Heat Transfer Research Program	1
1.2 The University of Texas Turbine Cooling Research Program.....	2
1.3 Organization of the Report.....	4
2. Facilities Description and Qualification.....	6
2.1 Water Channel and Wind Tunnel Facilities.....	6
2.2 Measurement Apparatus and Data Acquisition Techniques.....	8
2.3 Qualification Tests of the Boundary Layer Wind Tunnel.....	11
3. Development of a Very High Turbulence Generator.....	17
3.1 Grid Turbulence.....	17
3.2 Delta Wing Array.....	22
3.3 High Velocity Jets in Cross-stream Configuration	25
3.4 High-Freestream Turbulence Wind Tunnel Tests.....	32
4. Development of a Simultaneous Temperature/Velocity Probe.....	42
4.1 Hot-wire/LDV Measurements.....	42
4.2 Cold-wire/LDV Measurements.....	43
5. Film Cooling Thermal Field	49
5.1 Facilities, Instrumentation, and Experimental Plan.....	49
5.2 Results and Conclusions.....	51
6. Effect of Very High Freestream Turbulence on a Boundary Layer Flow.....	55
6.1 Surface Heat Flux.....	55
6.2 Velocity Field.....	65
7. Conclusions and Recommendations	72
7.1 Specific Conclusions.....	73
7.2 Recommendations	74
Appendix A: Mean Temperature Measurements of Jets in Crossflow for Gas Turbine Film Cooling Application	A1
Appendix B: Generation of Very High Freestream Turbulence Levels and the Effects on Heat Transfer	B1
Bibliography.....	Bi-1

List of Figures

Figure	Title	Page
2.1	Velocity profiles in terms of inner variables at five different spanwise locations.	12
2.2	Spanwise uniformity for the standard boundary layer.	13
2.3	Friction coefficients for a range of momentum Reynolds numbers as compared with a correlation. The friction coefficients were deduced from a Clauser fit of the log-law.	15
2.4	Benchmark test for the constant heat flux plate with two different freestream velocities and heat flux levels.	16
3.1	Streamwise turbulence intensity decay for grids in the three facilities as compared with curve fit from Baines and Peterson (1951).	18
3.2	Streamwise and vertical integral length scales in wind tunnel, compared to slopes of curve fits from Comte-Bellot & Corrsin (1966), and data from Baines and Peterson (1951).	20
3.3	Nondimensional 1-D spectra: a) planar grid in small water channel, b) bi-planar grid in large water channel, c) bi-planar grid in wind tunnel compared with von Karman spectrum.	21
3.4	Geometry and coordinates for delta wing array.	23
3.5	Streamwise turbulence intensity decay at varying angles of attack.	24

3.6	Comparison of the streamwise turbulence intensity decay between grids based on x/c (c , chord length), and x/b (b , bar width).	26
3.7	Schematic of mean velocity profile evolution in water channel.	28
3.8	a) Mean velocity profiles, b) Turbulence intensity profiles, c) Kinetic Energy profiles at $z/D = 28$ and 87 .	28
3.9	Streamwise turbulence intensity decay comparing velocity ratios.	30
3.10	Streamwise turbulence intensity decay comparing jet hole diameters.	31
3.11a	Effect of velocity ratio on integral length scale growth, $VR = 3.7, 5.3$ and 7.8 .	33
3.11b	Effect of diameter size on integral length scale growth, $VR = 5.3$, $D = 6.35$ mm and 12.7 mm.	33
3.12	Schematic of the wind tunnel turbulence generator.	35
3.13	Spanwise uniformity of highly turbulent flowfield before and after improvements. These profiles were acquired at $x/D = 130, 134$ from holes.	38
3.14	Streamwise length scales for the highly turbulent flowfield as compared with Whan-Tong's (1991) length scales and grid turbulence growth based on x/M .	39
3.15	Turbulence level decay rate as compared with grid turbulence rate and grid turbulence levels.	39

3.16	Streamwise decay of turbulence levels as a function of jet-to-mainstream velocity ratio and jet Reynolds number.	40
4.1	Measured frequency response for several different wire diameters and freestream velocities.	44
4.2	Comparison of velocity/temperature correlations with those given in the literature.	47
5.1	Dimensionless temperature contours along the jet centerline for $I = 0.125$, $DR = 2.0$, $VR = 0.25$, $M = 0.5$.	52
5.2	Dimensionless temperature contours along the jet centerline for $I = 0.5$, $DR = 2.0$, $VR = 0.50$, $M = 1.0$.	52
5.3	Dimensionless temperature contours along the jet centerline for $I = 2.0$, $DR = 2.0$, $VR = 1.0$, $M = 2.0$.	53
5.4	Dimensionless temperature contours along the jet centerline for $I = 0.5$, $DR = 1.2$, $VR = 0.65$, $M = 0.775$.	53
6.1	Stanton number distribution for both the standard boundary layer and high freestream turbulence case.	56
6.2	Ratio of high freestream turbulence St to the standard boundary layer St_0 at the same streamwise locations.	58
6.3	Comparison of present data with the Hancock/Bradshaw (1983) correlation.	60
6.4	Comparison of present data with the Maciejewski and Moffat (1989) correlation.	62
6.5	Comparison of present data to the Ames and Moffat (1990b) correlation using the turbulent dissipation scale.	63

6.6	Comparison of present data to the Ames and Moffat (1990b) correlation using the turbulent integral scale.	64
6.7	Mean velocity profiles in terms of inner wall variables at three different turbulence levels.	66
6.8a	Profile of rms fluctuating streamwise velocities non-dimensionalized with inner wall coordinates.	67
6.8b	Profile of rms fluctuating vertical velocities non-dimensionalized with inner wall coordinates.	67
6.9	Correlation coefficient for a boundary layer influenced by high freestream turbulence.	70
6.10	Comparison of nondimensionalized Reynolds shear stress with a standard boundary layer and boundary layer influenced by high freestream turbulence.	71

List of Tables

Table No.	Title	Page
5.1	Range of Experimental Parameters	50



Accession For	
NTIS	<input checked="" type="checkbox"/>
CRA&I	<input checked="" type="checkbox"/>
DTIC	<input type="checkbox"/>
TAB	<input type="checkbox"/>
Unannounced	<input type="checkbox"/>
Justification _____	
By _____	
Distribution / _____	
Availability Codes	
Dist	Avail and/or Special
A-1	

Nomenclature

b	Grid bar width
c	Delta wing chord
C_f	Friction coefficient
C_{f0}	Friction coefficient for a standard boundary layer
C_p	Specific heat
D	Jet hole diameter
DR	Density ratio, ρ_j/ρ_∞
E_{11}	One-dimensional wave number spectra
h	Heat transfer coefficient
H	Shape factor; water channel top plate height
HB	Hancock/Bradshaw parameter
I	Momentum flux ratio, $(\rho_j U_j^2)/(\rho_\infty U_\infty^2)$
k	Thermal conductivity
L_u^ε	Dissipation length scale
M	Grid mesh size; mass flux ratio, $(\rho_j U_j)/(\rho_\infty U_\infty)$
n	Exponent of decay/growth
q''	Wall heat flux
R_{ut}	Streamwise velocity/temperature correlation coefficient
R_{vt}	Vertical velocity/temperature correlation coefficient
R_{uv}	Velocity correlation coefficient
Re_c	Chord length Reynolds number
Re_D	Hole diameter Reynolds number
Re_M	Grid mesh Reynolds number
Re_Δ	Enthalpy thickness Reynolds number
Re_θ	Momentum thickness Reynolds number
Re_x	Reynolds number based on a virtual origin
S	Hole spacing, pitch
St	Stanton number
St_0	Stanton number for a standard boundary layer
St'	Stanton number based on u'_{max}
t	Temperature
TLR	Turbulence scaling parameter

Tu	Turbulence intensity, u'/U_∞
u	Velocity in streamwise direction
u^+	Nondimensional velocity, u/u_τ
u_τ	Friction velocity
u'	RMS velocity in streamwise direction
U, U_∞	Mainstream velocity in streamwise direction
U_j	Jet velocity
v'	RMS velocity in normal direction
VR	Velocity ratio, $(\rho_j U_j)/(\rho_\infty U_\infty)$
x	Streamwise distance
x_h	Streamwise distance measured from the start of the heater plate
W	Total width of test section
y	Vertical distance
y^+	Nondimensional vertical distance, $y \cdot u_\tau / \nu$
z	spanwise distance

Greek

α	Delta wing angle; thermal diffusivity
β	Low Re_θ function
Δ	Enthalpy thickness
δ_{99}	Velocity boundary layer thickness
δ^*	Displacement thickness
δ_{th}	Thermal boundary layer thickness
κ	Wave number
Λ_x	Streamwise integral turbulent length scale
Λ_y	Vertical integral turbulent length scale
ρ_j	Jet density
ρ_∞	Freestream density
θ	Momentum thickness; temperature ratio

Acknowledgements

This report is submitted by the Turbulence and Turbine Cooling Research Laboratory (TTCRL) at the University of Texas at Austin, to Air Force Systems Command, Wright Laboratory/POTC, under U.S. Air Force Contract F33515-88-C-2830. The program described in this report was sponsored and monitored by Wright Laboratory/POTC. Dr. Charles MacArthur developed the PRDA associated with this research, and he was the original Air Force Project Engineer.

The authors would like to acknowledge several people who have provided technical and fabrication support throughout this research program. Several of these people also work in the TTCRL, but are not specifically associated with this research program. Ms. Janine Whan-Tong did the initial development work on the turbulence generator designs. Mr. Choon L. Gan developed the simultaneous temperature/velocity data acquisition program. Mr. David Dotson helped in constructing the turbulence generator and Mr. Tim Diller helped in plotting the temperature contours.

Personnel not working in the TTCRL, but who did provide consultation services include: Mr. Hank Franklin, for machining and for his help in acquiring a fan for the initial turbulence generator tests; and Mr. John Spurgeon, for electrical and motor controller problems.

We would like to thank Engineering Laboratory Design, Inc. in Minnesota for their design and construction of the boundary layer wind tunnel. In particular, thanks to Mr. Art Anderson who helped install the tunnel in our laboratory.

We would also like to thank Wright Laboratory and Mr. Matt Meininger, the current Project Engineer, for their support of this project and Allied-Signal Aerospace Company, Garrett Engine Division, for their support in related turbine cooling experiments that have taken place in our lab.

1. Introduction

This document represents the Final Technical Report for the Turbine Heat Transfer Research Program entitled "Hydrodynamic Effects on Heat Transfer for Film-Cooled Turbine Blades." This program was conducted at the Turbulence and Turbine Cooling Research Laboratory at the University of Texas at Austin, for Air Force Systems Command, Wright Laboratory/POTC, under U.S. Air Force Contract F33515-88-C-2830.

1.1 Air Force Turbine Heat Transfer Research Program

The following paragraphs were extracted from the Air Force Turbine Heat Transfer Research PRDA. The objective was as follows:

It is to provide fundamental understanding of heat transfer processes and control methods which apply to the turbines of military turbine engines. To meet this objective, experimental data are needed on turbine heat transfer under conditions and in physical configurations that properly simulate engine conditions. Such data are currently severely limited in amount and scope and are, therefore, insufficient for design and analysis purposes.

The overall Technical Requirements for the Air Force Turbine Heat Transfer Research program were as follows:

The contractor shall conduct experimental research on fluid dynamic phenomena which govern the heat transfer in the turbine component of advanced military turbine aircraft engines. Phenomena to be studied include, but may not be limited to, one or more of the following: influence on the boundary layer of surface curvature, influence of freestream turbulence, influence of strong pressure gradients, film cooling injection, turbine secondary flows, unsteady flows (rotor-stator interactions), nonuniform turbine entry temperature profiles, very large gas-to-wall temperature differences, and boundary layer transition and separation. Experiments shall reproduce, physically or through fluid dynamic similarity, to the maximum extent possible the aerodynamic and thermodynamic conditions of advanced military turbine engines. Measurement and data

reduction techniques shall employ, where possible, non-intrusive methods, methods giving simultaneous measurements of several separate quantities, and measurements giving very high spatial or temporal detail.

1.2 The University of Texas Turbine Cooling Research Program

The research program proposed by The University of Texas at Austin (UT) was concentrated into three areas of the Air Force program: the influence of freestream turbulence, fluid and heat transfer measurements using non-intrusive methods, and development of experimental methods for simultaneous measurement of several quantities. The research was conducted by personnel in the Turbulence and Turbine Cooling Research Laboratory (TTCRL) in the Mechanical Engineering Department at UT. The objective of the UT program was primarily to quantify the effects of very high freestream turbulence on the hydrodynamic and thermal flow fields, and on surface heat flux. The scope of the work required to meet this objective included development of a very high freestream turbulence facility, development of a simultaneous temperature and velocity measurement capability, and studies of the effects of very high freestream turbulence on standard boundary layer flow and on film cooling flows. The scope was divided into five tasks.

Task 1 was the design, development, and testing of a fast-response temperature probe for use in simultaneous velocity and temperature measurements of $u't'$ and $v't'$ correlations. These measurements are important to guide development of improved models for the turbulent transport of heat. Furthermore, spatial correlations between u' (or v') and t' indicate the scale of the structures responsible for heat transport. To meet this task, we developed a method using a submicron cold-wire and a laser Doppler velocimeter (LDV) which measures at essentially the same spatial and temporal point in the flow. The LDV measures the velocity components of the flow upstream of the temperature sensor to avoid flow interference from the temperature probe. A small diameter cold-wire is used so that the sensor frequency response is sufficient to measure the temperature fluctuations. TTCRL personnel developed data acquisition software for the simultaneous

velocity/temperature measurements. Validating the simultaneous measurement technique included comparing velocity/temperature correlations to those found in the literature.

Task 2 was the design, development, and testing of a very high freestream turbulence generator to provide turbulence at the 15-25 percent level with appropriate length scales. Preliminary development work was carried out in a water channel, using both an LDV and a hot-film sensor to measure mean and fluctuating velocities, two-point correlations, and spectra. Initial experiments were carried out using standard biplanar meshes described in the open literature, to qualify, or benchmark, the testing procedures for evaluating high turbulence levels. Following the benchmark testing, two unique turbulence generators were designed, constructed, and tested in the water channel to determine the capability of the systems to yield high turbulence with sufficient homogeneity and isotropy, and with proper length scales. The set of benchmark grids and the selected unique turbulence generator were then reconstructed for the boundary layer wind tunnel and evaluated in terms of turbulence levels, two-point correlations, spectra, along with length scale distributions, isotropy, and homogeneity. This task also involved significant testing and modification of the turbulence generator for wind tunnel application to improve the spanwise uniformity of the mean velocity.

Task 3 was the development, installation, and validation of a new wind tunnel. Also included as a part of this task was the installation of the secondary injection system required for the turbulence generator which is located just downstream of the tunnel contraction. Both the secondary injection system and the new wind tunnel were obtained at no cost to this contract. The tunnel is closed-loop and of boundary layer design with a test section that has a four-to-one aspect ratio. A three-axis traverse system for either hot-wire or cold-wire sensors is included as an integral part of the tunnel test section. The test surface is a constant heat flux surface which provides a heated boundary layer for the turbulent heat flux measurements. The validation segment of this task included benchmarking both the fluid mechanics and heat transfer for the standard boundary layer. Verification of the hydrodynamic boundary layer characteristics included evaluating the

spanwise uniformity, mean velocity profiles, and Reynolds stress profiles. Verification of the heat transfer and thermal boundary layer characteristics included evaluating the streamwise and spanwise surface heat transfer coefficients, and mean and fluctuating thermal field measurements. These data were compared to that published in the literature and checked for consistency in terms of energy balances between surface heat flux and enthalpy thickness.

Task 4 was the documentation of the effects of very high freestream turbulence field on the fluid mechanics and heat transfer of turbulent boundary layer flows. The enhancement of the surface heat transfer was quantified in terms of several correlating parameters and compared to the data found in the literature. Measurements were also made to quantify the effects of the high turbulence levels on the mean and turbulence characteristics of the velocity and thermal boundary layers.

Task 5 focused on film-cooled boundary layer flows and the effects of freestream turbulence on the flow structure and surface heat transfer. Within the time period of this research, this task was partially completed. Measurements of temperature profiles within and downstream of a row of jets-in-crossflow were carried out for a range of film cooling injection-to-mainstream mass flux ratios (blowing ratios) and for a range of density ratios, all at a quiescent turbulence level (0.2%). The quiescent tests serve as reference tests for the effects of freestream turbulence on film cooling. Companion tests to document the fluid mechanic flow fields and surface heat transfer distributions have been carried out under another program.

1.3 Organization of the Report

The sections which follow describe the tasks of the research and their results. Section 2 describes the water channel and wind tunnel facilities, instrumentation, and data acquisition techniques used in this study. Qualification of the new boundary layer wind tunnel that was specifically designed to study the effects of high turbulence on simulated film cooling jets, which includes varying the density ratio, is also presented. Section 3 presents the design and development methodology for the high turbulence

generators, along with qualifications of the final generator design. Section 4 presents the design and development of the simultaneous velocity-temperature probe, along with qualification studies of its high-frequency temperature response and its measurement capabilities. Section 5 presents the mean temperature field measurements of the simulated film-cooling jets. Section 6 presents the studies conducted to document the effects of high turbulence on the standard boundary layer, including both velocity field and surface measurements. And finally, Section 7 presents the conclusions of the research and final recommendations for future studies.

2. Facilities Description and Qualification

During the course of this study, two water channel and two wind tunnel facilities were used. One wind tunnel was a new facility which was installed specifically to incorporate the freestream turbulence generator which was developed as part of this study. Velocity field measurements were made with single and two component LDV systems, and with hot-wire and hot-film anemometry. Thermal field measurements were made using a cold-wire probe. A constant heat flux test surface, installed in the new wind tunnel, was instrumented with thin thermocouple ribbons. These facilities, measurement apparatuses, data acquisition techniques, and qualification tests on the new wind tunnel are described briefly in the following sections.

2.1 Water Channel and Wind Tunnel Facilities

Two water channel facilities were used to evaluate different concepts for generating very high freestream turbulence levels. The TTCRL boundary layer water channel is a recirculating open channel with a test section 5 m long by 0.5 m wide by 0.3 m deep. A complete description of this facility can be found in Coughran (1986). For normal operating conditions freestream turbulence levels were measured to be $Tu = 0.5\%$. One modification to this facility was made to evaluate turbulence levels generated by jets-in-crossflow. A plenum chamber and a removable bottom insert with a row of jet holes were installed on the floor of the water channel. The flow to the plenum was pumped from the upstream stilling tank by a 1/4-hp pump controlled with a variac. The volumetric flowrate through this loop was measured through a rotameter connected in series, between the pump and the plenum chamber. The rotameter was accurate to ± 0.1 percent of the typical flowrate.

The second water channel facility, which incorporates a smaller channel, was used to test a delta-wing grid concept for generating high turbulence levels. This facility, constructed by Engineering Laboratory Design, Inc., is a closed-circuit, open channel with a plexiglas test section measuring 43.2 cm in length, 15.2 cm in width by 15.2 cm in depth. The area contraction ratio upstream of the test section is 4:1. Flow speed is controlled by a Fincor A/C

motor controller which adjusted the 1/2-hp pump. For normal operating conditions freestream turbulence levels were measured to be $Tu = 0.6\%$.

Thermal field measurements of film cooling flows were made in the TTCRL film cooling simulation wind tunnel. A detailed description of this tunnel is given in Pietrzyk et al. (1989). The tunnel, constructed by Engineering Laboratory Design, Inc., is a closed-loop facility with a $0.6 \times 0.6 \times 2.4$ -m-long test section. Suction is used to remove the boundary layer upstream of the test section, and a new boundary layer is initiated at the sharp leading edge of the test plate that formed the test section floor. The suction rate is set based on measurements of the pressure differential across the leading edge of the plate. LDV measurements show that this ensures parallel flow above the leading edge. A heat exchanger, located between the blower and the wind tunnel contraction, maintains the freestream temperature to $\pm 0.5^\circ\text{C}$. For all of the thermal field experiments, the freestream velocity and temperature were $20 \text{ m/s} \pm 1\%$ and $25^\circ\text{C} \pm 0.5^\circ\text{C}$ while the freestream turbulence intensity was $Tu = 0.2\%$. The freestream velocity was uniform within $\pm 0.5\%$ in both the spanwise and streamwise directions.

The TTCRL boundary layer wind tunnel was designed, constructed, and installed specifically to incorporate the freestream turbulence generator developed as part of this project. Engineering Design Laboratory, Inc. designed, based on our specifications, and constructed this wind tunnel. The turbulence generator, which was later installed in the wind tunnel, was designed, constructed, and installed by TTCRL personnel. The tunnel is a closed-loop facility with a working test section 180 cm long, 61 cm wide and 15.2 cm high. One side wall and the ceiling of the test section are made of 1.27-cm-thick acrylic. The side wall through which LDV measurements are taken is made of 0.42-cm-thick glass. Moveable ceiling panels in the test section, each panel 61cm in length with a separate vertical traverse, allow adjustment of the ceiling contour and hence, the pressure gradient in the test section. All tests in this wind tunnel are carried out for the zero pressure gradient case. A two-dimensional, 9:1 area contraction precedes the test section and a suction slot removes the boundary layer upstream of a sharp leading edge on the test plate. The freestream turbulence intensity level measured without the turbulence generator was $Tu = 0.6\%$ at 10 m/s. The temperature in the wind

tunnel is held constant to $\pm 0.1^{\circ}\text{C}$ through the use of water cooled heat-exchanger coils upstream of the contraction.

A constant heat flux surface was installed in the boundary layer wind tunnel following an unheated leading edge plate 12 cm in length. The constant heat flux plate consists of a serpentine, monel heating element sandwiched between two kapton films. The total thickness of this sandwich is 0.20 mm. The length of the plate is 1.4 m and the total width of the plate is the same as the test section, 0.6 m. The heater plate is bonded to a 12.7-mm-thick fiberglass composite (G-10). Below the plate are several layers of insulation to minimize conductive back-side losses. Since the heating element is of a serpentine pattern, there are small gaps where only kapton is present. A numerical analysis of the conduction within the plate and the convection heat loss at the plate surface showed that this has no overall effect on the heated boundary layer, and that accurate surface temperatures could be obtained at the center of the monel strips.

Typically, the heat flux plate is operated at a heat flux of 260 W/m^2 which results in a temperature differential of nominally 10°C at 8 m/s. Low temperature differentials are used to avoid property variation effects, but this plate does have the capability of operating at a maximum heat flux of 3100 W/m^2 . A DC power supply is used as the supply to the resistive heater. The voltage difference across a shunt resistor is measured as well as the total voltage difference across the DC power supply to give the total heat flux. A significant radiation correction is required to obtain the net convective heat flux. The radiation correction is based on the radiative exchange between the heat flux plate and the wind tunnel roof. Surface temperatures of the wind tunnel roof are measured to get an accurate measure of the surrounding radiative fluxes. The radiative heat flux is between 15 - 20% of the total heat flux.

2.2 Measurement Apparatus and Data Acquisition Techniques

Two LDV systems were used in this study. One system, designed and constructed by TTCRL personnel, is a fiber optic based LDV system using a 600-mW-argon ion laser, frequency shifting, 60 mm fl transmitting/collection

lens, and backscatter optics. The probe volume for this LDV is 60 μm in diameter and 500 μm in length. The second LDV system is a commercial system, TSI model 9100-10, which is operated in either single or two component mode. This system uses a 2-W-argon ion laser, frequency shifting, 480 mm fl transmitting/collection lens, and backscatter optics. The probe volume for this LDV is 80 μm in diameter and 300 μm in length.

Both LDV systems use TSI model 1990 counter processors. For water flows the data rates are high enough ($> 400/\text{s}$) such that a continuous velocity signal can be obtained by passing the output of the LDV counter through a digital-to-analog converter. For wind tunnel measurements, the LDV counter output is input directly into a Macintosh II computer. These data are corrected for velocity bias errors using residence time weighting.

Silicon carbide particles, 1.5 μm in diameter, are used as seed particles in the water channel. These particles were found to have no effect on hot-film measurements which are sometimes made simultaneously with the LDV measurements. A special seed generator had to be constructed so that LDV and hot-wire or cold-wire measurements could be made in the wind tunnel. Titanium dioxide particles normally used as the seeding material had the tendency to coat the hot-wire, causing an unacceptable voltage drift. Smoke particles from stick incense proved to be a good replacement. A smoke-generation box was constructed separate from the wind tunnel loop. The incense is burned in this pressurized smoke box, and the box is connected to the wind tunnel via an air-cooled heat-exchanger coil. The tar from the hot smoke condenses on plugs of fine steel wool placed at the exit of the smoke box, and on the inside walls of the heat-exchanger coil. To ensure that no tar deposits on the hot-wire, or condenses on the glass wall, the steel wool is changed frequently.

Two-point spatial correlations require simultaneous measurements with both an LDV system and a hot-wire or hot-film probe. Continuous velocity records required for autocorrelations and/or spectral analysis were also measured with hot-wire or hot-film probes. A TSI model 1050 constant temperature anemometer was used for these measurements. For water flows a TSI model 1212-20W cylindrical hot-film probe with a 50- μm diameter and

1-mm-long sensor was used. Measurements in air were typically made with a TSI model 1218 boundary layer probe with a 5- μ m diameter platinum-coated tungsten wire.

Data from the LDV systems and hot-wire anemometers were acquired using Macintosh II computers and National Instruments interface boards. A National Instruments NB-DIO-32 digital input board was used to acquire data directly from the LDV counters. Data acquisition and processing software were written by TTCRL personnel using ThinkC 4.0 for the Macintosh. Analog outputs from the LDV systems (after passing through a digital-to-analog converter) and the hot-wire anemometer were acquired using a National Instruments NB-MIO-16X analog-to-digital board. The analog-to-digital board was driven by programs developed by TTCRL personnel, using National Instruments LabView 2 symbolic programming language on a Macintosh II. The voltage-to-velocity conversions, statistical analyses, and on-line graphing of the data were also performed using LabView routines written specifically for this project.

Different data acquisition techniques were used for the simultaneous LDV and hot-wire/film measurements made in water and in air. Measurements in water were made with an analog output from the LDV system which was sampled essentially simultaneously (1-ms delay) with the analog output from the hot-film probe. Continuous analog LDV output was not possible for the wind tunnel measurements because of the much shorter time scales in this flow. Simultaneous measurements in this case required that acquisition of an analog hot-wire signal be triggered by the LDV counter when a valid LDV measurement was made. A special program was written which allowed data to be sampled from the analog input of the hot-wire anemometer within 30 μ s of the measurement acquired from the LDV system. This was shown to be well within the smallest time scale of the wind tunnel flows.

The constant heat flux plate was instrumented with type E surface thermocouple ribbons which are 0.038 mm thick. These thin thermocouple ribbons minimize conduction errors and any flow disturbances. The thermocouple junction is 0.076 mm thick which nondimensionally is $y^+ < 2$. These ribbons are connected to 0.051-mm-diameter wires which run laterally

along the surface of the plate and are then connected to larger diameter wires at the edge of the plate. The larger wires are then wired into a multiplexing board which is controlled by a National Instruments NB-MIO-16X analog-to-digital board that is housed inside a Macintosh II computer. Two multiplexing boards acquire outputs from 63 thermocouples. On-line data acquisition and data analysis software were written specifically for the constant heat flux tests using the National Instruments Labview 2 software.

2.3 Qualification Tests of the Boundary Layer Wind Tunnel

Both fluid mechanic and heat transfer qualification tests for the boundary layer tunnel were done to ensure reasonable spanwise uniformity and standard velocity and thermal boundary layers for the constant heat flux plate tests. Evaluating the velocity boundary layer was done by comparing the mean and fluctuating velocity profiles as well as the turbulent shear stress correlation profiles to those found in the literature. The spanwise uniformity for the velocity boundary layer was evaluated in terms of such parameters such as momentum thickness, θ ; the displacement thickness, δ^* ; the friction coefficient, C_f ; and the shape factor, H . Evaluating the heat transfer was done by comparing the surface temperature measurements in terms of the Stanton number, St , with correlations given in the literature. An energy balance check was also done through the enthalpy thickness. The spanwise uniformity was evaluated through surface temperature measurements.

Figure 2.1 shows velocity profiles, in terms of inner variables, which were taken at five different spanwise locations and a streamwise distance of 37 cm downstream of the leading edge plate. To ensure that the boundary layer was turbulent, the boundary layer was tripped using a 2-mm-diameter wire located 4 cm upstream of the constant heat flux plate. For these profiles the momentum Reynolds number was $Re_\theta = 1143$.

Figure 2.2 shows the spanwise variation, normalized by the spanwise average, of the skin friction coefficient, C_f , the displacement thickness, δ^* , the momentum thickness, θ , and the shape factor, H . The skin friction

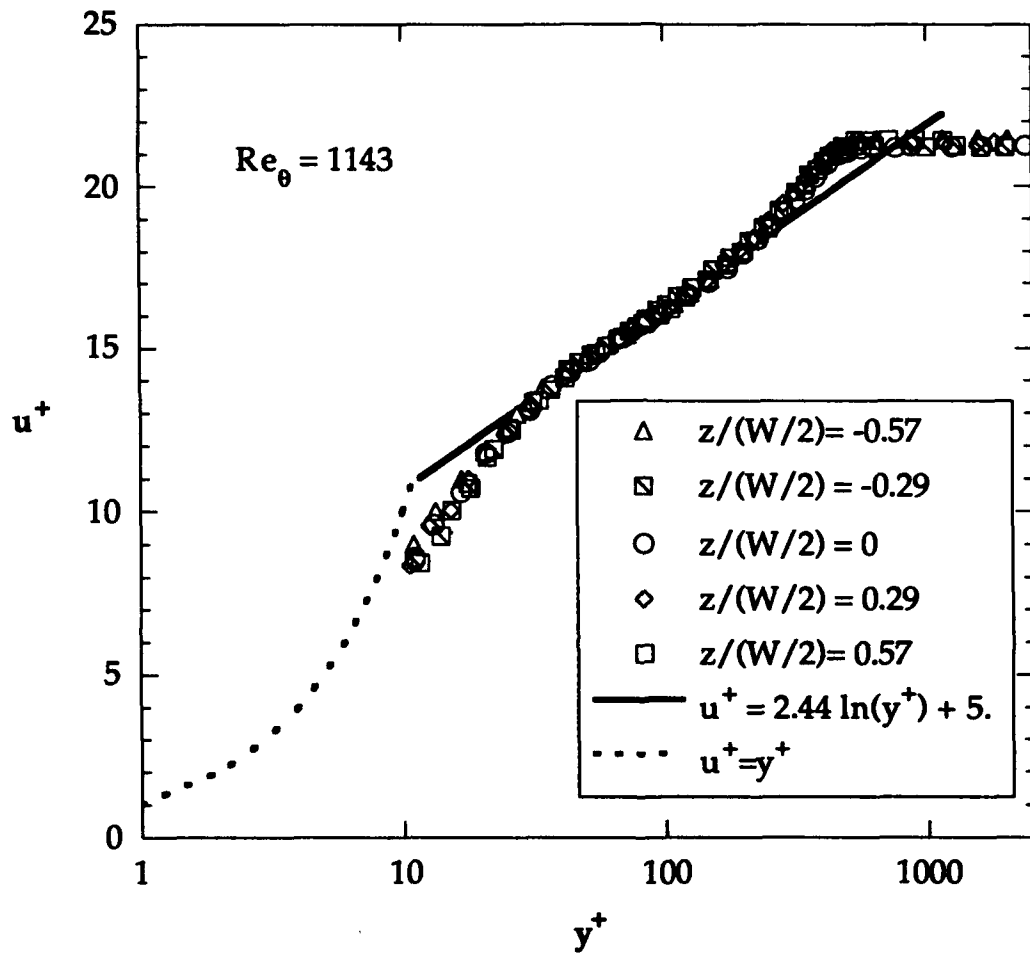


Figure 2.1 Velocity profiles in terms of inner variables at five different spanwise locations.

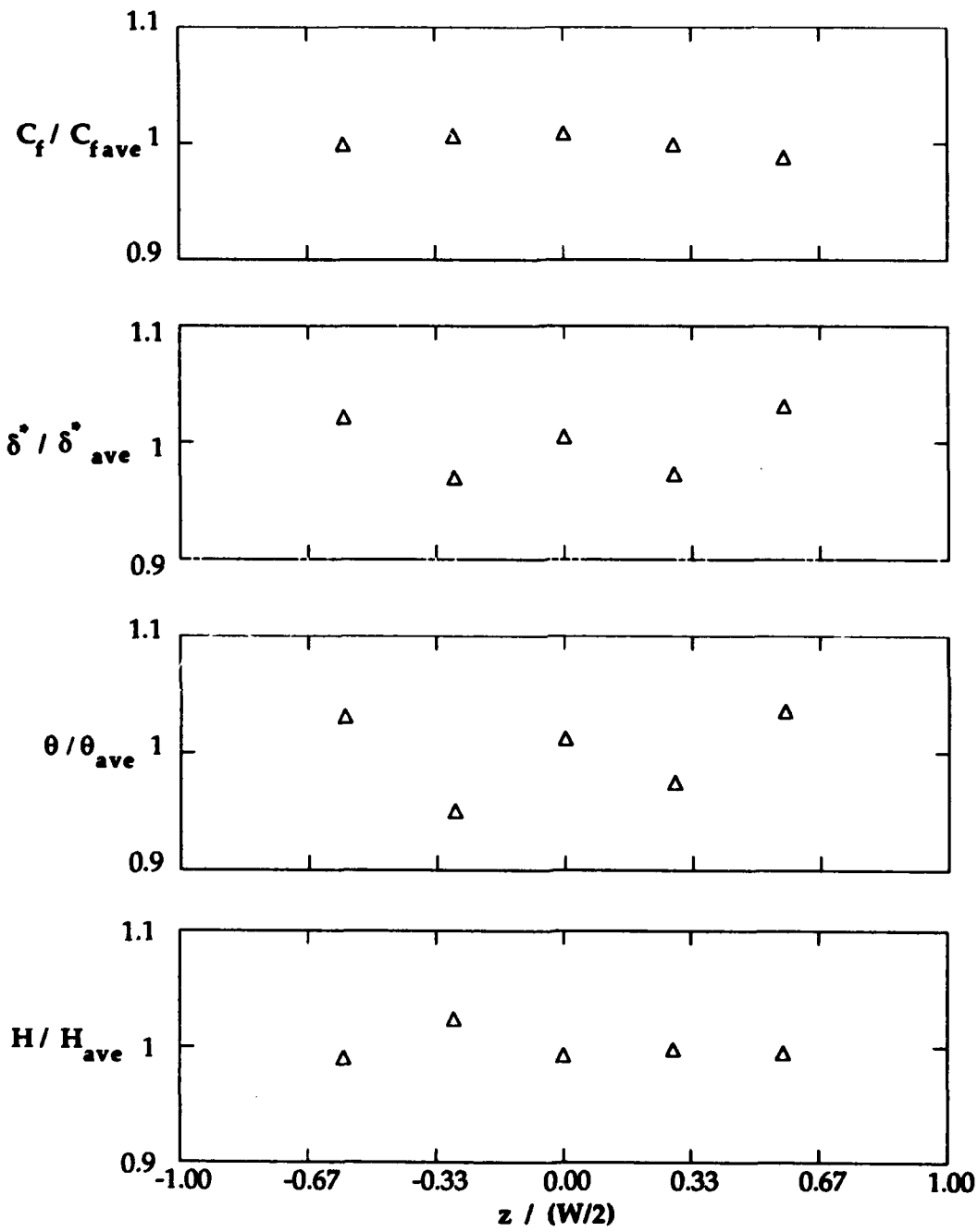


Figure 2.2 Spanwise uniformity for the standard boundary layer.

coefficients were calculated using a Clauser fit to the log-law. The spanwise variation in terms of these boundary layer parameters is better than $\pm 5\%$. Skin friction coefficients, C_f , were obtained from experiments conducted at several different momentum Reynolds numbers and compared to a correlation given by Kays and Crawford (1980). These results, shown in Figure 2.3, were in good agreement with the correlation.

Benchmark tests for the constant heat flux plate were done to compare the experimental results with the Stanton number correlation given in Kays and Crawford (1980). The measured Stanton numbers were based on the convective surface heat flux, the temperature differential between the freestream and the surface, the freestream velocity and the air properties which were evaluated at an average film temperature. Benchmark tests were done at two different velocities and two different heat flux conditions. These results are shown in Figure 2.4. Downstream of the region where there are unheated starting length effects, agreement between the correlation and the data is within 5%, except the last data point when $U = 14.3$ m/s. The difference between the correlation and measured Stanton number at this last streamwise position is 6%. The spanwise uniformity of the surface temperature is $\pm 5\%$ at 50 cm downstream from the start of the heat flux plate.

An energy balance in the boundary layer can be evaluated in terms of calculating the enthalpy thickness by two different methods. The enthalpy thickness can be calculated directly by integrating the velocity and temperature profiles, or by multiplying the Stanton number by the streamwise distance along the heat flux plate, $St \cdot \Delta x$. Checks were made for the standard boundary layer case at $x = 25$ cm and $x = 50$ cm downstream of the start of the heat flux plate. Enthalpy thicknesses obtained from the integrated profiles and from the $St \cdot \Delta x$ product were within 1.4% and 5.9% at the two streamwise positions.

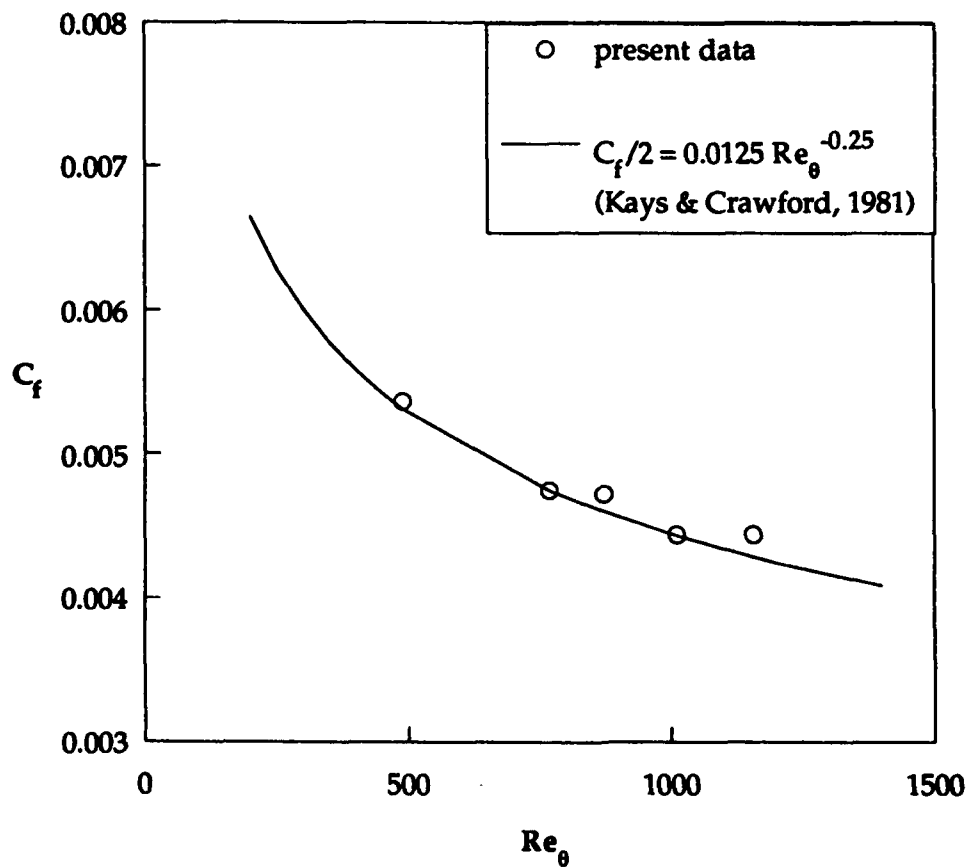


Figure 2.3 Friction coefficients for a range of momentum Reynolds numbers as compared with a correlation. The friction coefficients were deduced from a Clauser fit of the log-law.

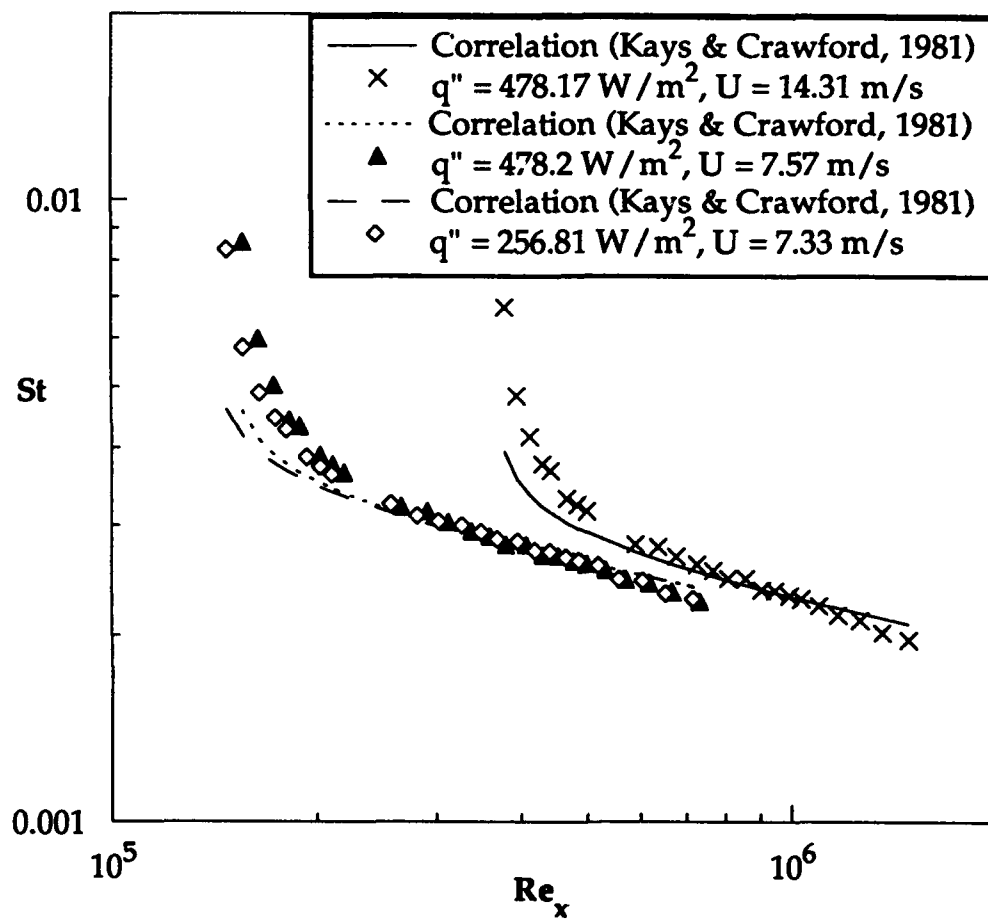


Figure 2.4 Benchmark test for the constant heat flux plate with two different freestream velocities and heat flux levels.

3. Development of a Very High Turbulence Generator

Two devices for developing very high freestream turbulence, the delta wing array and the normal jet configuration, were evaluated in this project. Measurements were also made in a typical grid-generated turbulence field to validate various measurement techniques developed as part of this project. Results are presented first for the grid-generated turbulence in which the turbulence levels, turbulence decay rates, and turbulence length scales are compared to results in the literature. The delta wing array, which did not prove to be very successful, is discussed briefly. Finally, the normal jet configuration which was successful in producing very high freestream turbulence levels is described.

3.1 Grid Turbulence

Grids used in this study were selected to match the configuration used by Baines and Peterson (1951). The work of Baines and Peterson was selected as our standard of comparison because they used grids of relatively high solidity ratio which resulted in high levels of turbulence in the near vicinity of the grids, and measurements of turbulence intensity and length scale were well documented.

Bi-planar square mesh grids using square bars were used in the water channel and wind tunnel facilities. In the large water channel facility, grids were used with three different mesh sizes, $M = 102$ mm, 68 mm, and 51 mm. Each grid had a bar width of $b = 25$ mm resulting in a range of solidity ratios from $\sigma = 0.44$ to 0.75. The grid used in the wind tunnel had a mesh of $M = 25.4$ mm, a bar width of $b = 6.35$ mm, and a solidity ratio of $\sigma = 0.44$.

Mean and rms velocities were measured in both facilities using LDV systems. The freestream velocity in the water channel facility was $U_\infty = 21$ cm/s so that the mesh Reynolds number ranged from $Re_M = 0.67 \times 10^4$ to 1.3×10^4 . In the wind tunnel, a freestream velocity of $U_\infty = 10.8$ m/s was used resulting in a mesh Reynolds number of $Re_M = 1.7 \times 10^4$. Measurements of the decay of the streamwise turbulence intensity are presented in Figure 3.1 where x is the distance from the grid position. These results are compared

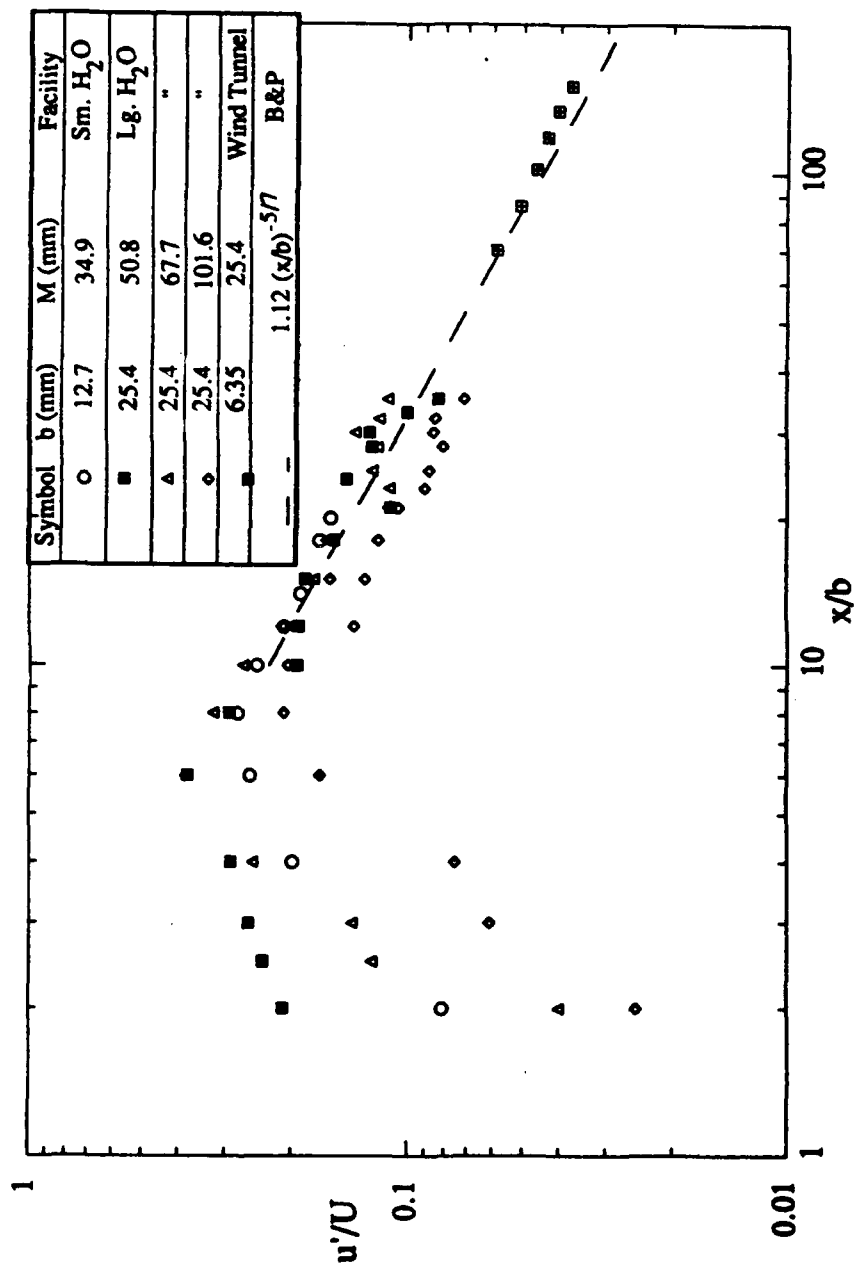


Figure 3.1 Streamwise turbulence intensity decay for grids in the three facilities as compared with curve fit from Baines and Peterson (1951).

with the decay rate found by Baines and Peterson (1951) using grids of similar geometry and in the same Reynolds number range. As shown in Figure 3.1, the present results compare well with the results of Baines and Peterson in both the magnitude and the decay rate of the turbulence intensity.

The degree of anisotropy was determined from the ratio of the streamwise to the normal rms velocities. In the wind tunnel, over the range from $x/M = 20$ to 40 , this ratio was measured to be nominally $u'/v' \approx 1.2$ which is consistent with previous grid turbulence studies.

Integral length scales of the turbulence were determined from measurements of the streamwise velocity autocorrelation for the streamwise length scale, Λ_x , and cross-stream, vertical spatial correlations of the streamwise velocity for the cross-stream length scale, Λ_y . A hot-wire (wind tunnel) or hot-film (water channel) was used for measurements of the autocorrelation, and simultaneous LDV and hot-wire/film were made for measurements of the spatial correlation. Autocorrelations were used to determine the streamwise length scale after measurements confirmed the accuracy of using the Taylor hypothesis to deduce the streamwise spatial correlation from the autocorrelation.

Our measurements, shown in Figure 3.2, were in excellent agreement with those of Baines and Peterson (1951), who measured Λ_y only, and had a growth rate that compared well to that of Comte-Bellot and Corrsin (1966). Moreover, the ratio of streamwise to cross-stream length scales was approximately $\Lambda_x/\Lambda_y = 2$ which is consistent with homogeneous, isotropic turbulence theory.

Turbulent kinetic energy spectra obtained from hot-wire/film measurements in the wind tunnel and the large water channel facilities are shown in Figure 3.3. In each case the measured spectra compared well with the theoretical spectrum (von Kármán spectrum) for homogeneous isotropic turbulence.

In summary, measurements of the turbulence intensity, decay rate, anisotropy, streamwise and cross-stream integral length scales, and energy

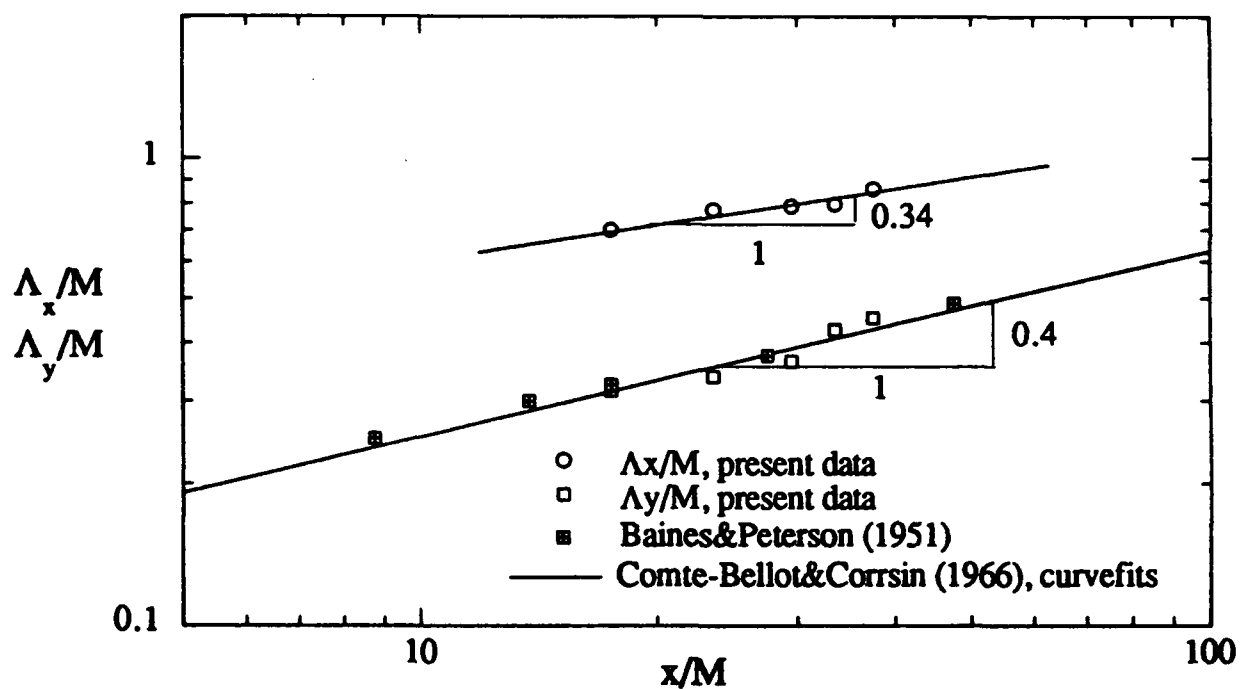


Figure 3.2 Streamwise and vertical integral length scales in wind tunnel, compared to slopes of curve fits from Comte-Bellot & Corrsin (1966), and data from Baines and Peterson (1951).

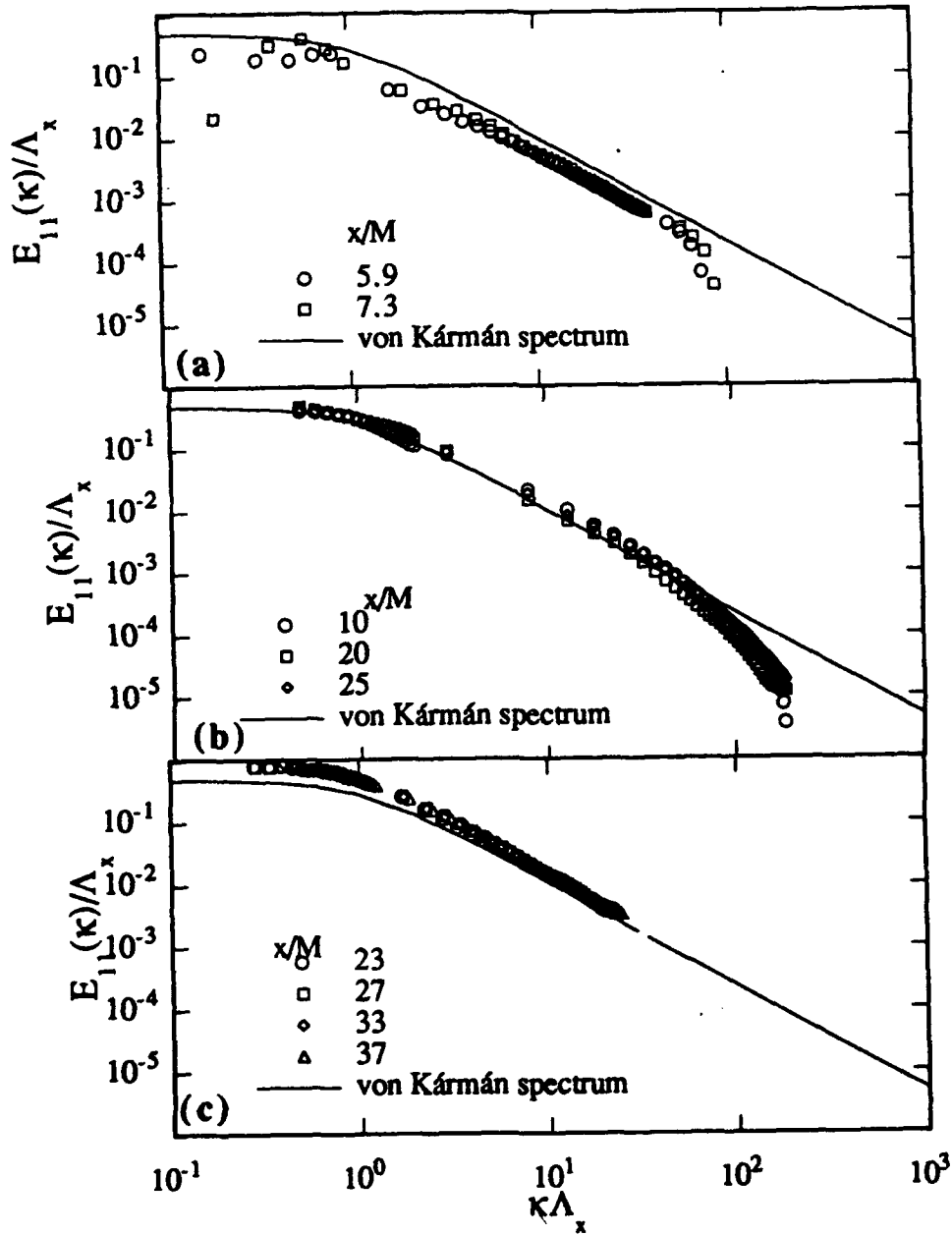


Figure 3.3 Nondimensional 1-D spectra: a) planar grid in small water channel, b) bi-planar grid in large water channel, c) bi-planar grid in wind tunnel compared with von Karman spectrum.

spectra of the grid generated turbulence were all in good agreement with the literature. This confirmed the accuracy of our measurement techniques for quantifying the characteristics of a turbulent field.

3.2 Delta Wing Array

The results of the grid tests described above also confirmed that grids would not be adequate for producing turbulence levels in excess of 20% as required for this project. Although high solidity ratio grids produce high turbulence levels for a short distance immediately behind the grid, the grid would have to be prohibitively large if the turbulence is to be sustained over a reasonable distance. For example, to maintain a turbulence level of nominally 20% over a 0.5-m distance, a bar width of 50 mm would be required. Since the test section height is 150 mm, this is clearly not feasible.

As shown by Hinze (1975) the rapid decay rate of homogeneous, isotropic turbulence is analytically predictable. Therefore, to develop a device capable maintaining high levels of turbulence over some distance requires that we forego the ideal of isotropic turbulence. The rationale of using an array of delta wings for generating freestream turbulence was based on the concept of having oriented vortices in the turbulence which would presumably decay at a slower rate than the randomly oriented vortices found in isotropic turbulence.

Experiments to determine the effectiveness of the delta wing array in generating sustained high turbulence levels were conducted using a small scale model in the small water channel. The geometry of the delta wing array is described by the schematic shown in Figure 3.4. The delta wing elements attached to the vertical strips were oriented at various angles downstream ranging from 35° to 90° from the streamwise direction. At the maximum angle (maximum blockage) the solidity ratio was $\sigma = 0.67$.

The turbulence levels developed by the delta wing array were found to be strongly dependent on the angle of the elemental blades as shown in Figure 3.5. These tests were conducted at a nominal freestream velocity of $U_\infty = 15$ cm/s with a Reynolds number of $Re_c = 2 \times 10^3$, where c is the chord length.

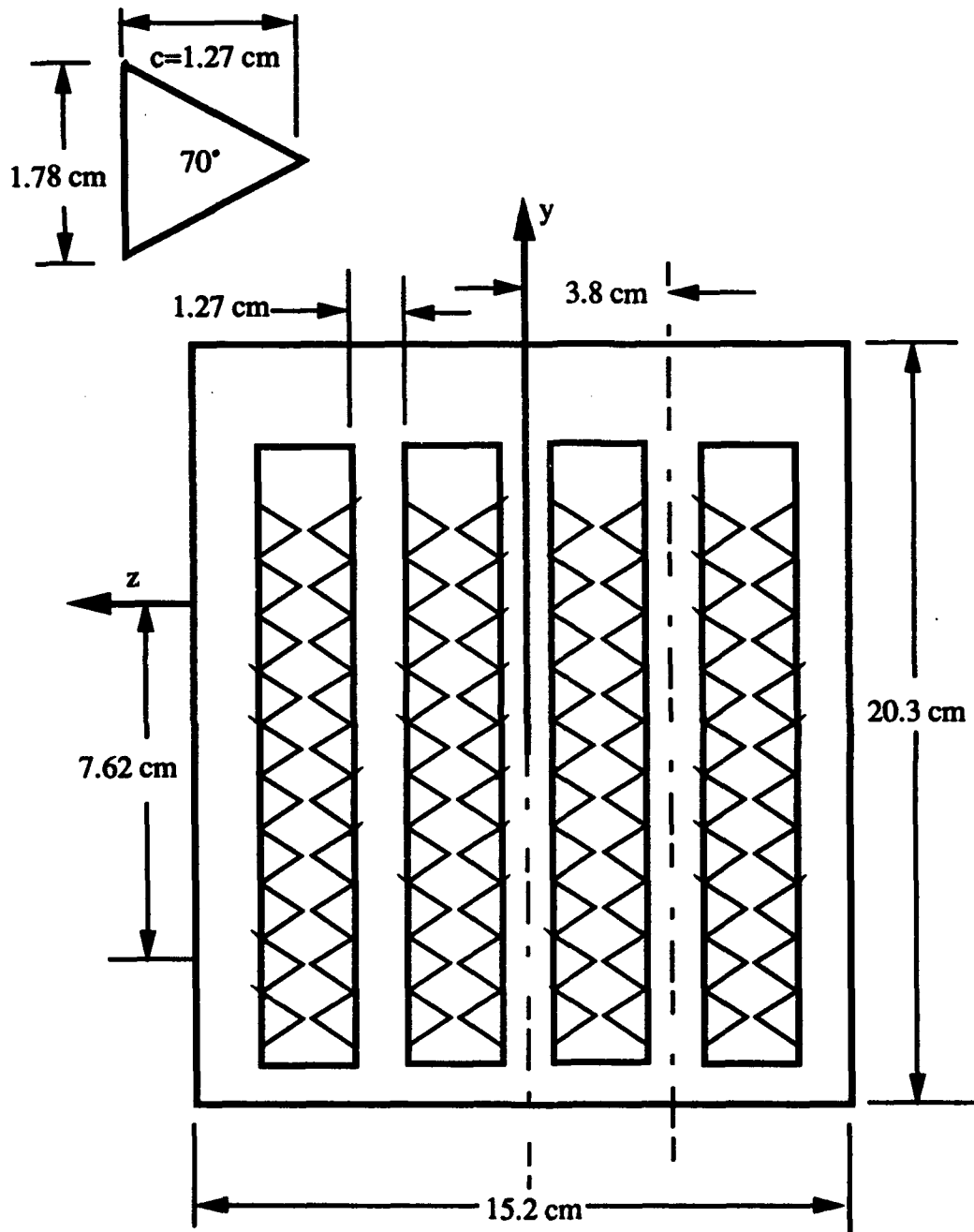


Figure 3.4 Geometry and coordinates for delta wing array.

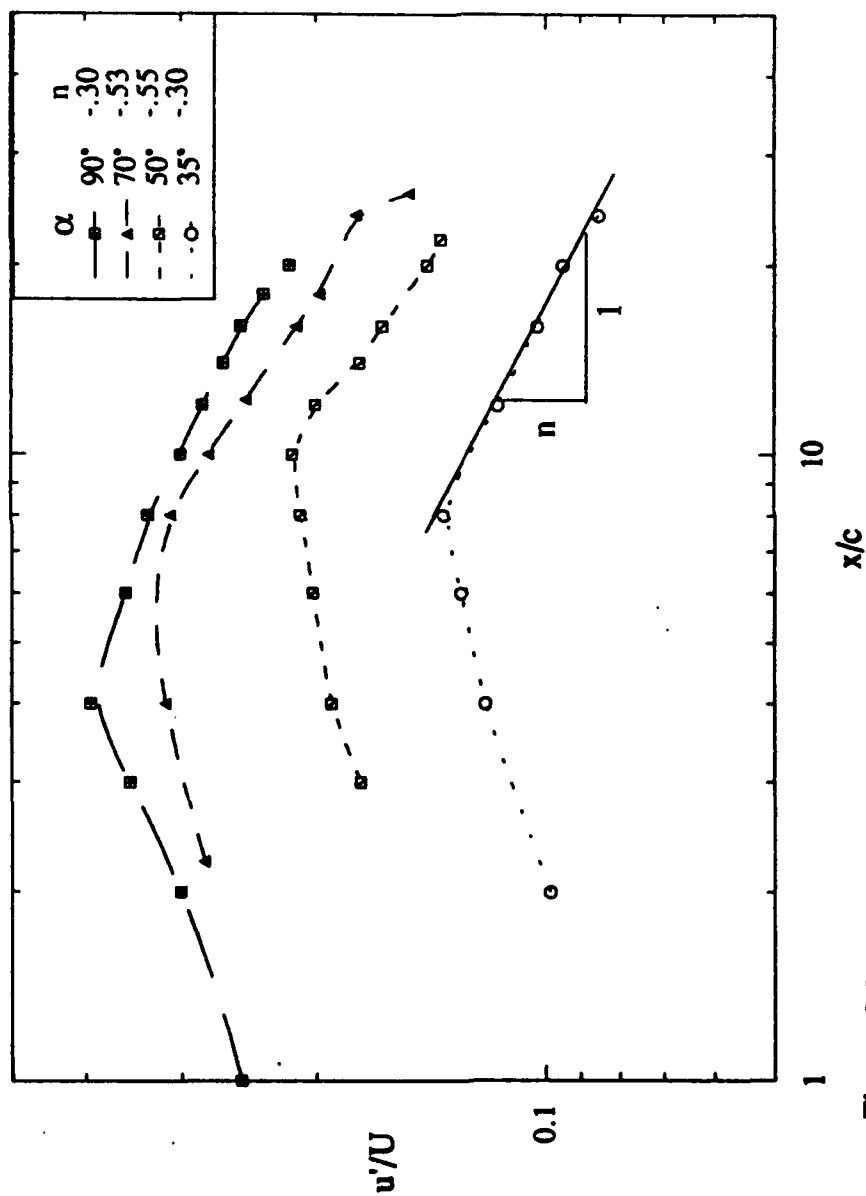


Figure 3.5 Streamwise turbulence intensity decay at varying angles of attack.

Maximum turbulence levels were found to occur at the maximum blade angle of 90° , i.e., blades in the plane of the holder. Decay rates could not be determined precisely because of the limited length of the small channel. However, over the short distance measured, the decay rate for the $\alpha = 90^\circ$ configuration was proportional to $(x/c)^{-0.3}$ which is significantly less than grid turbulence which is typically proportional to $(x/c)^{-0.7}$.

A direct comparison to grid turbulence was accomplished by testing a square mesh grid in the small water channel. The bar width was selected to be 12.7 mm which was the same as the vertical support bars used on the delta wing array. The mesh size was selected to be 34 mm which resulted in a solidity ratio of $\sigma = 0.61$ which was just slightly less than the delta wing array set at the maximum angle. Turbulence levels generated by the square mesh grid are compared to the turbulence levels generated by the delta wing array with $\alpha = 90^\circ$ in Figure 3.6. The delta wing array was found to generate significantly higher turbulence intensities with levels of 30% decaying to 22% over the range $x/c = 10$ to 20. Turbulence levels generated by the square mesh over the same streamwise distance were 25% decaying to 16%.

3.3 High Velocity Jets in Cross-stream Configuration

The objective of this study, to generate and study very high freestream turbulence levels, was based on the very high freestream turbulence levels that occur in the turbine section of a gas turbine engine. This turbulence is generated in the upstream combustor. Hence a turbulence generator design based on mechanisms similar to those which occur in a combustor would hold some promise. This was the rationale for the turbulence generator design based on high velocity jets in a cross-stream.

The high velocity jets in cross-stream configuration were developed in two phases. For the first phase various geometrical and flow parameters were investigated in a water channel facility. This section of the report discusses the data from the water channel tests that were used to design the final configuration installed in the boundary layer wind tunnel. The second phase of the development, which is discussed in Section 3.4, involved the actual

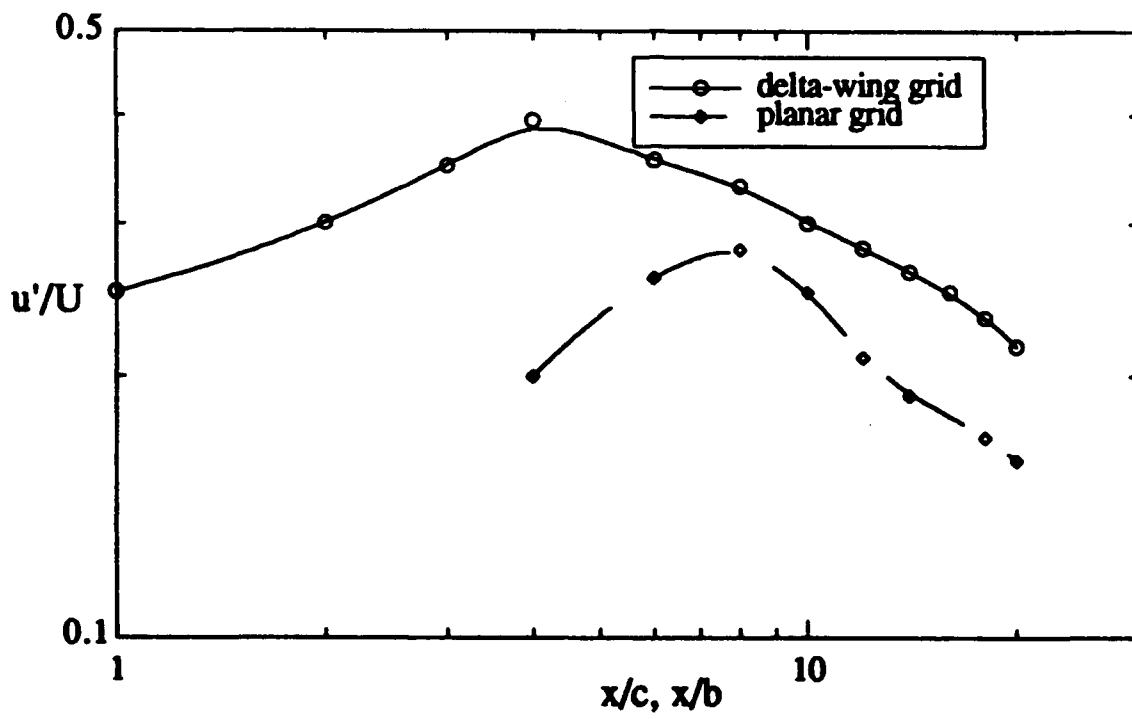


Figure 3.6 Comparison of the streamwise turbulence intensity decay between grids based on x/c (c , chord length), and x/b (b , bar width).

design for the wind tunnel application, the refinement in the design, and finally the resulting highly turbulent flowfield.

The general configuration of the row of normal jets tested in the water channel is shown in Figure 3.7. The jets were injected into the water channel through a row of holes on the bottom wall. Two hole diameters were tested, a row of 14 holes 6.35 mm in diameter, and a row of 8 holes 12.7 mm in diameter. Holes were spaced at $S/D = 1.5$ where S is the distance between hole centers. Since the row of holes did not span the water channel, side walls were installed to bracket holes on both sides. A top cover plate which could be adjusted to different heights H above the bottom wall was also installed. The final configuration used is shown in Figure 3.7.

Parameters that were studied in the water channel tests were the effect of hole diameter, the effect of hole spacing, the effect of the top wall height, and the velocity ratio of the jets to the freestream velocity. To determine the performance of each configuration, measurements were made of the flow uniformity, of the turbulence intensity and decay rate of the turbulence, and of the turbulence integral length scale. The turbulence generator was required to have reasonable uniformity in the mean and turbulence intensity profiles in the spanwise and normal directions. Maximum turbulence levels with a slow decay rate were sought.

Tests were conducted at three velocity ratios, $VR = 3.7, 5.3$, and 7.8^* . In each case the flow was highly nonuniform in the near hole region. Vertical profiles of the mean velocity and turbulence intensity at the center of the spanwise width are shown in Figure 3.8 for two distances downstream, $x/D = 28$ and 87 . This test was done using $VR = 5.3$, hole diameter $D = 6.35$ mm, hole spacing $S/D = 1.5$, and a top plate height of $H/D = 11$. At $x/D = 28$ the profiles were highly nonuniform, but by $x/D = 87$ the mean velocity and turbulence intensity profiles were both uniform within $\pm 10\%$. Similar results were obtained at the lower and higher velocity ratios. Increasing the

* Velocity ratios indicated in the Thesis by Whan-Tong, (1991) ; $VR = 3, 4$, and 5 , were in error because they were based on the upstream velocity which was not equal to the mainstream velocity passing through the jets.

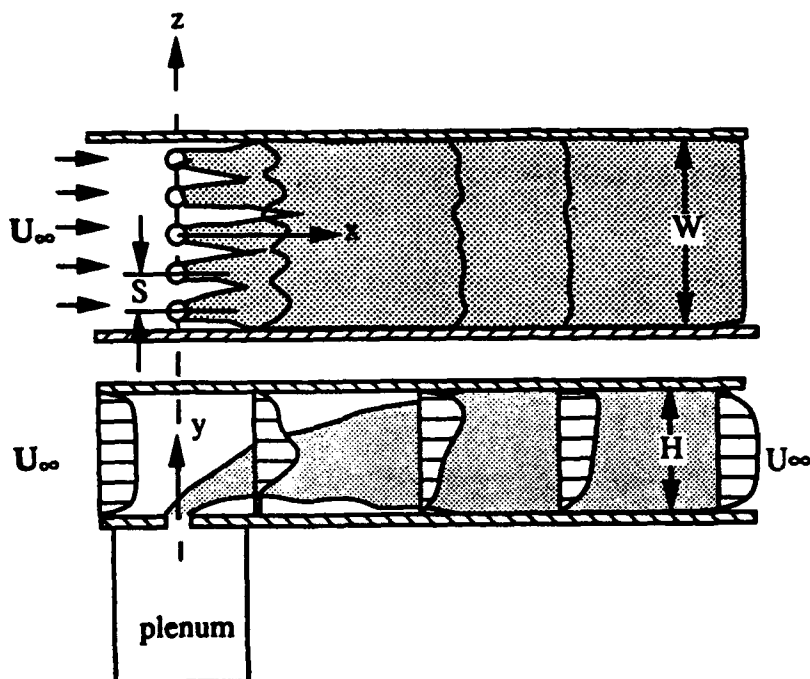
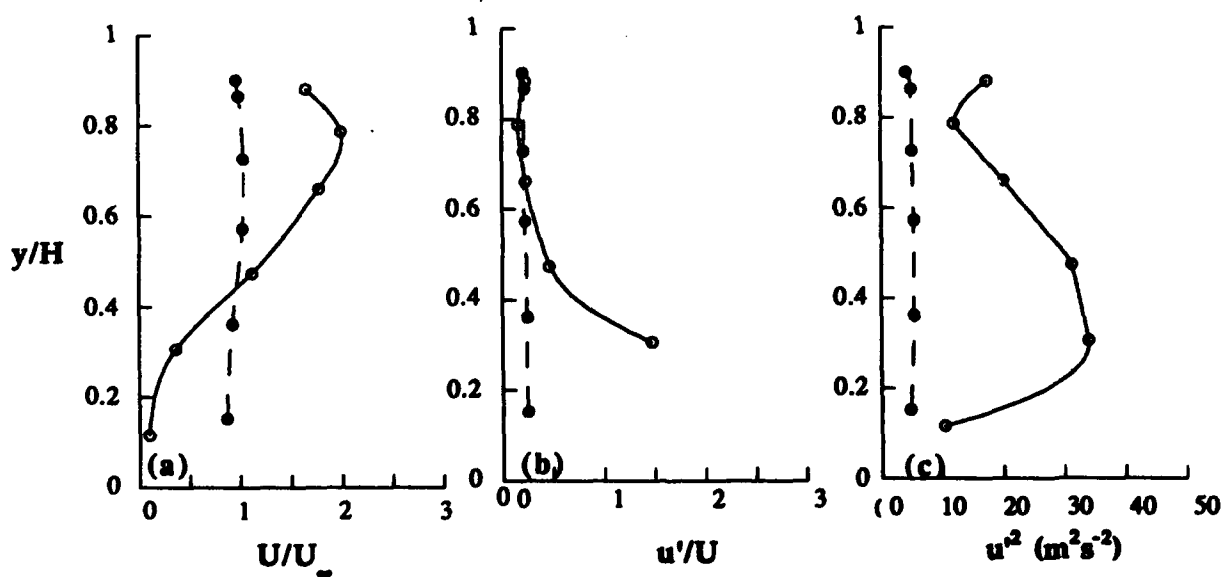


Figure 3.7 Schematic of mean velocity profile evolution in water channel.



Figures 3.8 a) Mean velocity profiles, b) Turbulence intensity profiles, c) Kinetic Energy profiles at $z/D = 0$ and $x/D = 28$ and 87 .

hole spacing to $S/D = 3$ had the effect of slightly decreasing the vertical and spanwise uniformity.

Preliminary measurements were made without using a top plate above the row of cross jets. Results from these measurements indicated that the flow field would be highly nonuniform when the jets are unconstrained. A top plate was added and the effect of the top plate height was tested using the large diameter holes, $D = 12.7$ mm. The top plate was placed at $H = 70$ mm and 140 mm corresponding to ratios of $H/D = 5.5$ and 11, respectively. Mean velocity and turbulence intensity uniformities were measured at $x = 560$ mm ($x/D = 45$). The lower top plate height was found to give significantly better uniformity. In fact, the uniformity of the mean velocity and turbulence intensity vertical profiles for the lower height was significantly better than that for the small diameter holes at the same streamwise distance and with the top plate height. All experiments with the small holes, $D = 6.35$ mm, were conducted with a top plate height of $H = 70$ mm and, therefore, a height-to-diameter ratio of $H/D = 11$. Turbulence levels for the smaller holes at similar x/D positions were significantly less than obtained with the large holes. This result indicates that the hole diameter does not appropriately scale the plate height and/or the turbulence decay rate.

Turbulence intensity levels and decay rates were strongly dependent on the velocity ratio as shown by measurements at the mid-height and mid-span of the channel flow shown in Figure 3.9. Larger velocity ratios resulted in higher turbulence levels, but the decay rate was greater for the higher turbulence levels. Measurements were not made far enough downstream to determine whether turbulence generated with larger velocity ratios would eventually fall to the same level, or lower levels, than turbulence generated with lower velocity ratios. Increasing the spacing between holes was found to significantly decrease turbulence levels. Increasing the top plate height was found to substantially increase turbulence levels, but uniformity greatly deteriorated. Figure 3.10 shows the effect of using larger diameter holes with constant H . In terms of the dimensional distance downstream, turbulence levels were initially much higher for the larger diameter holes, but rapidly decayed to the same level as that for the small diameter holes. When compared in terms of nondimensional x/D , the turbulence levels are initially

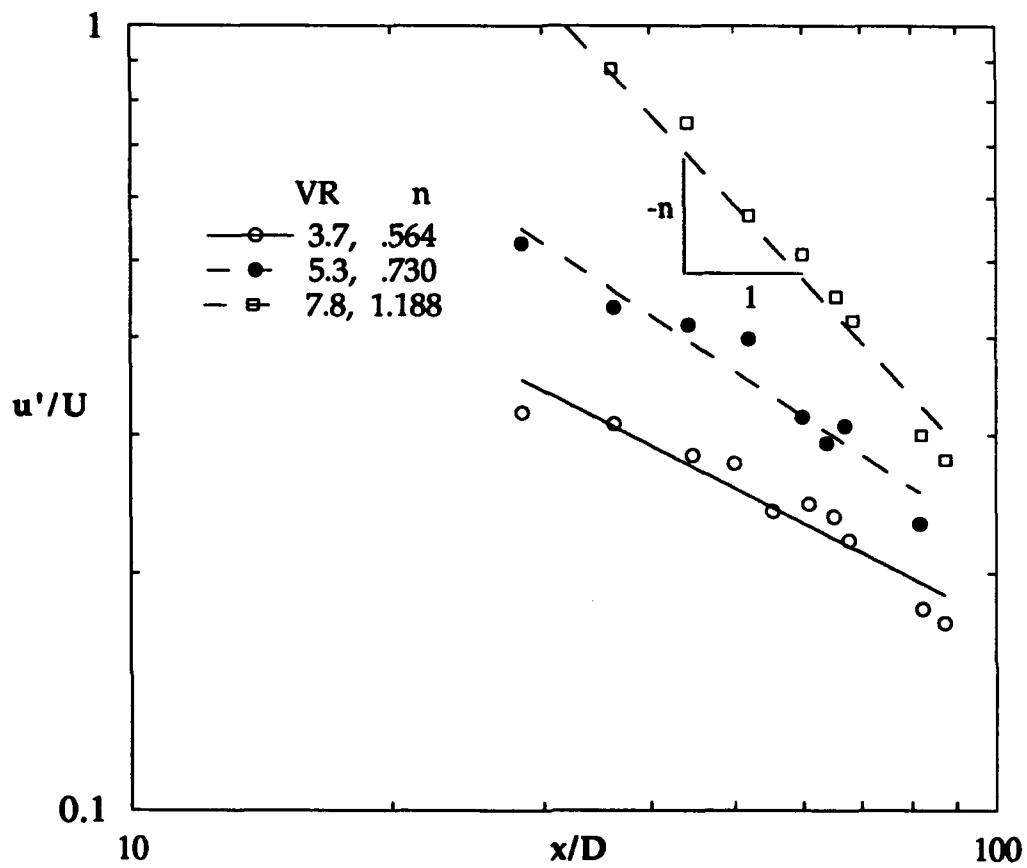


Figure 3.9 Streamwise turbulence intensity decay comparing velocity ratios.

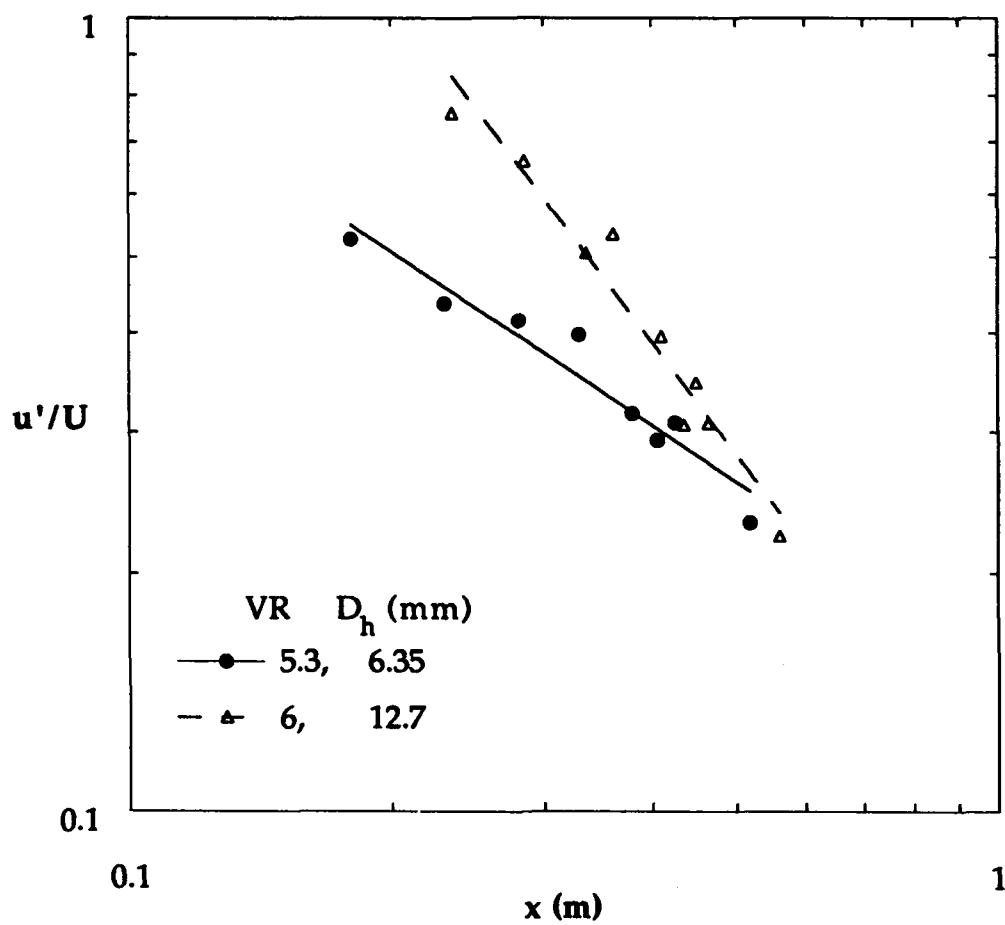


Figure 3.10 Streamwise turbulence intensity decay comparing jet hole diameters.

the same for the two cases, but decay rate for the large diameter holes is much greater resulting in significantly lower turbulence levels downstream.

Integral length scales of the turbulence were measured at various streamwise positions at the mid-height and mid-span of the channel flow. The effect of velocity ratio and hole diameter on the integral length scale was investigated. Figure 3.11(a) shows that varying the velocity ratio from $VR = 3.7$ to 7.8 had essentially no effect on the integral length scale. Figure 3.11(b) shows that increasing the hole diameter from $D = 6.35$ mm to 12.7 mm also had essentially no effect on the integral length scale.

In summary, the turbulence intensity levels and decay rates were strongly dependent on the velocity ratio with higher turbulence levels occurring at higher velocity ratios. However, the decay rate was greater for the higher turbulence levels. In evaluating the hole diameter, the decay rate, in terms of x/D , for the larger hole diameters is much greater. The velocity profiles are highly nonuniform in the vicinity of the jet holes, but by $x/D = 87$ the mean velocity and turbulence intensity profiles become uniform to within $\pm 10\%$ with a hole spacing of $S/D = 1.5$. Varying either the velocity ratio or hole diameter in the range which we studied, had essentially no effect on the integral length scale.

3.4 High-Freestream Turbulence Wind Tunnel Tests

The results from the water channel tests were used in the initial design of the jets in cross-stream configuration for the wind tunnel. In designing the turbulence generator for the wind tunnel we wanted not only to achieve high turbulence levels, but also a uniform mean flowfield, and have turbulent length scales on the order of the boundary layer thickness. This section of the report discusses primarily the second phase of the turbulence generator development which includes the initial design, the refinements made to the turbulence generator, the resulting turbulence field in terms of the decay rates and length scales, and the capabilities of the turbulence generator at different velocity ratios.

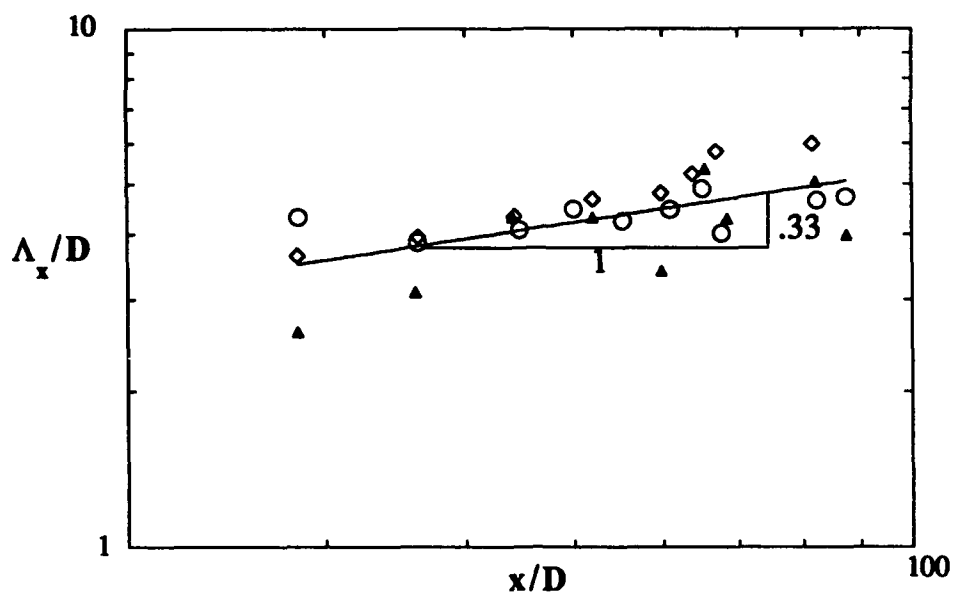


Figure 3.11a Effect of velocity ratio on integral length scale growth
VR = \circ 3.7, \diamond 5.3, \triangle 7.8.

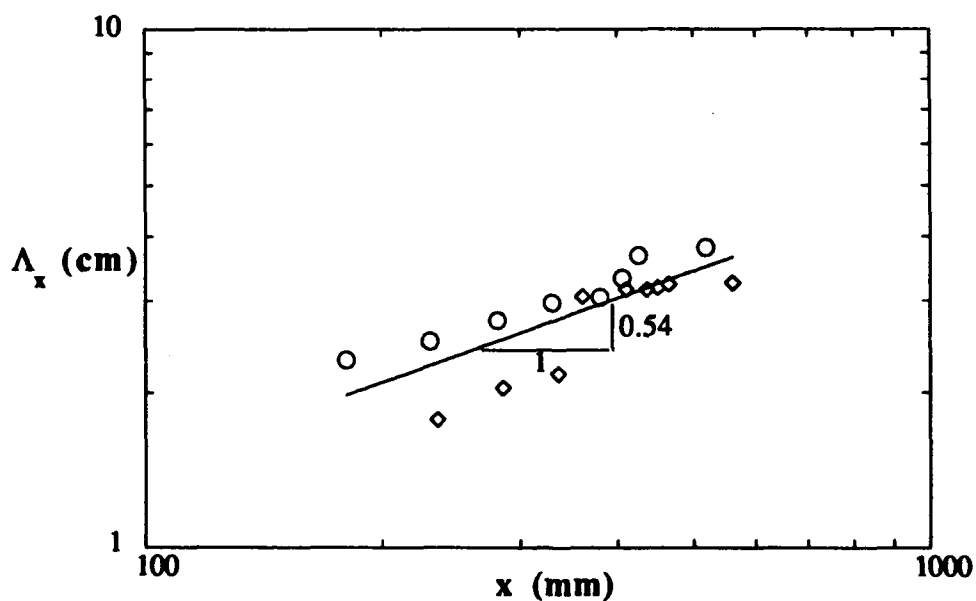


Figure 3.11b Effect of diameter size on integral length scale growth
VR = 5.3, D = \circ 6.35 mm \diamond 12.7 mm.

Based on the water channel studies, the critical parameters that needed to be matched for the wind tunnel design were the spacing-to-hole diameter ratio, S/D , the channel height-to-hole diameter ratio, H/D , and the jet-to-mainstream velocity ratio, VR . A schematic of the turbulence generator installed in the wind tunnel is shown in Figure 3.12. The streamwise distance between the jet holes and the test surface was chosen based on uniform mean and turbulence profiles being measured in the water channel at an $x/D = 87$. One of the design constraints was the flowrate characteristics of the blower which was to provide the secondary flow for the jets. Initially, our laboratory acquired a 1.5 hp, axial fan at no cost from a surplus warehouse. The flowrate/pressure drop characteristics for this fan were used in the initial turbulence generator design.

The water channel tests indicated that an $S/D = 1.5$ were needed to maintain lateral uniformity for the mean velocity and thus, was chosen for the wind tunnel. In order to maintain vertical symmetry, represented by the top plate in the water channel tests, jet holes needed to be placed on both the top and bottom of the wind tunnel test section. The water channel tests indicated that higher turbulence levels occurred with the larger H/D ratio and a more rapid turbulence decay with the larger diameter holes. The hole diameter for the turbulence generator was chosen to be 5.08 mm which gives an $H/D = 15$. Results from the water channel also indicated that a velocity ratio of 5 was sufficient to give the high turbulence levels.

The initial tests were completed and high turbulence levels were achieved in the wind tunnel, as documented in the Whan-Tong (1991) thesis. In order to achieve the high turbulence levels, the mainstream velocity was reduced to nominally 4 - 5 m/s because the blowing ratio needed in the wind tunnel was much higher ($VR = 9$) than that indicated by the water channel data. The need for a higher blowing ratio was primarily because the turbulence levels not only scale with blowing ratio but also the Reynolds number, Re_p , based on the upstream velocity and the jet hole diameter. For example, as Reynolds number is increased the turbulence levels achieved at the same velocity ratio are reduced. The data that show this effect will be discussed at the end of this section after the improvements that were made to the wind tunnel

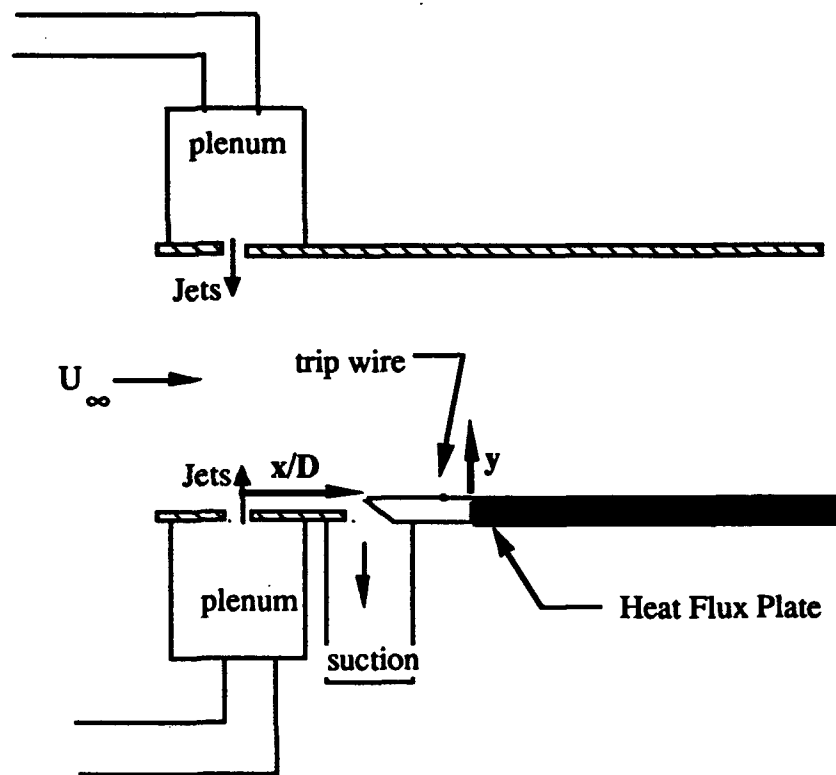


Figure 3.12 Schematic of the wind tunnel turbulence generator.

turbulence generator design are explained. The water channel data were run at a $Re_D = 500$ and high turbulence levels were achieved at a $VR = 5$, whereas in the wind tunnel the $Re_D = 1330$ and the high turbulence levels required a $VR = 9$.

After the initial tests were completed, improvements to the turbulence generator began. One of the major goals in improving the turbulence generator was to have high turbulence levels at a faster mainstream velocity. The mainstream velocity that the initial high freestream turbulence tests were done was nominally 4 - 5 m/s. A higher mainstream velocity results in an increased percentage of convective heat transfer relative to radiative heat transfer, hence requiring a smaller radiation correction. The second goal was to obtain a uniform mean velocity field in both the vertical and lateral directions for the highly turbulent flowfield.

The first goal was accomplished by installing a 7.5-hp blower with much larger pressure drop/flowrate capabilities than the original fan. However, our experiments indicated that the turbulence level did not scale with velocity ratio alone. At higher freestream velocities, nominally 7 - 8 m/s, a higher velocity ratio was required to achieve the same turbulence levels. Turbulence levels of 20% at an $x/D = 130$ were obtained at a $VR = 11$. Although high turbulence levels were achieved, the spanwise mean velocity was highly non-uniform.

The second goal, achieving the uniform mean flowfield, required several iterations in the generator design. Initially, we determined that an $S/D = 3$ gave better lateral uniformity with no loss in turbulence levels than an $S/D = 1.5$. Even with this improvement, the mean field was still quite non-uniform. The two major causes of the nonuniformity were gaps at the spanwise edges of the test section where there were no jet holes, and the interaction between the top and bottom jets.

The original design of the jet hole plates on the bottom and top of the wind tunnel allowed for a 57-mm side gap on the outer edges of the tunnel. These gaps were in the original design for simplicity since no changes to the test section supports were required. However, these gaps provided a low

resistance path for the mainstream flow. The design was modified by adding holes such that the hole pattern continued out to the wind tunnel edges.

The interaction between the top and bottom row of jet holes was eliminated by installing a splitter plate at the vertical centerline of the tunnel. The splitter plate is 1.6 mm thick and extends 25 cm upstream and 15 cm downstream of the jet holes. In improving the lateral uniformity, even higher velocity ratios were required to achieve high turbulence levels. Figure 3.13 shows the lateral velocity profiles before and after improving the turbulence generator design. In the improved flowfield, the required velocity ratio was $VR = 17$ (at $Re_D = 1700$) which represents a 20% increase in mass to the mainstream flow. These profiles were taken at a streamwise distance of $x/D = 130$ which is the streamwise location on the heat flux test plate where there are no longer unheated starting length effects.

After improving the lateral uniformity of the mean velocity field, the turbulent length scales were measured. Figure 3.14 gives the measured length scales deduced from the autocorrelation time scales and the convective velocity. The length scales measured in the water channel were nominally on the order of the boundary layer thickness which was the desired scale. Similarly, those length scales measured in the wind tunnel were on the order of the boundary layer thickness. Also shown in Figure 3.14 is the curve fit slope for the growth rate of the length scales measured by Comte-Bellot and Corrsin (1966) for grid-generated turbulence. The growth rate of the turbulent length scales agree well with the grid-generated length scale growth rate. The decay rate for the highly turbulent flowfield is shown in Figure 3.15. Again, the decay rate is quite similar to that of grid-generated turbulence; however, the turbulence levels are much higher.

The turbulence levels that can be achieved using this turbulence generator are both a function of the jet Reynolds number, Re_D , and jet-to-mainstream velocity ratio, VR . Figure 3.16 shows the turbulence decay rates as a function of streamwise distance measured relative to the jet holes at different Reynolds numbers and VR . As Re_D increases, the turbulence levels drop at

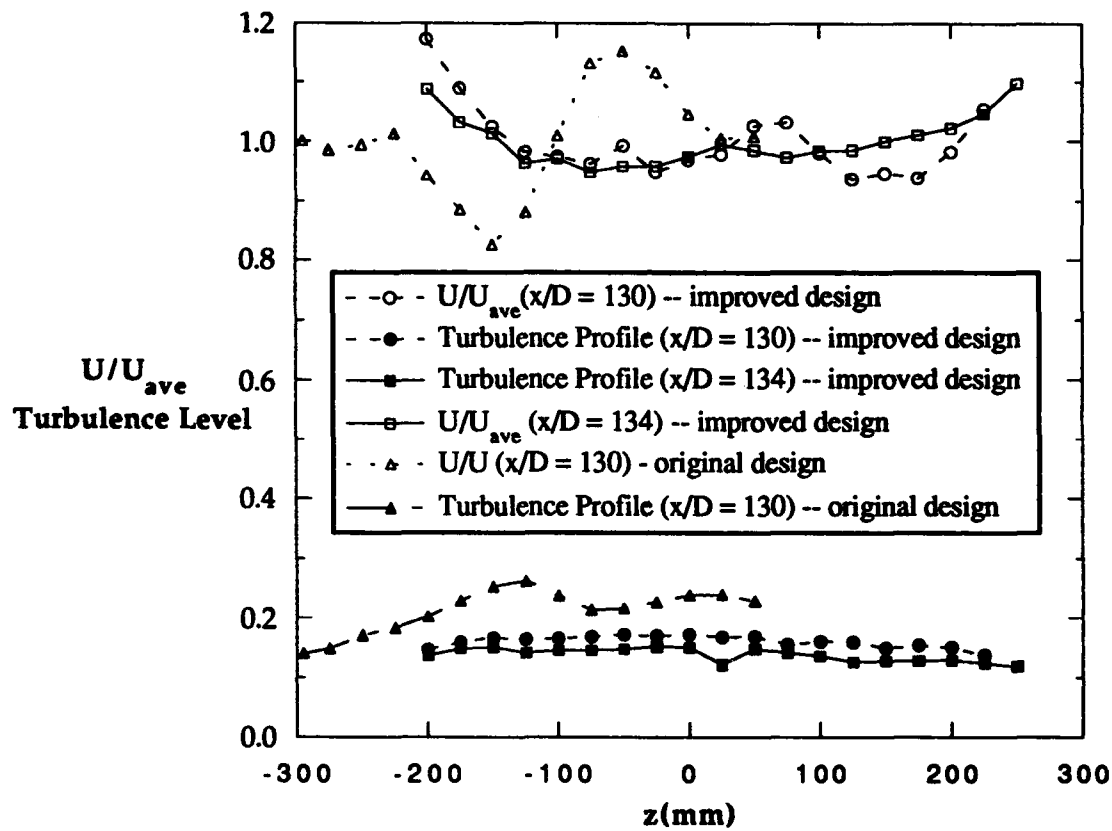


Figure 3.13 Spanwise uniformity of highly turbulent flowfield before and after improvements. These profiles were acquired at $x/D = 130, 134$ from holes.

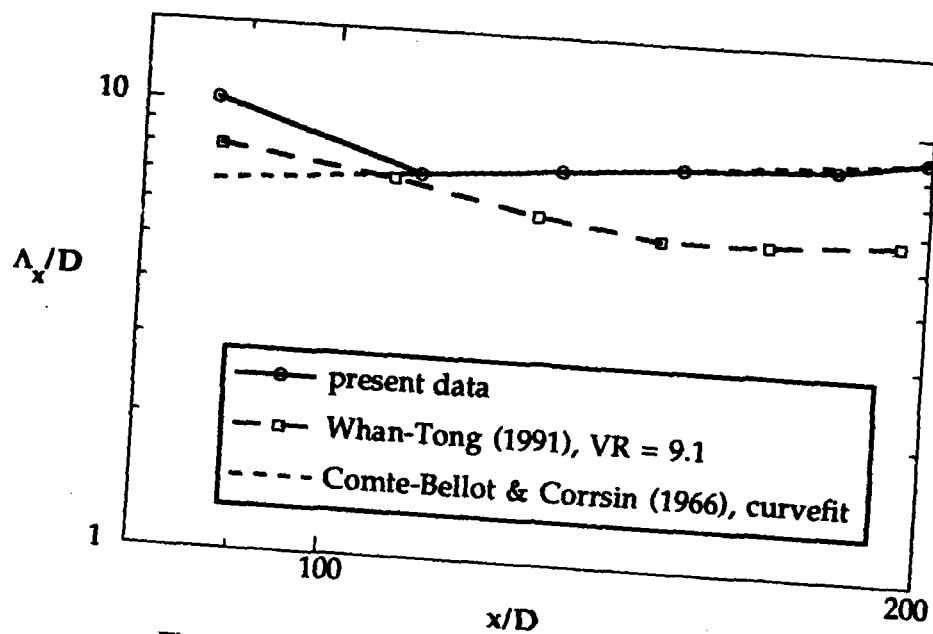


Figure 3.14 Streamwise length scales for the highly turbulent flowfield as compared with Whan-Tong's (1991) length scales and grid turbulence growth based on x/M .

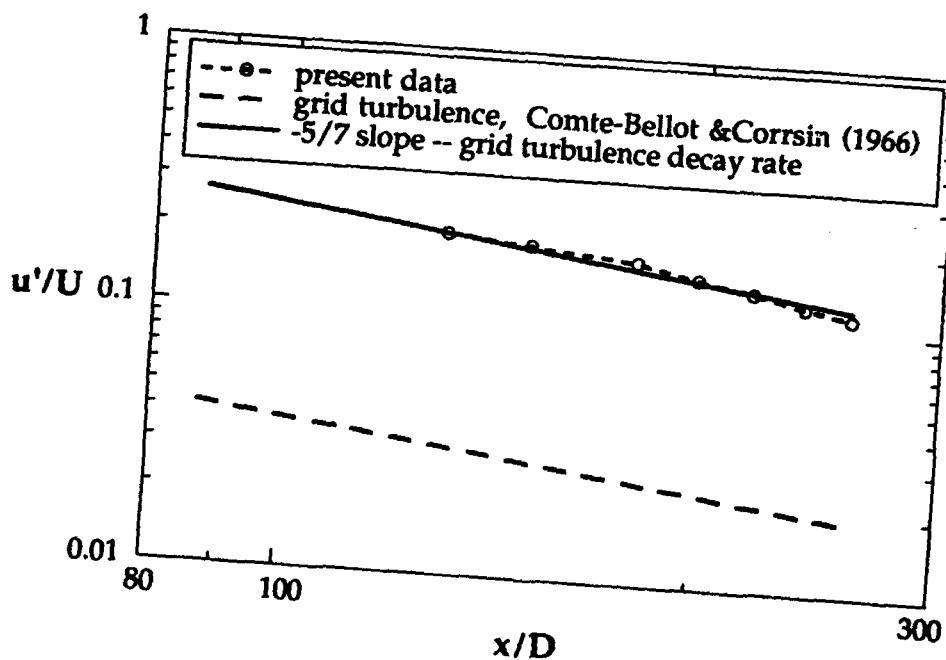


Figure 3.15 Turbulence level decay rate as compared with grid turbulence rate and grid turbulence levels.

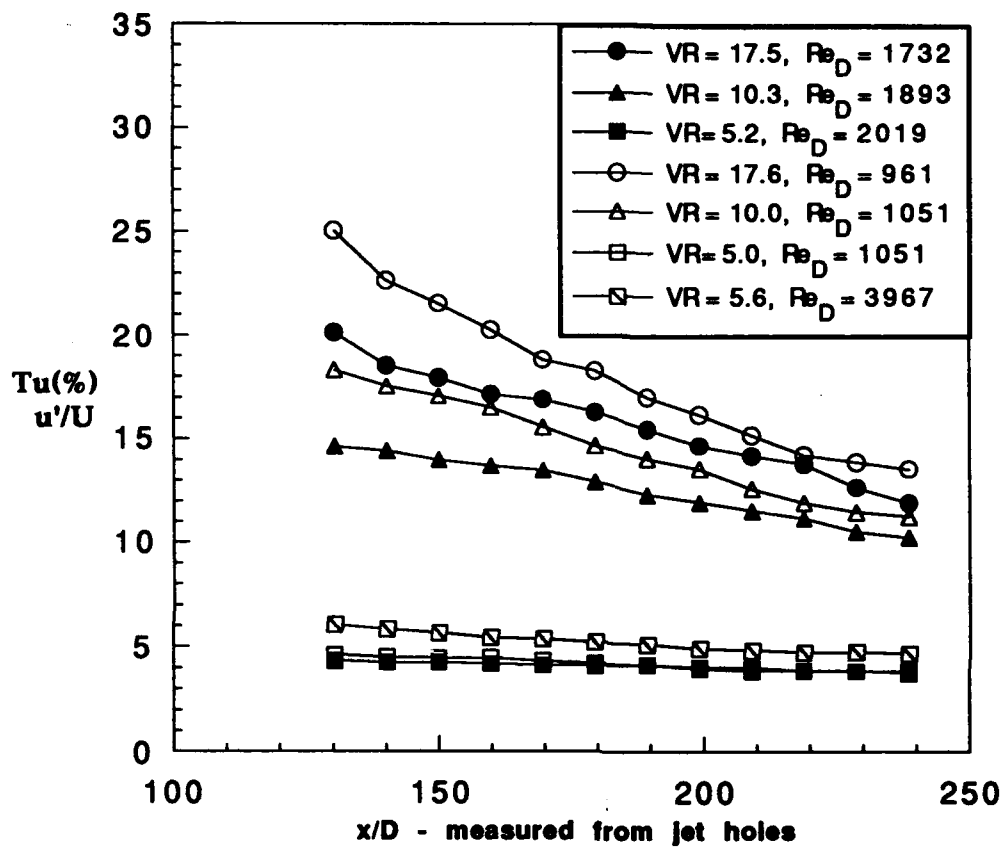


Figure 3.16 Streamwise decay of turbulence levels as a function of jet-to-mainstream velocity ratio and jet Reynolds number.

velocity ratios of $VR = 17.5$ and 10 , but remain relatively constant for a velocity ratio of $VR = 5$.

In summary, high turbulence levels could be achieved using the original design of the wind tunnel turbulence generator which was based on the water channel data. However, refinements were needed to achieve faster freestream velocities with a uniform mean flowfield. After these refinements were made, sufficiently high turbulence levels, $Tu = 20\%$, were achieved at a freestream velocity of 8 m/s . The turbulent length scales in this turbulent flowfield are on the order of the boundary layer thickness. Different turbulence levels can be achieved with this generator. However, the turbulence level is not only a function of velocity ratio but also the Reynolds number.

4. Development of a Simultaneous Temperature/Velocity Probe

In order to resolve temperature fluctuations and temperature-velocity correlations in the heated boundary layer, a fast responding temperature probe was needed. Two concepts for obtaining simultaneous temperature and velocity measurements with a high frequency response temperature sensor were investigated. The first concept involved using a cold-wire probe simultaneously with the LDV system. In the second concept, a hot-wire probe with a low over-heat ratio was used simultaneously with the LDV system. Using a cold-wire probe has the advantage of giving an output signal directly proportional to the fluid temperature with negligible sensitivity to velocity, but the wire diameter must be less than 1 μm in diameter to have sufficient frequency response. We were particularly concerned about the use of the cold-wire probe with the LDV system (which has never been done before) because of the possibility of the LDV seed particles breaking the submicron wire. The hot-wire probe has the advantage of good frequency response with a relatively large diameter wire which would be less susceptible to breaking, but requires special signal processing to educe the fluid temperature from the output which is sensitive to temperature and velocity.

4.1 Hot-wire/LDV Measurements

Use of a hot-wire probe simultaneously with LDV measurements to obtain temperature measurements was first evaluated. This technique is similar to techniques used previously by Blair and Bennett (1987) who used a multisensor hot-wire probe with the sensors operated at different over-heat ratios. Because of the different relative sensitivity of the hot-wire sensors to temperature and velocity, both temperature and velocity could be resolved from differences in sensor outputs. Simultaneous hot-wire and LDV measurements have a definite advantage over the multiple hot-wire technique because the LDV is sensitive only to velocity which results in more accurate measurement of velocity and temperature.

To implement the hot-wire/LDV technique for temperature measurements, calibration experiments were conducted to establish the appropriate over-heat ratio to obtain good temperature sensitivity while maintaining good frequency response. Based on these tests an over-heat ratio of 1.05 was found to give accurate temperature measurements with a frequency response of nominally 10 kHz. Following this, a signal processing algorithm for educing the temperature from a hot-wire signal, given the simultaneous LDV measurement of the velocity, was developed and evaluated. Although the general principle of the hot-wire/LDV technique for temperature measurements was proved by these tests, the complete system was not evaluated in this project because the cold-wire/LDV technique proved to be successful (as described below) and was implemented instead.

4.2 Cold-wire/LDV Measurements

As discussed previously, high frequency response from a cold-wire requires a very small wire diameter. Typical wire diameters that have been used range from 2.5 μm , used by Chen and Blackwelder (1978) to 0.64 μm , used in various studies by Antonia (e.g., Antonia and Browne, 1987). The capability of both constructing and operating cold-wires with diameters of 5 μm , 2.5 μm , 1.5 μm , and 0.64 μm was developed as a part of this project. The frequency responses of four different wire diameters were measured at three different freestream velocities. To determine the frequency response, a square-wave energy flux input was imposed on the cold-wire using a laser beam which was focussed on the wire and interrupted with a rotating chopper blade. The cold-wire response to the square wave input was observed on the oscilloscope and the frequency response was deduced from the measured relaxation time constant. For the 5- μm and 2.5- μm -diameter wires, the frequency response was also measured using a less direct method that involved deducing the cold-wire response based on the response of the wire in a hot-wire circuit using an external electronic sine wave input to the anemometer. Measured frequency responses for the four different wire diameters at different freestream velocities are shown in Figure 4.1. These measurements were found to correspond well with predictions based on a energy balance between the thermal capacitance of the wire and the convective heat flux.

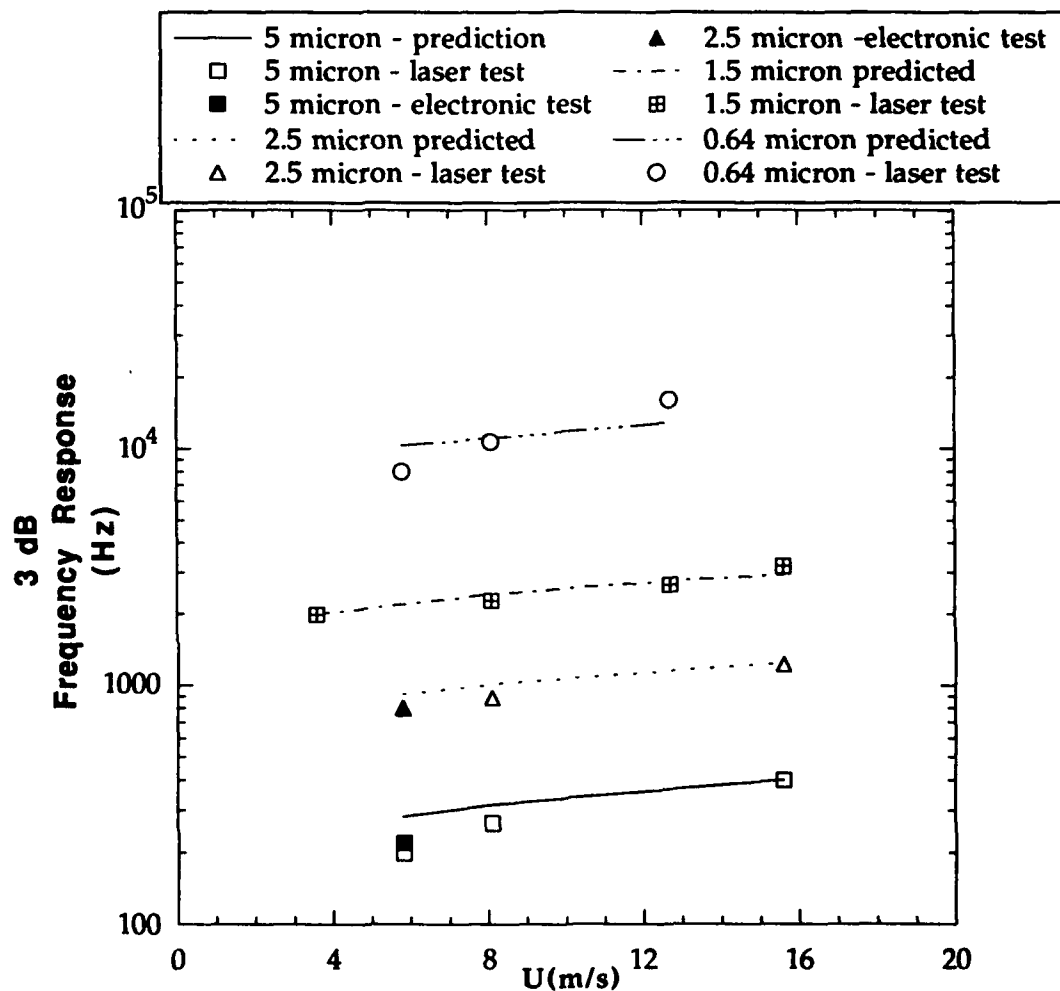


Figure 4.1 Measured frequency response for several different wire diameters and freestream velocities.

The spectrum of temperature fluctuations in the log-region of a heated turbulent boundary layer was measured with a 0.64- μm wire to determine the maximum frequency response needed. This spectral analysis showed a 60-dB decrease in the amplitude of temperature fluctuations at a frequency of 2600 Hz. These results indicated a need for a frequency response greater than 3 kHz, and hence a probe diameter of 1.5 μm or 0.64 μm .

Simultaneous temperature/velocity measurements required placement of the LDV probe volume immediately upstream of the cold-wire sensor at a distance small enough such that there would be negligible loss in correlation between the sensors. The maximum allowable distance between the LDV and cold-wire was 0.5 mm. This estimate was based on the delay time in which autocorrelation coefficient measurement fell to $R_{uu} = 0.98$ and the corresponding convection velocity. For all simultaneous temperature and velocity measurements presented in this report, the LDV probe volume was placed within 0.3 mm of the cold-wire sensor.

Verification of the capability for simultaneous temperature and velocity measurements was done first by showing good velocity correlation between the LDV and a hot-wire for measurements within the boundary layer, and second by comparing measurements of temperature-velocity correlations in a heated turbulent boundary layer with data in the literature. With the simultaneous hot-wire and LDV measurements, both sensors are sensitive to nominally the streamwise U component of velocity (the hot-wire is actually sensitive to the total velocity with both U and V components) so that the cross-correlation coefficient between these signals should ideally be $(R_{uu})_{12} = 1.0$ if the sensors are close enough. Recall that the data acquisition process developed for these simultaneous measurements had a 30- μs time delay between the analog input (hot-wire or cold-wire) and LDV input (discussed in Chapter 2). Given a distance between the LDV probe volume and the hot-wire sensor of 0.3 mm, and a nominal convection velocity of 10 m/s, this data acquisition lag time corresponds to the convection time from the LDV probe volume to the hot-wire sensor. Consequently, maximum correlation is expected for this configuration. The two-point velocity cross-correlation coefficient between the LDV and hot-wire was measured to be $(R_{uu})_{12} = 0.95$.

This correlation coefficient was reasonably close to the ideal level of $(R_{uu})_{12} = 1.0$. We believe that the 5% decrease in the measured level is due to the slightly different sensitivities between the LDV and hot-wire.

For the second step in verifying our simultaneous measurement capability, velocity/temperature correlation coefficients, R_{ut} and R_{vt} , were measured across a heated turbulent boundary layer with minimal freestream turbulence level ($Tu < 0.5\%$) and at $Re_\theta = 1640$. Because of the difficulty of these measurements, very few results are available in the literature. Moreover, as noted by Subramanian and Antonia (1981), results in the literature vary by as much as 50% for both R_{ut} and R_{vt} . The most reliable results in the literature appear to come from the work of Subramanian and Antonia (1981) and Chen and Blackwelder (1978). Subramanian and Antonia used a $0.63\text{-}\mu\text{m}$ cold-wire located 1.2 mm upstream of X-configured hot-wire probe. Chen and Blackwelder used a similar configuration, but their cold-wire sensor was $2.5\text{ }\mu\text{m}$ in diameter thereby having a lower frequency response than the $0.64\text{-}\mu\text{m}$ wire. Use of the cold-wire/hot-wire configuration also has the disadvantage of interference effects among the sensors and the need for corrections to the hot-wire data due to temperature contamination. These limitations do not occur with the cold-wire/LDV system developed in this project. Although these two studies are the most reliable found in the literature, they reported velocity correlation coefficients, R_{uv} , which are somewhat greater in magnitude than the maximum correlation value being $R_{uv} = -0.45$ generally measured in isothermal studies. Subramanian and Antonia report correlations of $R_{uv} = -0.5$ at a $Re_\theta = 1500$ and Chen and Blackwelder report values of $R_{uv} = -0.52$ at a $Re_\theta = 2800$. Since the cold-wire/LDV system measures velocity correlations without any type of probe interference or required temperature correction, our measurement of $R_{uv} = -0.43$ throughout the boundary layer is consistent with data in the literature.

Results from our measurements are compared with those of Subramanian and Antonia (1981) and Chen and Blackwelder (1978) in Figure 4.2. R_{ut} values from our measurements were very similar to those of Chen and Blackwelder who also measured $R_{ut} = -0.6$ across most of the boundary layer. However, Subramanian and Antonia measured significantly higher correlations, $R_{ut} = -$

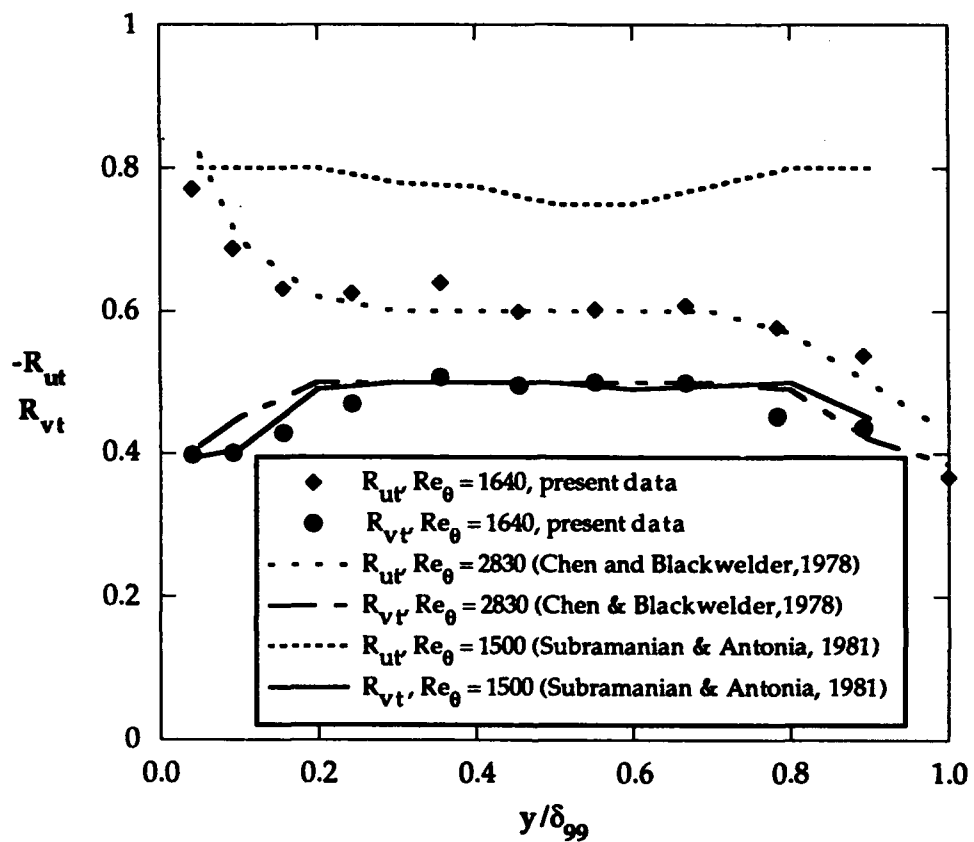


Figure 4.2 Comparison of velocity/temperature correlations with those given in the literature.

0.8, across most of the boundary layer. Our measured vertical velocity/temperature correlations, R_{vt} , were similar to both those of Subramanian and Antonia and Chen and Blackwelder throughout the boundary layer, $R_{vt} = -0.5$.

5. Film Cooling Thermal Field

The objective of this phase of the project was to determine the dynamics of the interaction of the film cooling jet with the mainstream and the diffusion characteristics of the film cooling jet. In particular, we were interested in how the jet dynamics were related to the momentum flux ratio (I), the velocity ratio (VR), and the mass flux ratio (M). This objective was accomplished by making a detailed mapping of the thermal field above the injection hole and for a short distance downstream of the hole.

Details of the facilities, instrumentation, experimental procedures, results, and conclusions from this phase of the project are given in the paper *Mean Temperature Measurements of Jets with Crossflow for Gas Turbine Film Cooling Application* by Thole et al. (1990) which is included in Appendix A. A brief description is given below.

5.1 Facilities, Instrumentation, and Experimental Plan

Experiments were performed in the TTCRL film cooling simulation wind tunnel as described in section 2.1. A flat test plate was used with a single row of inclined holes. A secondary flow loop provided air for the film cooling jets. Liquid nitrogen was used to cryogenically cool the air in the secondary flow loop to temperatures as low as 150K which resulted in jet to mainstream density ratios up to $DR = 2.0$.

The test plate had a row of 11 holes, 12.7 mm in diameter and spaced 3 diameters apart in the spanwise direction. The holes, having a length-to-diameter ratio of 3.5, were inclined at 35 degrees and located 19 diameters downstream of the leading edge of the test plate. The test plate and plenum chamber were constructed from a glass reinforced plastic material (commercially known as EXTREN) with low thermal expansion coefficient ($\alpha = 1.4 \times 10^{-5} /K$) and relatively low thermal conductivity ($k = 0.58 \text{ W/m}\cdot\text{K}$).

Mean temperatures were measured with a 4- μm -diameter cold-wire probe. This probe was traversed along the centerline of one of the film cooling holes from the upstream edge of the hole to 10 diameters downstream.

An experimental program was formulated to independently evaluate the effect of momentum flux ratio, velocity ratio, and mass flux ratio. Nine experiments were performed with a range parameters as indicated in Table 5.1.

Table 5.1. Range of Experimental Parameters

Case	Momentum Flux Ratio	Density Ratio	Velocity Ratio	Mass Flux Ratio
1	0.125	2.0	0.25	0.5
2	0.35	1.4	0.5	0.7
3	0.4	1.6	0.5	0.8
4	0.5	2.0	0.5	1.0
5	0.5	1.2	0.65	0.78
6	0.5	1.6	0.56	0.89
7	0.63	1.6	0.63	1.0
8	0.83	1.2	0.83	1.0
9	2.0	2.0	2.0	2.0

Mean temperature data, normalized using the freestream and jet exit temperatures, are presented in terms of the nondimensional parameter, θ , defined as follows:

$$\theta = \frac{T - T_{\infty}}{T_j - T_{\infty}} \quad (5.1)$$

5.2 Results and Conclusions

The primary result from these experiments was establishing conditions for which the jets remain attached to the wall, or detached but then reattached to the wall, or completely detached from the wall. Whether the jets were attached to or detached from the wall was determined from the temperature profiles. The position of the jet is most clearly evident from the non-dimensional temperature contours as shown in Figures 5.1, 5.2, and 5.3. Jets which remain attached to the wall are evident from the contour plots where the maximum θ remains at the wall for an $I = 0.125$ as shown in Figure 5.1. As the momentum flux ratio increases to $I = 0.5$, the contour plot, as shown in Figure 5.2, shows that the jet initially detaches which is evident from the maximum θ occurring well above the wall between $x/D = 2$ and 4. Beyond $x/D = 6$, in Figure 5.2, the maximum θ has returned to the wall indicating that the jet has reattached to the wall. At an even higher momentum flux ratio, $I = 2.0$, as shown in Figure 5.3, the trajectory of the jet as indicated by the location of the maximum θ value clearly shows a fully detached jet.

From the series of experiments listed in Table 5.1, three regimes in terms of the jet attachment/detachment characteristics were identified. In the low momentum flux ratio regime, which occurred for $I < 0.4$, the jet remained attached to the wall. For the intermediate momentum flux ratio regime, $0.4 < I < 0.8$, the jet initially detaches from the wall, but reattaches to the wall within several diameters downstream. The diffusion of the jet is not greatly affected by the detachment and later reattachment so that the cooling effectiveness remains comparable to jets which remained attached. In fact, because of the increased mass flux, jets in the intermediate momentum flux regime may have greater cooling effectiveness for $x/D > 10$. In the high

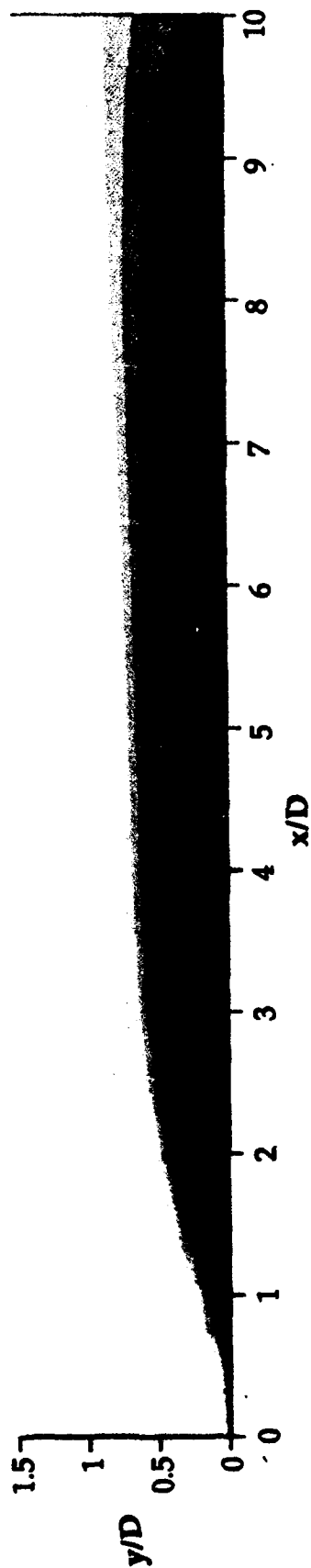
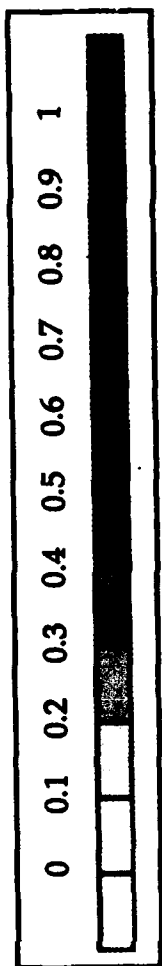


Figure 5.1 Dimensionless temperature contours along the jet centerline for $I = 0.125$, $DR = 2.0$, $VR = 0.25$, $M = 0.5$.

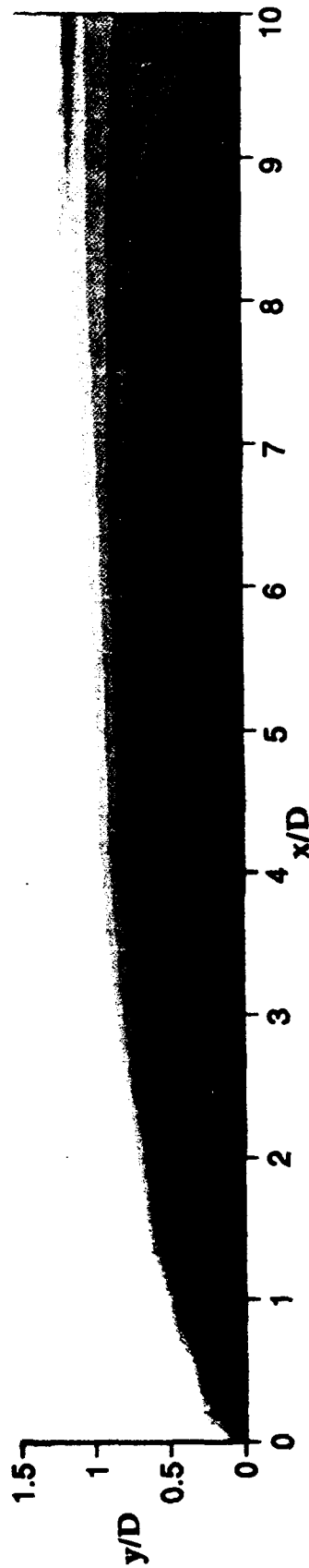


Figure 5.2 Dimensionless temperature contours along the jet centerline for $I = 0.5$, $DR = 2.0$, $VR = 0.50$, $M = 1.0$.

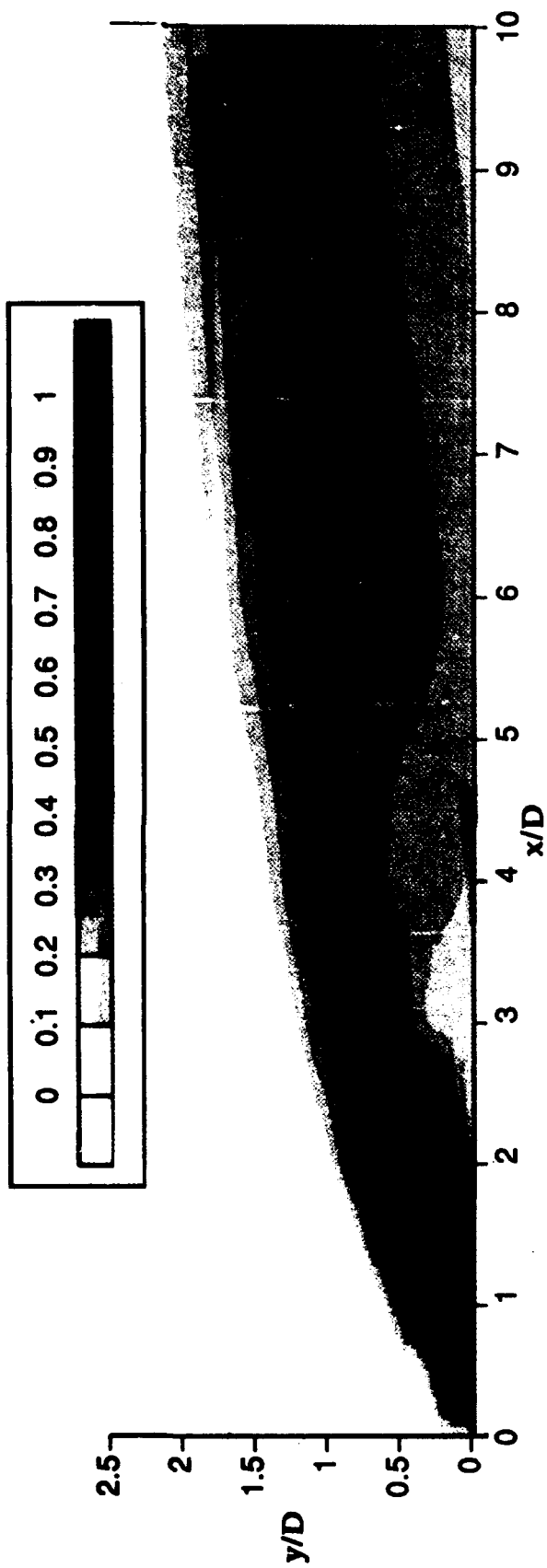


Figure 5.3 Dimensionless temperature contours along the jet centerline for $I = 2.0$, $DR = 2.0$, $VR = 1.0$, $M = 2.0$.

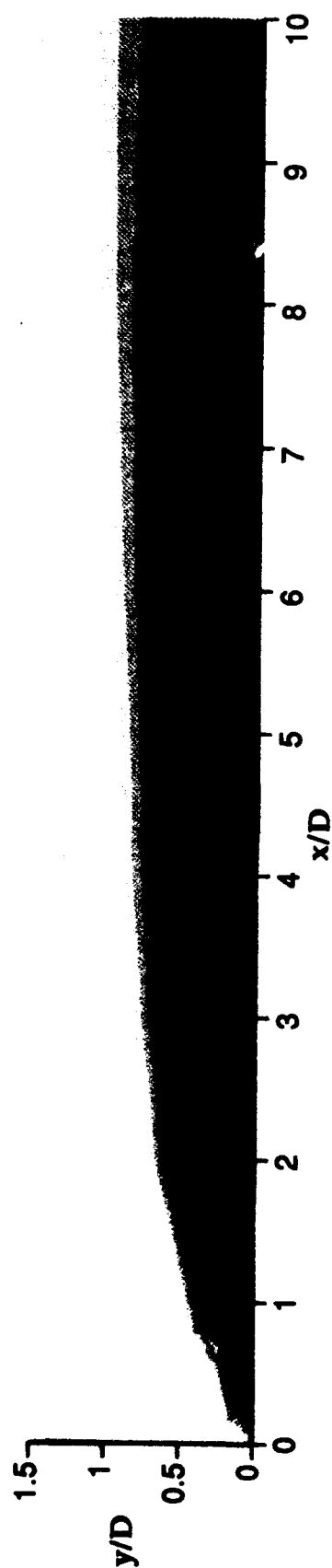


Figure 5.4 Dimensionless temperature contours along the jet centerline for $I = 0.5$, $DR = 1.2$, $VR = 0.65$, $M = 0.775$.

momentum flux ratio regime, $I > 0.8$, the jet detaches and remains detached from the wall. Obviously, this results in poor cooling effectiveness

By varying the density ratio from $DR = 1.2$ to 2.0 , the momentum flux ratio, the velocity ratio, and the mass flux ratio could be independently controlled. To determine which of these parameters is the appropriate scaling parameter for the jet attachment/detachment characteristics, the series of experiments listed in Table 5.1 were designed so that each parameter was held constant over the full range of density ratios. Results from these experiments clearly established that the attachment/detachment characteristics of the jets were dictated by the momentum flux ratio. For example, at a constant momentum flux ratio of $I = 0.5$ and a range of density ratios of $DR = 1.2$, as shown in Figure 5.4, and $DR = 2.0$, shown in Figure 5.2, the thermal fields show that the initial detachment of the jet and later reattachment remains virtually the same. Similar comparisons at constant velocity ratio and constant mass flux ratio showed distinct differences in the jet characteristics.

These results are consistent with the results of Sinha et al. (1991) who measured the adiabatic effectiveness for a similar range of density ratios. The detachment-reattachment of the jet, deduced from adiabatic effectiveness variations downstream of the hole, indicated a scaling with momentum flux ratio. Since the maximum effectiveness occurs when the jet is in this detachment/reattachment regime, use of the momentum flux ratio to establish maximum cooling effectiveness is of great practical importance.

6. Effect of Very High Freestream Turbulence on a Boundary Layer Flow

Effects of very high freestream turbulence on a boundary layer velocity field and surface heat flux were studied in the TTCRL boundary layer wind tunnel facility described in Section 2. The original configuration of the turbulence generator was used for these studies. As described in Section 3, the original configuration of the turbulence generator did not have a splitter plate between the top and bottom jets.

In many of the heat transfer correlations, either a turbulent autocorrelation length scale, Λ_x , or a turbulent dissipation length scale, L_u^ϵ , which is defined in Section 6.1, is used. For these studies turbulence levels ranged from $Tu = 24\%$ at $x_h = 20$ cm to $Tu = 12\%$ at $x_h = 80$ cm. The turbulent dissipation length scale and the integral scales were nominally $L_u^\epsilon = 90$ mm and $\Lambda_x = 30$ mm for the freestream turbulence, and the boundary layer thickness over the range of interest was on the order of 20 mm.

6.1 Surface Heat Flux

Details of the study on the effects of very high freestream turbulence on surface heat flux are given in the paper *Generation of Very High Freestream Turbulence Levels and the Effects on Heat Transfer* by Thole et al. (1991) which is included in Appendix B. A brief description of the most significant results is given below.

The enhancement of heat transfer for the highly turbulent flowfield as compared with the standard boundary layer benchmark data and with a standard boundary layer correlation (given by Kays and Crawford, 1980) is shown in Figure 6.1. The Stanton number distributions are given as a function of Reynolds number based on streamwise distance, Re_x , where x is measured from the virtual origin located 0.36 m upstream of the heat flux plate. The virtual origin was deduced from the measured momentum thickness. Freestream turbulence intensities over the range for which St data

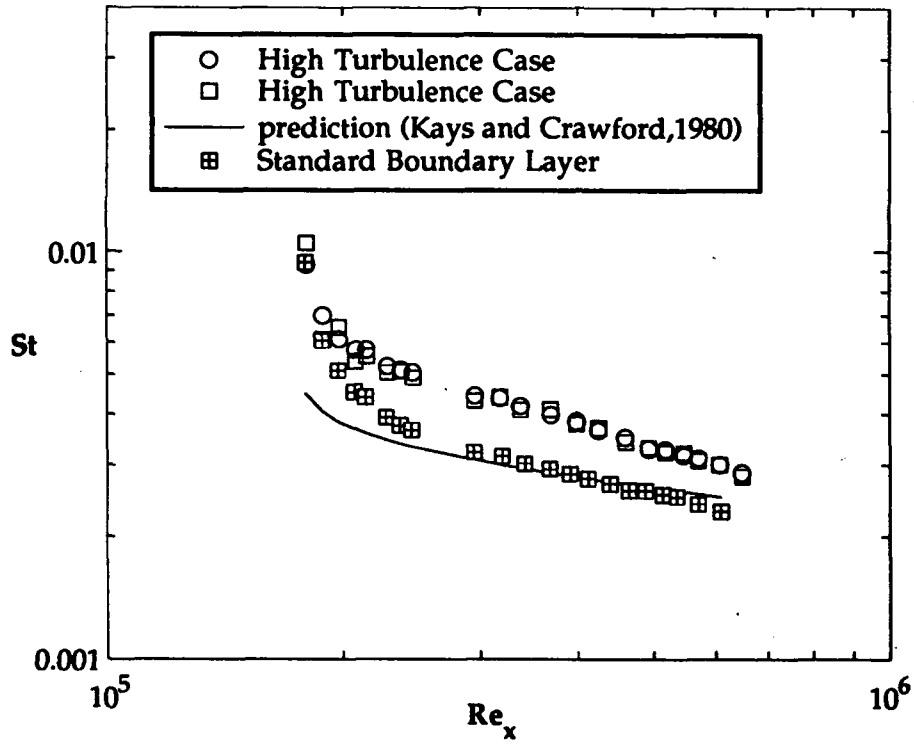


Figure 6.1 Stanton number distribution for both the standard boundary layer and high freestream turbulence case.

were measured varied from $Tu = 24\%$ at the start of the heat flux surface to $Tu = 11\%$ at downstream station where $Re_x = 6.5 \times 10^5$.

Correlation of this heat transfer data requires measurements of the enthalpy thickness at various streamwise positions. As discussed in Section 2.3 the enthalpy thickness, Δ , can be determined directly by measuring the velocity and temperature profiles, or it can be found by using an energy balance which results in $\Delta = St \cdot x_h$, where x_h is the distance along the heater plate. For the standard boundary layer, this energy balance was within 6%. For the high freestream turbulence heat transfer data, the enthalpy thickness was obtained using $\Delta = St \cdot x_h$.

Results presented in Figure 6.1 were obtained at nominal freestream velocities of 7.8 m/s for both the standard boundary layer and the boundary layer with high freestream turbulence. As noted in Section 2.3, good agreement was found between the measured St and established correlations. Experimentally measured values of St for the standard boundary layer were used as the reference St_0 in evaluating freestream turbulence effects.

Although we were most interested in how increases in St would correlate with various parameters which accounted for turbulence levels and length scales, the increase in St simply as a function of position (x_h) is quite informative. As shown in Figure 6.2, the enhancement of heat transfer increases dramatically at the start of the heat flux surface reaching a maximum of $St/St_0 = 1.4$ within a short distance. The results of Ames and Moffat (1990a), also shown on Figure 6.2, also showed an increase in St/St_0 at the start of the heat flux plate. Since heat transfer is expected to increase proportional to freestream turbulence level, and since the freestream turbulence level decreases with downstream position, the increase in St/St_0 with downstream position at the start of the heat flux plate is contrary to expectations. This reduced enhancement of heat transfer due to high freestream turbulence could be due to either a low Re_Δ effect or a large ratio of turbulence length scale to thermal boundary layer thickness, Λ_x/Δ . In both data sets the enhancement increases in the downstream direction until there is a peak in the enhancement. If we assume that the suppression of the heat transfer has become negligible at this peak, it is of interest to contrast Re_Δ and

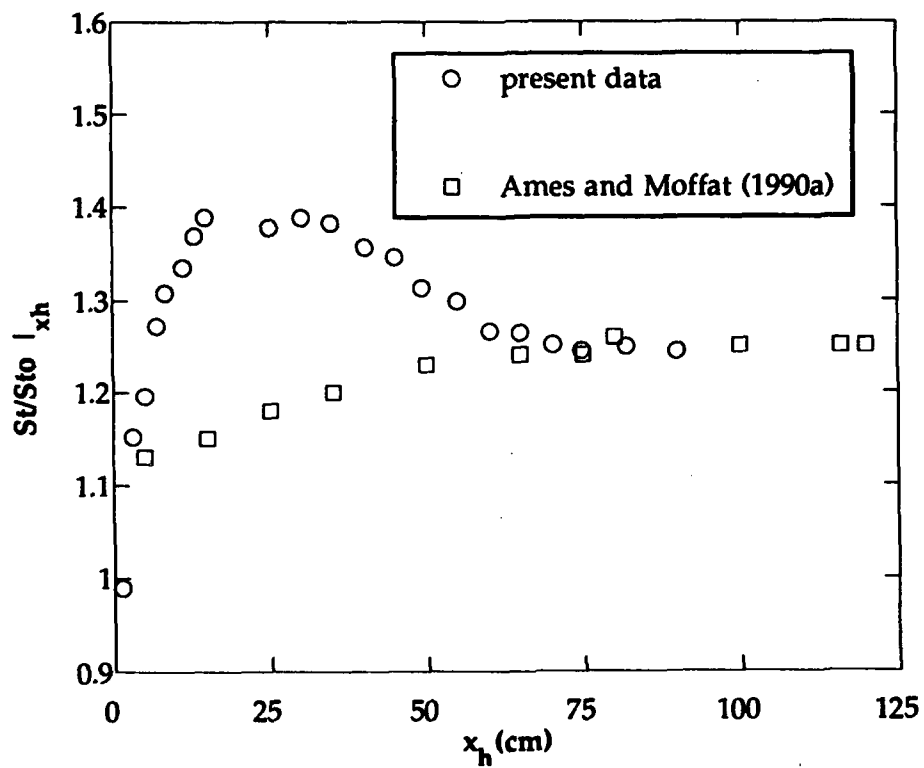


Figure 6.2 Ratio of high freestream turbulence St to the standard boundary layer St_0 at the same streamwise locations.

Λ_x/Δ for the two data sets at the peak. These values are $Re_\Delta = 520$ and 1960 , and $\Lambda_x/\Delta = 29$ and 36 for our data and for that of Ames and Moffat, respectively. Clearly, the Re_Δ values are quite different, but the Λ_x/Δ are very close, suggesting that the suppression of the heat transfer enhancement at the beginning of the plate is due to a length scale ratio effect.

Four correlations for scaling the enhancement of heat transfer due to high freestream turbulence were evaluated. The first correlation was that developed by Hancock and Bradshaw (1983) for correlating the effect of high freestream turbulence on skin friction. They found that the skin friction coefficient ratio (C_f/C_{f0}), where C_{f0} is for a standard boundary layer at the same Re_θ , correlated with a parameter they defined as:

$$HB \equiv \frac{Tu}{\left(\frac{L_u^\varepsilon}{\delta_{99}} + 2\right)} \quad (6.1)$$

where the dissipation length scale (L_u^ε) was defined by Simonich and Bradshaw (1978) as:

$$L_u^\varepsilon \equiv - \frac{\overline{(u'^2)^2}}{U_\infty \frac{d\overline{(u'^2)^2}}{dx}} \quad (6.2)$$

Blair (1983) adjusted the Hancock/Bradshaw correlation for heat transfer by using a Reynolds analogy factor, $2St/C_f = 1.3$. Data from our experiments and the experiments of Ames and Moffat (1990a) are compared with the Hancock/Bradshaw correlation and the Blair modification in Figure 6.3. Although the data of Ames and Moffat are in reasonable agreement with the Hancock/Bradshaw correlation, our data show as much as a factor of 2 greater increase in St .

Blair also suggested a correction for reduced enhancement of heat transfer which occurs at low Reynolds number. When applied to our data this low Reynolds number correction led to greater disagreement between our results and the Hancock/Bradshaw correlation.

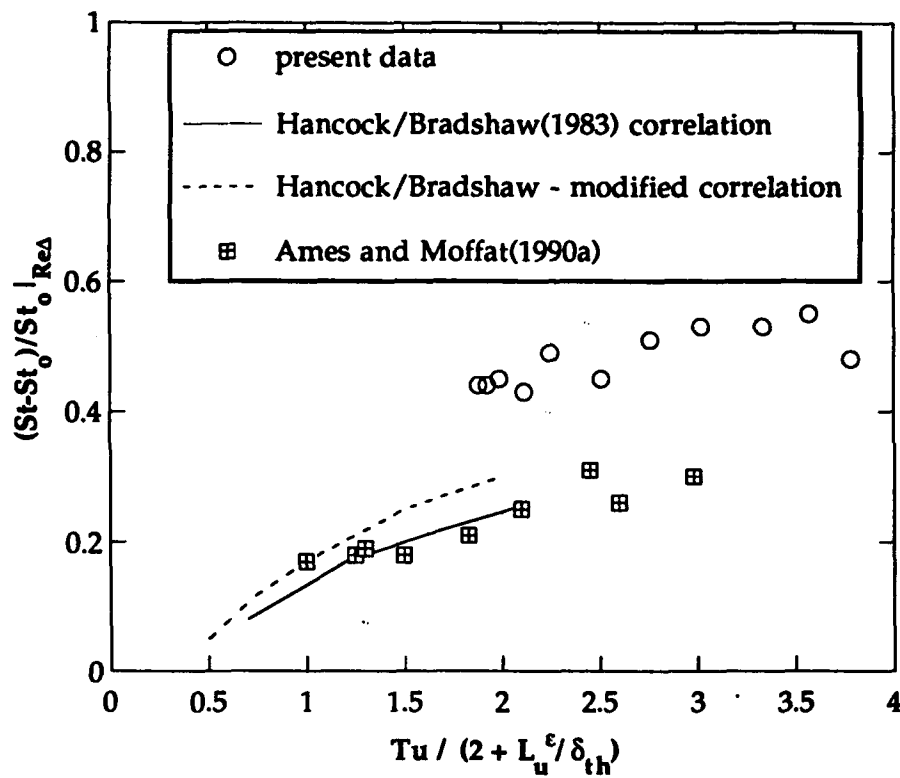


Figure 6.3 Comparison of present data with the Hancock/Bradshaw (1983) correlation.

A correlation for high freestream turbulence effects on heat transfer was proposed by Maciejewski and Moffat (1989) in which the Stanton number was based on the maximum fluctuating streamwise velocity rather than the mean velocity. Results using this St' correlation are shown in Figure 6.4. Our present data, the data of Maciejewski and Moffat, the data of Ames and Moffat (1990a), and the data of MacArthur, et al. (1986) show a relatively constant value of St' within the range $0.020 < St' < 0.028$. The correlation proposed by Maciejewski and Moffat with a large peak at $Tu = 11\%$ was developed before the present data and the data of Ames and Moffat were available. The experimental results shown in Figure 6.4 indicate that a better correlation of the data would be achieved for a constant value of $St' = 0.022$.

The third correlation evaluated was proposed by Ames and Moffat (1990b) who used scaling arguments to deduce the effect of high freestream turbulence on turbulent heat transport and defined a scaling parameter, TLR, as follows:

$$TLR \equiv Tu \left(\frac{\Delta}{L_\epsilon} \right)^{0.33} \left(\frac{Re_\Delta}{1000} \right)^{0.25} \quad (6.3)$$

Our data and that of Ames and Moffat (1990b) are presented in terms of the TLR parameter in Figure 6.5. There is a distinct overlap of the data at $TLR \approx 0.04$ where the present results are distinctly higher than the data of Ames and Moffat. A similar parameter, TAR, can be defined by substituting the integral length scale for the dissipation scale in equation 6.3. When scaled with respect to this TAR parameter a consistent trend was found for the data of Ames and Moffat (1990b), Maciejewski and Moffat (1989), and the present results as shown in Figure 6.6. The improved correlation with respect to the TAR parameter may be attributed to the integral scale being a direct measure of the characteristic length scale of the turbulence. The legitimacy of using a the dissipation scale is particularly questionable in flows that are not truly homogeneous and isotropic. Highly turbulent flow fields are quite often neither homogeneous nor isotropic.

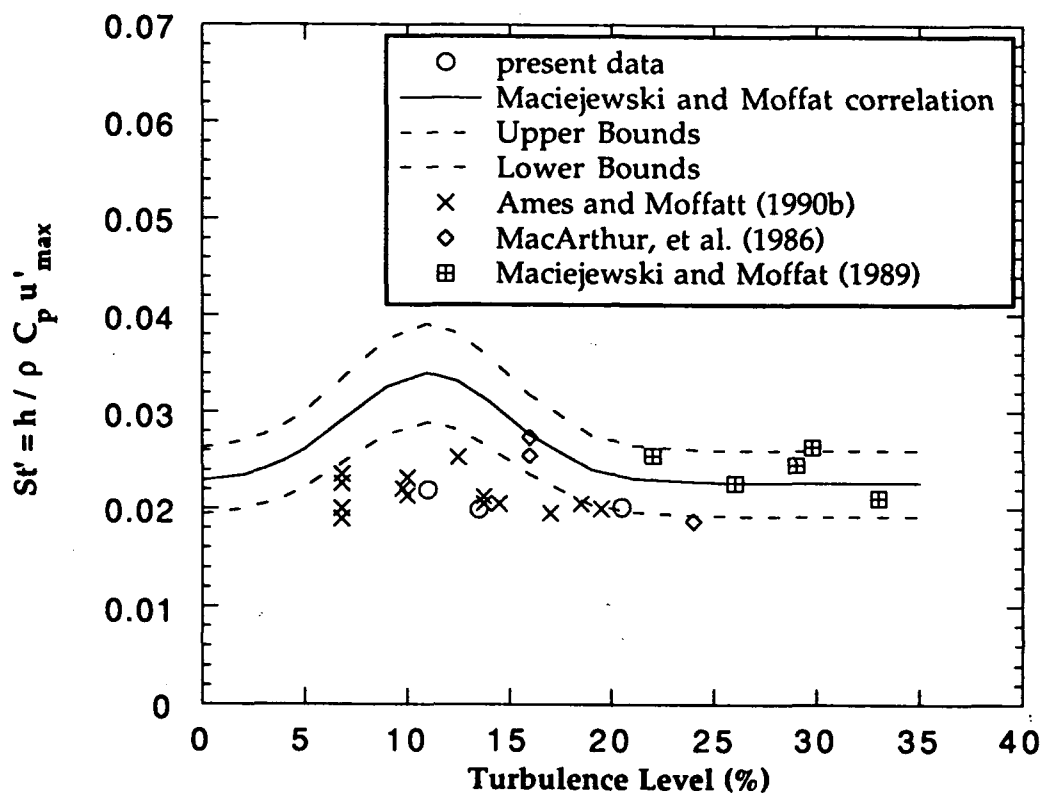


Figure 6.4 Comparison of present data with the Maciejewski and Moffat (1989) correlation.

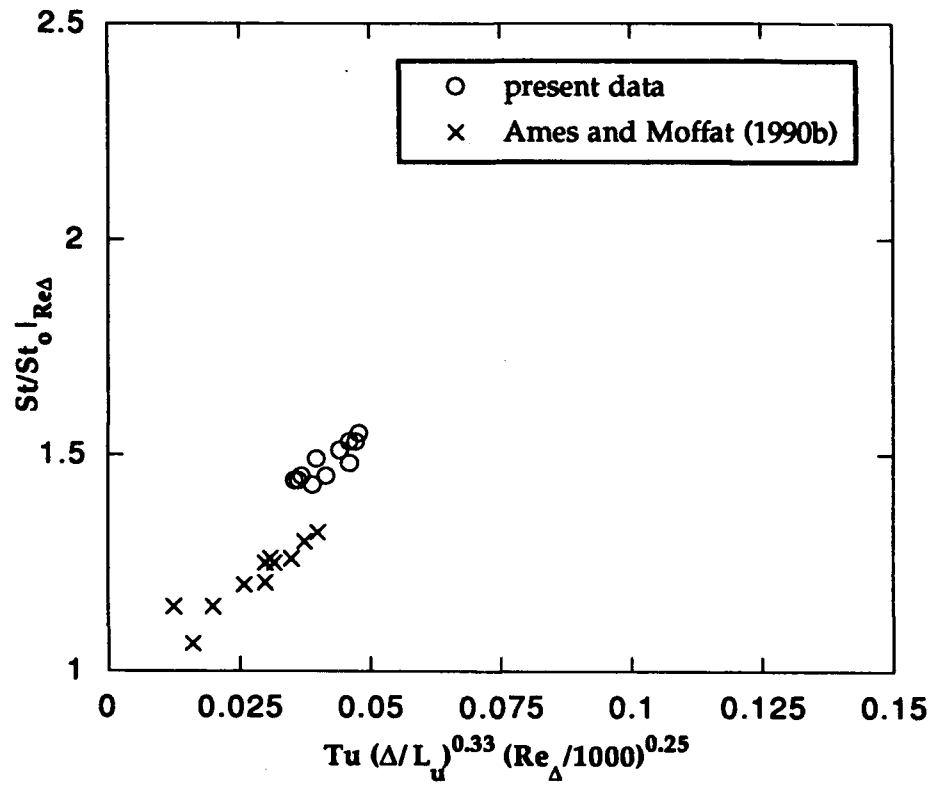


Figure 6.5 Comparison of present data to the Ames and Moffat (1990b) correlation using the turbulent dissipation scale.

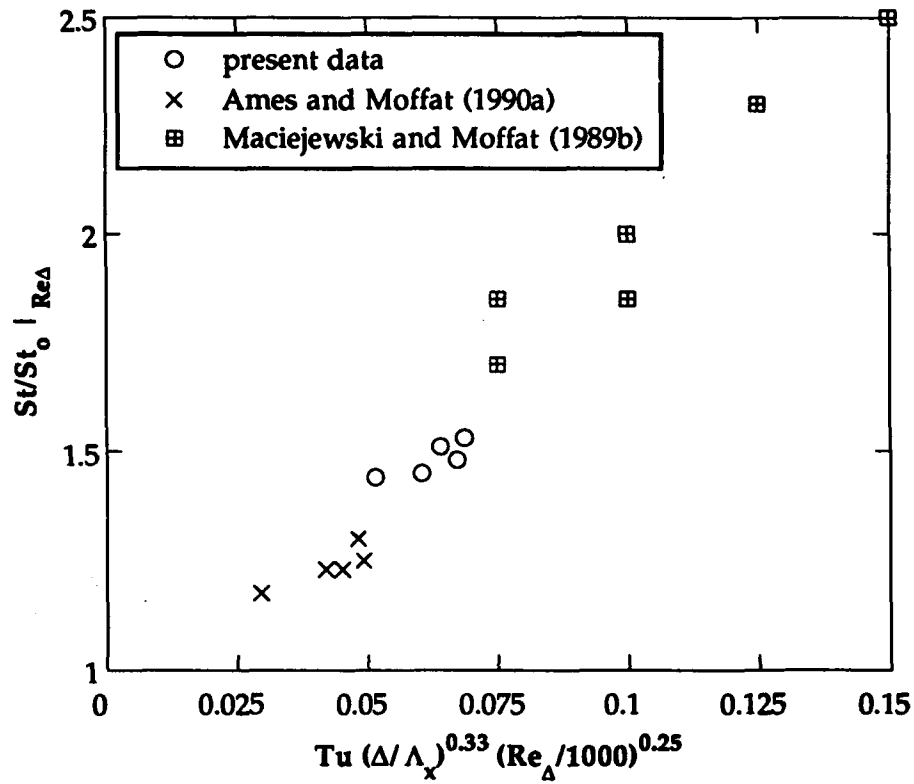


Figure 6.6 Comparison of present data to the Ames and Moffat (1990b) correlation using the turbulent integral scale.

6.2 Velocity Field

Data presented in this section are nondimensionalized using the shear velocity, u_τ , obtained from Clauser fits to the log-law region of the mean velocity profile. Use of the Clauser fit technique, which has typically been done in previous studies of high freestream turbulence effects on turbulent boundary layers, presumes that the log-law is still valid. However, results that we present in this section show that the validity of the log-law is questionable at very high freestream turbulence levels. Hence, in using the Clauser fit u_τ , we realize that the presentation of the data at very high turbulence levels is flawed, but the presentation still illustrates inadequacy of the log-law at very high freestream turbulence levels.

Figure 6.7 shows the mean velocity profiles curve fit to the log-law for freestream turbulence levels of $Tu = 20.5\%$ ($Re_\theta = 710$), 13% ($Re_\theta = 780$), and 11% ($Re_\theta = 1050$) as compared to a standard boundary layer. At these high turbulence levels it is clear that not only has the wake in the outer part of the boundary layer been reduced, but also a significant negative wake occurs. Moreover, the point at which the mean profile deviates from the log-law occurs at smaller y^+ as the turbulence level increases. In particular, the mean velocity profile for $Tu = 20.5\%$ deviates from the log-law almost immediately at $y^+ = 50$ and has a slope that is distinctly less than that for the log-law.

The deviation of the mean velocity profile from the log-law at smaller y^+ as the freestream turbulence level increases is consistent with the data presented by Ames and Moffat (1990b). Also, similar to Ames and Moffat, a greater enhancement of heat transfer was found as compared to the skin friction which was deduced from the best fit to the log-law.

Profiles for the streamwise and vertical rms fluctuating velocities, nondimensionalized with shear velocity, u_τ , are shown in Figures 6.8a and 6.8b, respectively. In these figures the present data at turbulence levels of 20.5% , 13% , and 11% are supplemented with data from Johnson and Johnston (1989) for turbulence levels of 7.5% ($Re_\theta = 1230$) and 0% ($Re_\theta = 1460$). These figures show quite clearly that the rms fluctuating velocities are scaled with

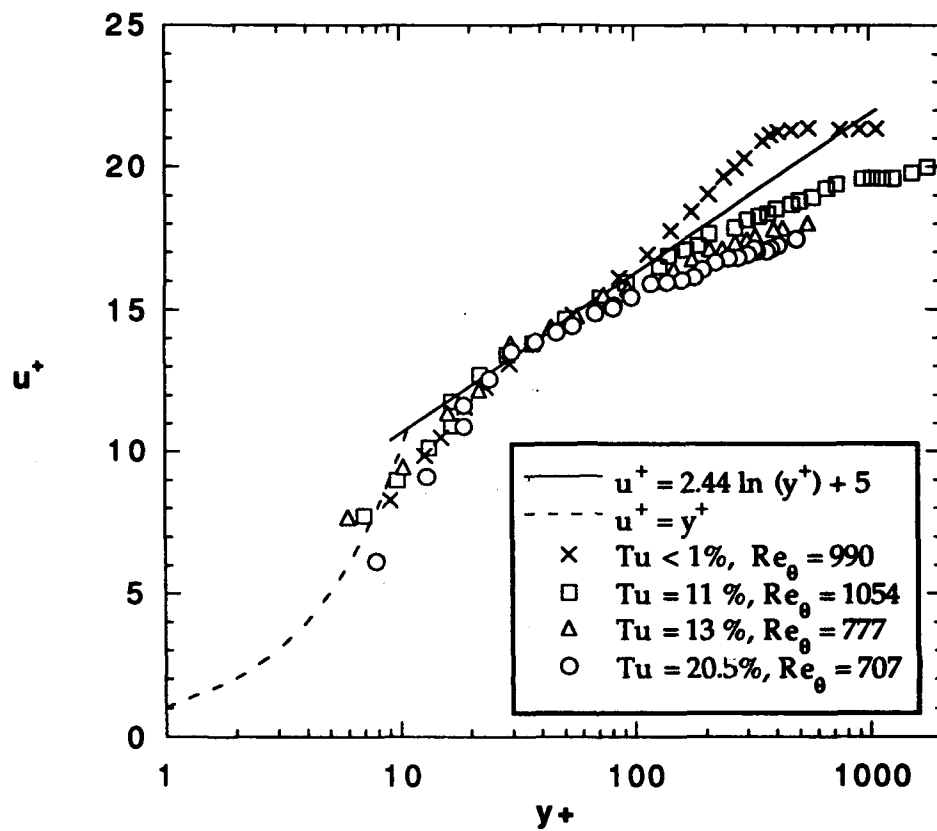


Figure 6.7 Mean velocity profiles in terms of inner wall variables at three different turbulence levels.

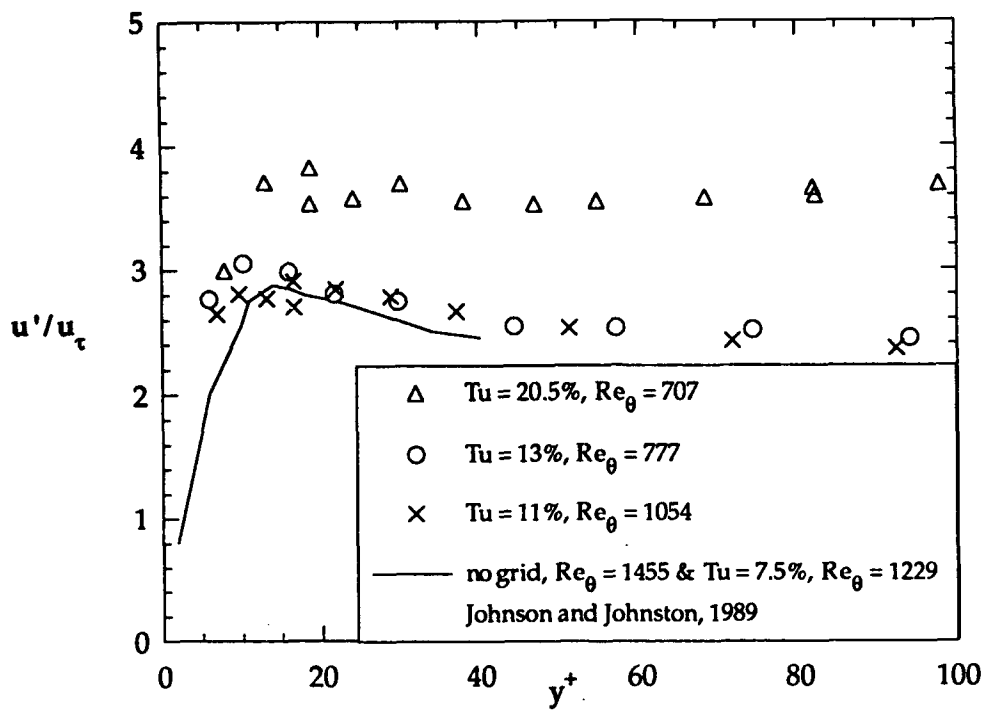


Figure 6.8a. Profile of rms fluctuating streamwise velocities nondimensionalized with inner wall coordinates.

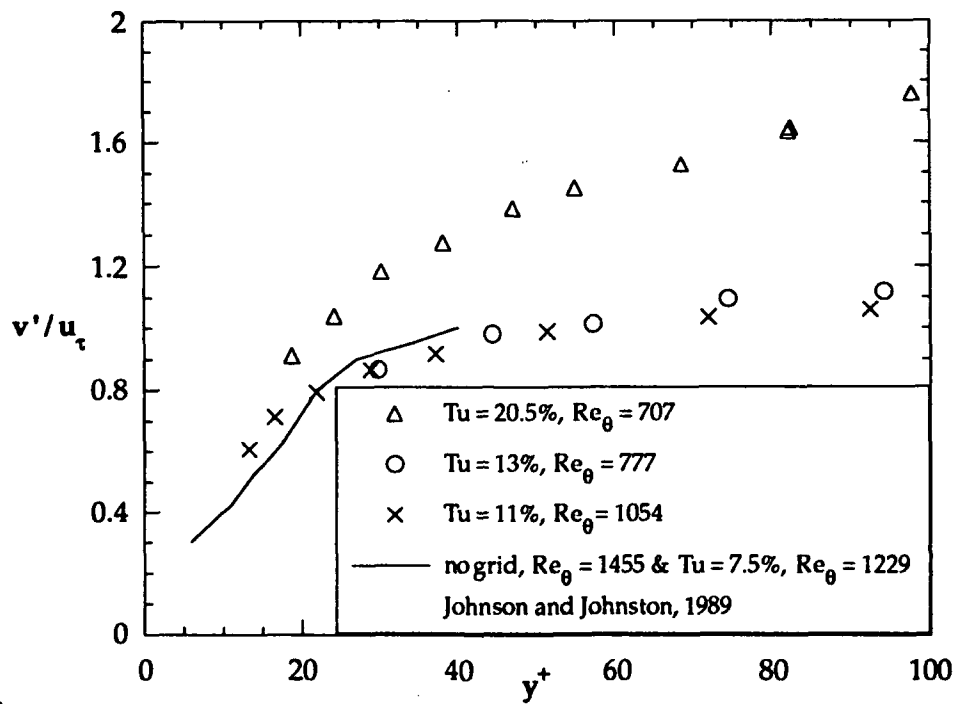


Figure 6.8b Profile of rms fluctuating vertical velocities nondimensionalized with inner wall coordinates.

u_τ quite successfully for freestream turbulence levels less than 13%, but both the u'/u_τ and v'/u_τ profiles are significantly increased for a freestream turbulence level of 20.5%. Ames and Moffat (1990b) observed a similar increase in u'/u_τ for freestream turbulence levels of 15% and 19%. Given that the fluctuating velocities no longer scale with the shear velocity u_τ for high freestream turbulence levels, the validity of the log-law for the mean velocity field is questionable at these high freestream turbulence levels.

The propagation of freestream turbulence effects into the boundary layer is particularly evident from the correlation coefficient R_{uv} . The effect of increasing freestream turbulence levels on R_{uv} is shown Figure 6.9. For low freestream turbulence (nominally $Tu = 1\%$) $R_{uv} \approx -0.45$ which is consistent with many previous studies. For a freestream turbulence level of 11%, the correlation coefficient is significantly smaller in magnitude at the outer part of the boundary layer, but rises to essentially the low turbulence value close to the wall. However, for a turbulence level of 20.5%, the magnitude of the correlation coefficient is significantly reduced all the way to the wall. These results indicate that the less coherent freestream turbulence propagates further into the boundary layer as freestream turbulence levels increase. For very high freestream turbulence levels, the effects propagate through to the wall.

Figure 6.10 compares shear stress distribution for a highly turbulent freestream with that of a low turbulence freestream. The shear stress is non-dimensionalized using the friction velocity, u_τ , which was obtained by doing a curve fit of the log-law. The nondimensional shear stress distribution for the highly turbulent case gives values greater than 1.0. This result suggests that the u_τ value obtained from a fit to the log-law is less than that which represents the true skin friction.

Previous studies have indicated that high freestream turbulence increases the wall heat flux more than the skin friction. For very high turbulence levels ($Tu > 10\%$) these results have been based on the use of curve fits to the log-law to deduce the skin friction. Our results have shown that the validity of the log-law for very high freestream turbulence levels is seriously in doubt. Consequently, determining the correlation between heat flux and skin

friction for very high freestream turbulence levels will require more precise measurements of the wall shear stress.

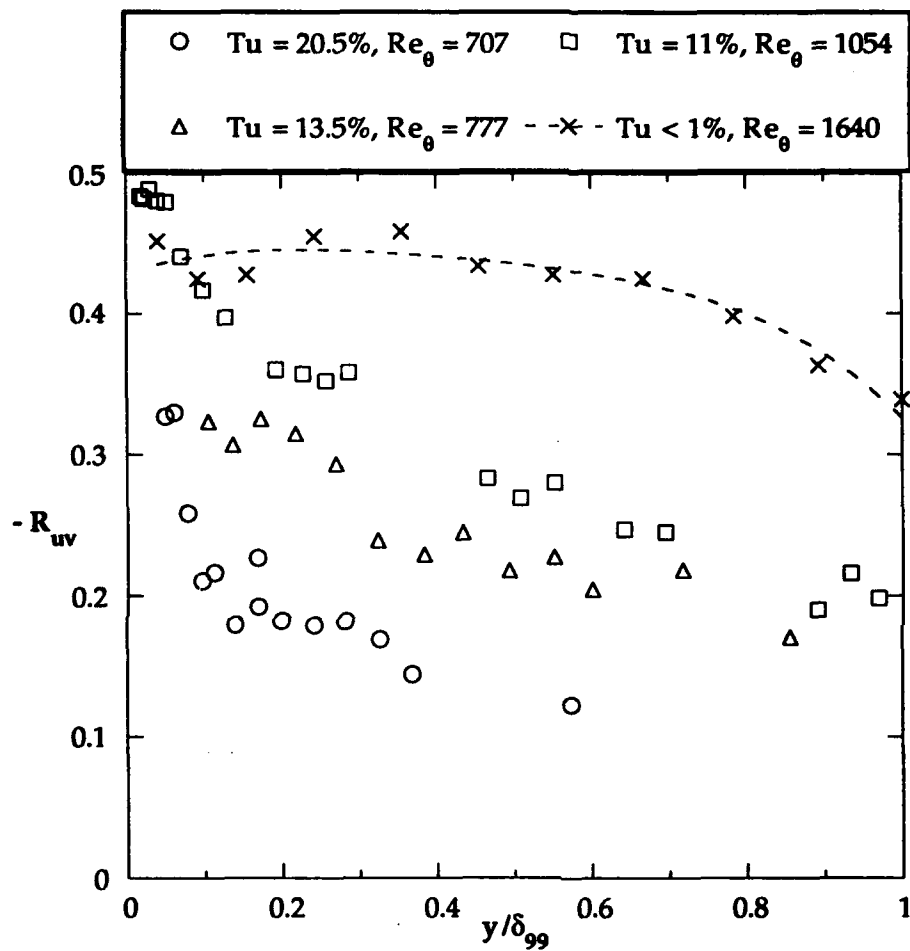


Figure 6.9 Correlation coefficient for a boundary layer influenced by high freestream turbulence.

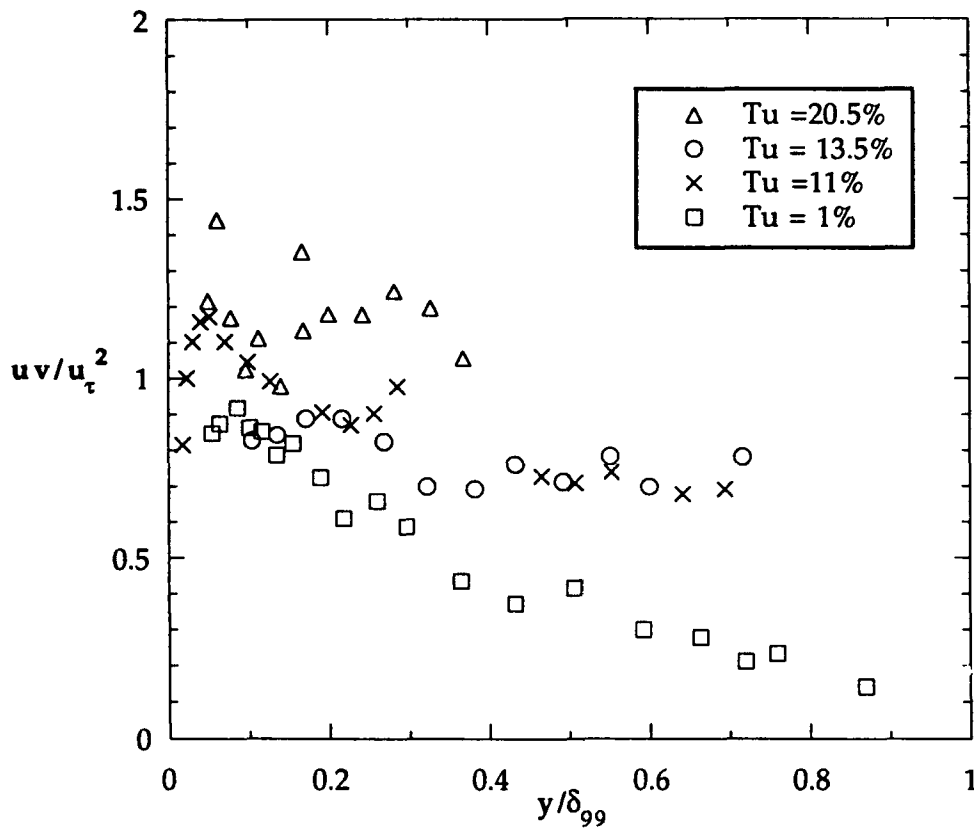


Figure 6.10 Comparison of nondimensionalized Reynolds shear stress with a standard boundary layer and boundary layer influenced by high freestream turbulence.

7. Conclusions and Recommendations

The turbulence generator we developed in this project produces freestream turbulence levels, Tu , in excess of $Tu = 20\%$; a turbulence level which is characteristic of that experienced in the turbine environment. These generated turbulence levels decayed from 20% to 11% over a streamwise distance of 65 cm with integral length scales on the order of the boundary layer thickness. This turbulence generator was incorporated in a new boundary layer wind tunnel facility which was designed specifically for testing adiabatic effectiveness and heat transfer coefficients for simulated film cooling flows. We also developed as part of this project a unique technique for simultaneous temperature and velocity measurement. This technique, based on simultaneous measurements from a submicron cold-wire and a laser Doppler velocimeter (LDV), requires no corrections for thermal lag of the temperature probe or thermal contamination of the velocity sensors. Consequently, the cold-wire/LDV technique is more accurate than any previously used technique or device.

Using the freestream turbulence generator in the boundary layer wind tunnel, effects on surface heat flux and the turbulence characteristics of the boundary layer were determined. Based on our results, and results in the literature, we determined the appropriate scaling of the heat transfer enhancement in terms freestream turbulence level and turbulence length scale.

From experimental measurements of the thermal field for simulated film cooling flows with variable density ratio, we determined conditions for which the cooling jets remained attached to the wall, detached and then reattached to the wall, or detached completely from the wall. Results from these experiments showed how the detachment/reattachment characteristics scale with the momentum flux ratio. These experiments were conducted with negligible freestream turbulence levels. Effects of high freestream turbulence on film cooling were not studied as originally planned due to the lengthy development phase of the turbulence generator and simultaneous temperature/velocity measurement technique. The next two sections will

discuss specific conclusions from this study and recommendations for future studies.

7.1 Specific Conclusions

These conclusions based on results obtained in this program are as follows:

1. The configuration of a row of high velocity jets in cross-flow proved to be effective in generating very high freestream turbulence levels. Jet-to-mainstream velocity ratios required to obtain turbulence levels above $Tu = 20\%$ ranged from jet-to-mainstream velocity ratio of $VR = 5$ in water flows to $VR = 10$ to 17 in air flows. For a given velocity ratio, turbulence levels increase with decreasing Reynolds number.
2. Accurate simultaneous measurements of temperature and velocity can be made when using a $0.64\text{-}\mu\text{m}$ cold-wire sensor located within 0.3 mm downstream of an LDV probe volume.
3. High freestream turbulence effects on surface heat flux were found to scale with both the St' and TAR parameters. St' is a special Stanton number based on the maximum rms velocity rather than the freestream mean velocity. The TAR parameter is based on scaling arguments for turbulent heat flux which includes length scale effects. The value of St' was found to be constant regardless of the turbulence level. Scaling with St' implies that the surface heat flux is dependent only on the magnitude of the fluctuating velocity, and independent of the mean velocity field and the turbulence length scale! In applying the TAR parameter, the enhancement of surface heat flux was quantified in terms of the ratio of Stanton numbers with and without high freestream turbulence, St/St_0 . The St/St_0 ratio was found to monotonically increase with an increase in the TAR parameter. The surface heat transfer enhancement was better characterized by integral length scales than by dissipation length scales.

4. For moderately high freestream turbulence levels ($Tu < 13\%$) the scaling of the mean velocity and Reynolds stress profiles is affected in the outer part of the boundary layer, but near wall profiles within the inner 10% of the boundary layer ($y/\delta < 0.1$) maintain scaling with inner variables of friction velocity and kinematic viscosity (u_τ and ν). However, our results show that for very high freestream turbulence levels ($Tu > 13\%$) the log-law mean velocity profile in the inner region of the boundary layer is no longer applicable.
5. Thermal field measurements of simulated film cooling jets showed that the detachment and reattachment characteristics of the jets scaled with the momentum flux ratio, I . Three regimes were identified: a low momentum flux regime, $I < 0.4$, in which the jets remain attached, an intermediate momentum flux regime, $0.4 < I < 0.8$, in which the jet initially detaches but reattaches to the wall, and a high momentum flux regime, $I > 0.8$, in which the jet detaches and remains detached from the wall.

7.2 Recommendations

The development of both the highly turbulent flowfield and the simultaneous velocity/temperature measurement technique was completed. Recommendations for future work include using this facility and this measurement technique to do further turbulent boundary layer studies. The recommendations in this section are primarily discussed in terms of how to further quantify the high freestream turbulence effects on a turbulent boundary layer subjected to a constant heat flux boundary condition. However, after the experiments described are completed for the turbulent boundary layer, the next step is to study the film cooled boundary layer.

One significant question is how the high freestream turbulence affects the thermal field for a turbulent boundary layer. Both mean and fluctuating temperature profiles need to be measured for the heated turbulent boundary layer subjected to high freestream turbulence in order to answer this question.

The velocity/temperature measurements at high freestream turbulence levels should be documented. Simultaneous measurements are needed to determine how the correlations as well as the turbulent Prandtl number are affected at different turbulence levels. We have the capabilities of measuring space/time two-point correlations for temperature/velocity which would reveal the characteristics of the turbulent structure and how that structure is affected by high freestream turbulence. In order to get more detail on how the turbulent structures are altered, conditional sampling should be used employing either the temperature sensor or the LDV as a detector probe.

Lower velocity correlations in the boundary layer have been measured implying that less correlated freestream turbulence has penetrated into the boundary layer. How far the freestream turbulence penetrates and how it alters the boundary layer is useful for several reasons. Specifically, from a turbulence modeling viewpoint, if the modeling is based on a multiscale $k-\epsilon$ model where the kinetic energy is split into large and small scales, knowing how the freestream turbulence length scales alter the boundary layer length scales is required. Comparing the energy spectra between a standard boundary layer and a high freestream turbulence boundary layer at different boundary layer heights would allow us to determine both the penetration of the freestream turbulence, the magnitude of the alterations, and the energy partition.

From a heat transfer correlation standpoint, we need to further evaluate the St' and TAR correlating parameters. From our study, both parameters scaled high freestream turbulence effects on heat transfer. However, the St' parameter does not account for any type length scale directly, but the TAR parameter does. A series of experiments where the turbulence level is held constant but the turbulent length scales are altered over a large range, would resolve this issue. In addition, the St' model is based on the maximum u' velocity between $10 < y^+ < 25$, where y^+ is the vertical distance normalized by u_τ and ν . Therefore, in applying this model one must know beforehand what the maximum u' is for a given turbulence level. It would be valuable to determine how to predict u'_{\max} for a given turbulence level.

Appendix A

Mean Temperature Measurements of Jets in Crossflow for Gas Turbine Film Cooling Application

by

K. A. Thole, A. K. Sinha, D. G. Bogard, and M.E. Crawford

**Presented at the *Third International Symposium on Transport
Phenomena and Dynamics of Rotating Machinery*
Honolulu, Hawaii**

MEAN TEMPERATURE MEASUREMENTS OF JETS WITH A CROSSFLOW FOR GAS TURBINE FILM COOLING APPLICATION

K. A. Thole, A. K. Sinha, D. G. Bogard, and M. E. Crawford

Mechanical Engineering Department, University of Texas, Austin, TX 78712 USA

ABSTRACT

This paper presents mean temperature profiles measured within and downstream of a row of inclined jets with a crossflow. The conditions for the experiments are representative of film cooling used on gas turbine blades. A range of density ratio between 1.2 and 2.0 was examined under different mass, velocity, and momentum flux ratios of the jet to mainstream. Of these film cooling parameters, the momentum flux ratio best scaled the characteristics of the thermal field. The film cooling jets were found to remain attached to the surface; to detach and then reattach to the surface; or to detach and remain detached from the surface. These three scenarios and also the vertical jet penetration distance into the mainstream were found to scale with the momentum flux ratio. These results which establish the point at which detachment occurs have obvious relevance to turbine blade film cooling. The velocity ratio and mass flux ratios were found to be inadequate scaling parameters for the thermal fields.

NOMENCLATURE

D	injection hole diameter
DR	density ratio, jet to mainstream, $DR = \rho_j/\rho_\infty$
I	momentum flux ratio, jet-to-freestream, $I = \rho_j U_j^2 / \rho_\infty U_\infty^2$
k	thermal conductivity
M	mass flux ratio or blowing rate, jet to freestream, $M = \rho_j U_j / \rho_\infty U_\infty$
Re_{δ_2}	Reynolds number based on momentum thickness, $Re_{\delta_2} = U_\infty \delta_2 / \nu$
T	mean temperature
T_{aw}	adiabatic surface temperature
T_j	temperature of the injected fluid
T_∞	freestream temperature
U_j	average jet velocity at the exit of the hole
U_∞	freestream velocity
VR	velocity ratio, average jet velocity to mainstream, $VR = U_j/U_\infty$
X	downstream distance from the leading edge of the hole
Y	vertical distance measured from the test surface
Z	lateral distance measured from the axis of the hole
α	coefficient of thermal expansion
ρ	density
θ	non-dimensional temperature, $\theta = (T - T_\infty)/(T_j - T_\infty)$
η	adiabatic wall effectiveness $\eta = (T_{aw} - T_\infty)/(T_j - T_\infty)$
δ_1	boundary layer displacement thickness

δ_{99}	boundary layer thickness
δ_2	boundary layer momentum thickness
ν	kinematic viscosity

INTRODUCTION

Because designers are increasing the entry temperatures to turbines to improve propulsion efficiencies, new cooling schemes for the turbine blade are required to prolong the blade's life. *Film cooling is a turbine cooling technique in which the blade surface is protected from high temperature mainstream gases by releasing a coolant through the surface.* In the blade (or vane) cooling process, the compressor bleed air is introduced into the hollow core of the blade and is channeled and then dumped through the blade surface via one or more rows of holes. The holes are typically located in the vicinity of the leading edge of the blade and at other high thermally loaded locations on the blade's suction and pressure surfaces. The heat transfer process is an external convection/conduction/internal convection process in which the resulting external and internal heat fluxes set the blade temperature. The coolant is intended to help reduce the external heat flux to the blade.

Cooling jets emerging at various locations along the surface interact with the boundary layer flow along the surface and the hot mainstream. Governing the flow field of the jet-mainstream interaction and the associated heat transfer are geometrical parameters such as hole shape, angle, and spacing; and fluid dynamic parameters such as coolant-to-mainstream ratios of density (DR), velocity (VR), blowing or mass flux (M), and momentum flux (I). Most previous research has focused on how these parameters influence the wall temperature for an adiabatic wall. These results are generally presented in terms of a normalized wall temperature which is known as the adiabatic wall effectiveness, η . Relatively few studies have investigated the thermal and flow fields associated with the film cooling.

The adiabatic wall effectiveness is primarily dependent on how the cooling jet interacts with the mainstream. The thermal field is important because it directly shows the jet-mainstream interaction. For example, Ramsey and Goldstein (1971) used temperature profiles, measured at a sequence of four streamwise locations, to track the "penetration of the jet" at two different blowing ratios. In a later study, Yoshida and Goldstein (1984) used temperature profile measurements to distinguish differences in jet trajectories and mixing with the mainstream when the jet and mainstream conditions changed from laminar to turbulent.

Several studies have been conducted in which a heavy molecular weight gas is used to obtain higher density for the cooling jets. The technique relies on the use of the heat-mass transfer analogy to relate the measured species concentration field to the thermal field. This analogy holds if the turbulent and molecular Lewis numbers are unity, as noted by Ito et. al. (1978). Similar to the thermal profile measurements, concentration profile measurements have been used to determine the penetration of the cooling jets into the mainstream. In particular, Foster and Lampard (1980) used measurements of concentration profiles at a sequence of four streamwise locations to establish "jet lift-off." They noted that this jet lift-off was not clearly evident from mean velocity profiles measured at the same streamwise locations. Ko et. al. (1982) also established jet lift-off using a concentration profile measured a short distance downstream of the hole.

The importance of the thermal field is indicated by the computational study of Demuren et. al. (1985) in which discrepancies between computed and measured cooling effectiveness were resolved by referring to computed and measured temperature fields. Differences between predicted and measured cooling effectivenesses were found to be due to distinct differences in the computed and measured temperature fields in the near wall region, although the overall

temperature fields were qualitatively the same.

Although thermal or concentration field measurements are clearly superior for determining the trajectory of the cooling jets, previous studies have not established the effect of parameter variations. In particular, the thermal field with respect to mass flux, velocity, or momentum flux ratios has not been evident in previous studies because of the limited range of parameter variations – one or two blowing ratios at a constant density ratio.

Since the density ratio is generally about $DR = 2$ for gas turbine film cooling, the effect of high density ratios is important. Moreover, varying the density ratio over a wide range is the only way to independently vary the key flow parameters M , VR , and I . The only previous work in which systematic variations of density ratio were used to determine appropriate scaling parameters for film cooling were studies by Pederson, Eckert, and Goldstein (1977) and Sinha, Bogard, and Crawford (1990). Using a foreign gas injectant, Pederson et al. varied the density ratio from 0.2 to 4 with a range of blowing ratios and measured the effects on η . Along the centerline at a position $X/D = 10$ downstream of the hole, they found that the maximum η always occurred at approximately $VR = 0.5$ with increasing η at higher density ratios. For $VR > 0.8$, η at different density ratios scaled with velocity ratio, but for $VR < 0.4$, η was found to scale with momentum flux ratio. Sinha et al. (1990) used thermal techniques to determine adiabatic effectiveness for density ratios ranging from 1.2 to 2.0. Their results showed that the centerline effectiveness scaled with mass flux ratio while the jet remained attached to the wall, but scaled best with momentum flux ratio when the jet began to detach.

Pietrzyk, Bogard, and Crawford (1989b) presented detailed velocity data for density ratios of $DR = 1$ and $DR = 2$ with a range of blowing ratios. In the near hole region the velocity ratio was found to be a good parameter for scaling density effects. In the far-field region, the velocity fields for the dense jets were similar to that for the unit density case with the same mass flux ratio. The high density jets had significantly lower relaxation rates for the turbulence levels and \overline{uv} shear stresses as compared with the low density jets.

In this study, measurements of the thermal field were made to complement previous measurements of the velocity field of Pietrzyk et al. (1989a and 1989b). The thermal field shows certain characteristics that the velocity field cannot show. The thermal field measurements also give a better indication of the jet trajectory and jet lift-off as compared to velocity field measurements. The thermal field measurements combined with previous velocity field measurements provide an important database for developing and verifying film cooling models. The experimental conditions for this study were achieved by cryogenically cooling the injectant to vary the density ratio while independently varying the mass flux, the momentum flux, and the velocity ratios. A major goal of this study was to determine how each of these parameters scaled the entire thermal field as the density ratio varied. Previously reported studies of the thermal field (concentration field) have not been extensive enough to show variation in the jet trajectory and diffusion as M , VR , and I are varied.

FACILITY AND INSTRUMENTATION

Experiments were performed using a closed loop wind tunnel with a secondary flow loop that provided cryogenically cooled air for controlling the jet density, as depicted in Fig. 1. A flat test plate was used with a single row of inclined holes. A brief description of the facility is given here; but further details can be found in Pietrzyk, Bogard, and Crawford (1989a and 1989b).

Figure 2 shows the geometry of the film-cooled test plate and the coordinate system. The

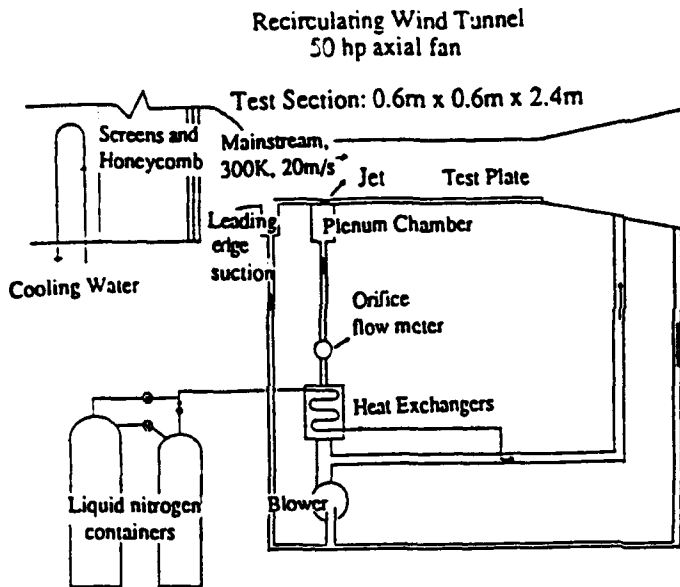


FIGURE 1. Schematic of the the film cooling test facility.

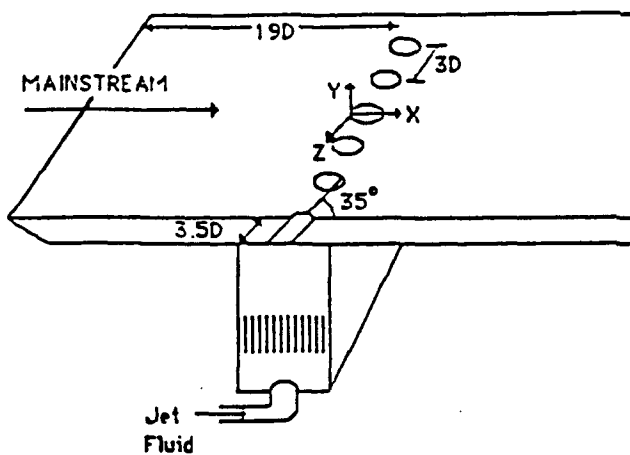


FIGURE 2. Film cooling test geometry and coordinate system.

cryogenically cooled air was injected through a row of 11 holes, 12.7 mm in diameter and spaced 3 diameters apart in the spanwise direction. The holes, having a length-to-diameter ratio of 3.5, were inclined at 35 degrees and located 19 diameters downstream of the leading edge of the test plate. The test plate and plenum chamber were constructed from a glass

reinforced plastic material (commercially known as EXTREN) with low thermal expansion coefficient ($\alpha = 1.4 \times 10^{-5}$ per K) and relatively low thermal conductivity ($k = 0.58$ W/m/K). Surface roughness measurements verified that the plate was hydrodynamically smooth.

Initial Boundary Layer Conditions

A 50 hp axial fan located in the closed loop recirculating wind tunnel provided the mainstream flow. Suction was used to remove the boundary layer upstream of the test section, and a new boundary layer was initiated at the sharp leading edge of the test plate that formed the test section floor. The suction rate was set based on measurements of the pressure differential across the leading edge of the plate. Laser Doppler velocimetry measurements showed that this ensured parallel flow above the leading edge. A heat exchanger, located between the blower and the wind tunnel contraction, maintained the freestream temperature at $298 \text{ K} \pm 0.5 \text{ K}$. For all experiments the freestream velocity was $20 \text{ m/s} \pm 1 \%$ and the freestream turbulence intensity was 0.2% . The freestream velocity was uniform within $\pm 0.5 \%$ in both the spanwise and streamwise directions. The streamwise development of the turbulent boundary layer on the test plate was documented by Pietrzyk et al. (1989a), who showed that at the injection location ($X/D = 0$), the non-dimensional boundary layer thickness δ_{99}/D was $\delta_{99}/D = 0.58$, the non-dimensional boundary layer displacement thickness was $\delta_1/D = 0.10$, and the momentum-thickness Reynolds number was about $Re_{\delta_2} = 1090$.

A thin, uniform thermal boundary layer in the spanwise direction was formed due to the cold plenum chamber which extended from $X/D = -5$ to $X/D = 3$ below the test plate. The maximum normalized temperature, measured in the thermal boundary layer between holes at $X/D = 3$ and at $Y/D = 0.08$ above the wall, was less than $\theta = 0.05$, which was below the lowest temperature contour appearing on our plots. The approaching thermal boundary layer is insignificant when compared to the thermal boundary layer formed by the film cooling jets and thus not expected to alter the temperature field.

Conduction errors in the test plate were estimated using a three-dimensional conduction heat transfer code. Based on these calculations, the normalized surface temperatures were expected to be reduced by as much as $\Delta\eta = 0.3$ near the hole, and by $\Delta\eta = 0.1$ at $X/D = 10$. Despite these relatively large surface conduction errors, measurements showed that air temperatures were relatively unaffected as low as $Y/D = 0.01$.

Secondary Flow Loop

Cryogenically cooling the air in a secondary flow loop provided the injectant at a controllable density ratio. A 7.5 hp blower directed the air in the secondary flow loop through a set of four finned-tube heat exchangers arranged in series. Liquid nitrogen, supplied by a pressurized 160 liter dewar, was used as the coolant in the heat exchangers. The jet temperature was maintained within $\pm 1.5 \text{ K}$ of the required operating temperature.

The mass flowrate of the fluid in the secondary flow loop was measured using a sharp-edged orifice plate flow meter. To obtain accurate flowrate measurements, the air temperature was measured at the orifice meter. Temperatures in the secondary flow loop and the plenum supplying the jets of coolant were measured using chromel-constantan thermocouples. Accuracy of the thermocouples was verified using four set points provided by boiling distilled water (373.2 K), ice (273.2 K), dry ice (194.4 K), and liquid nitrogen (77.4 K).

The temperatures recorded by the readout instrument were within 0.1 K, which was the resolution of the instrument. Maximum temperature fluctuations at the orifice meter were ± 2.5 K, and the measurement of total mass flowrate of the jets was accurate within ± 0.7 %. Due to the accumulation of the frost in the secondary flow loop, the mass flowrate varied by as much as ± 4 % during experiments. The density ratio between the jets and the mainstream was maintained within ± 3 %. To check the variation in flowrate from different jets, the mean velocity was measured at five vertical positions at two streamwise locations for five different jets in the center of the test section. These measurements showed the variation of flowrate among the jets to be within ± 4 %. The temperature variation among the jets varied by less than ± 1 K.

Temperature Measurement Instrumentation

Air and wall temperatures were measured during the experiments. A TSI model 1050 hot-wire anemometer was operated in a constant current mode to obtain cold-wire measurements of the mean air temperature. A 4 micron diameter, tungsten wire with a sensor length of 0.76 mm was used. The cold-wire was calibrated in the mainstream and at the exit of the cooled jets where the air temperature was measured using thermocouples. The voltage/temperature correlation remained linear within 1.5% which was verified at jet temperatures of 247 K, 186 K, 166 K, and 150 K. The precision of traversing the temperature sensor was ± 0.01 mm normal to the wall and ± 0.5 mm in the streamwise direction. Taking into account the position uncertainty, the total uncertainty of the non-dimensional air temperatures (θ to be defined later) was ± 0.035 .

Chromel-constantan thermocouples measured the wall temperatures. Initial testing of an EXTREN plate showed that large conduction errors resulted from installing the lead wires to the thermocouples through the EXTREN plate. The primary source of the conduction errors was the large driving potential between the ambient and the cold surface, resulting in equilibrium temperatures of the bead that were significantly higher than that of the surface.

To eliminate the conduction error, ribbon contact surface thermocouples were developed. Sinha et. al. (1990) report the details of the surface temperature measuring technique. The ribbon thermocouples were nominally conduction-error free because of the large convective surface area relative to its small conduction cross-sectional area. The chromel and constantan ribbons were 1.5 mil thick and 60 mil wide with a junction diameter of approximately 15 mil. The thermocouples were joined by spot welding negative (constantan) ribbons to a single positive (chromel) ribbon. An epoxy bonded the thermocouples to the EXTREN plate. The non-dimensional surface temperatures were measured to within an accuracy of ± 0.006 .

EXPERIMENTAL PLAN

Since a constant mass flux ratio would maintain a constant energy flux ratio, one might expect the thermal field to scale with M as the density ratio changes. However, as discussed in the Introduction, Pietrzyk et. al. (1989b) found that the velocity field in the near hole region scaled with velocity ratio. With equal velocity ratios, the velocity gradients and the volumetric flowrates at different density ratios are similar. Pietrzyk et. al. (1989b) also noted that there appeared to be greater penetration for the higher density jet which had greater momentum flux ratio. Since the deflection of the jets leaving the hole depends on the momentum flux ratio, the momentum flux ratio should dictate the jet trajectory. Therefore, the thermal field, which is strongly dependent on the velocity field will be influenced by all three parameters, M , VR , and I . Consequently a series of experiments were designed to

systematically investigate the scaling of the thermal field with respect to M, VR, and I.

A list of the experimental conditions and the corresponding case and figure numbers of the data represented by temperature contours are presented in Table 1. Note that Cases 2, 3 and 4 were at constant velocity ratio, Cases 4, 7, and 8 were at constant mass flux ratio, and Cases 4, 5, and 6 were at constant momentum flux ratio.

TABLE 1. Range of Experimental Parameters

Case	Momentum Flux Ratio	Density Ratio	Velocity Ratio	Mass Flux Ratio	Figure Number
1	0.125	2.0	0.25	0.5	5
2	0.35	1.4	0.5	0.7	8
3	0.4	1.6	0.5	0.8	9
4	0.5	2.0	0.5	1.0	6
5	0.5	1.2	0.65	0.78	10
6	0.5	1.6	0.56	0.89	11
7	0.63	1.6	0.63	1.0	12
8	0.83	1.2	0.83	1.0	13
9	2.0	2.0	2.0	2.0	7

Mean temperature profiles were taken along the jet centerline ($Z/D = 0$) at a number of streamwise stations extending from the leading edge of the jet ($X/D \approx 0$) to 10 diameters downstream. The trailing edge of the hole extends to a streamwise location of $X/D = 1.74$. The gradients in the thermal field were effectively resolved by concentrating data points in regions of high gradients. The number of points in a profile varied depending on the streamwise location. Most of the figures presented in this paper to document the thermal fields are in form of contours, the levels of which were obtained by linearly interpolating between the data points. The data have been non-dimensionalized using the freestream and jet temperatures, and are presented in terms of a non-dimensional parameter, θ , defined by equation (1) as

$$\theta = \frac{T - T_{\infty}}{T_j - T_{\infty}} \quad (1)$$

RESULTS AND DISCUSSION

Whether or not a film cooling jet remains attached to the surface after it exits the hole is relevant to the protection the jet can give the turbine blade surface. If the jet remains attached, the coldest temperatures will occur at the blade surface to give the best possible protection. However, if the jet detaches from the surface immediately downstream of the hole, warmer temperatures occurring downstream of the jet exit would be detrimental to the blade.

Figure 3 shows the non-dimensional temperature profiles at three different streamwise locations for the lowest momentum flux ratio ($I = 0.125$) jet studied in these experiments. These profiles show the maximum θ occurs at the surface which indicates that at all three locations the film cooling jet remained attached to the surface. Also shown in Figure 3 are surface temperatures measured at $X/D = 6$ and 10 . The zero temperature gradients immediately above the wall show that the plate is essentially adiabatic in terms of heat flux into the air. However, there is a significant difference between the air temperature immediately above the plate and the surface temperature. This difference is due to conduction effects within the plate which were discussed in the Facilities and Instrumentation section.

Figure 4 shows non-dimensional temperature profiles at three streamwise locations for the full range of density ratios ($DR = 1.2, 1.6, \text{ and } 2$) at the same intermediate momentum flux ratio ($I = 0.5$). Even though these profiles were measured at significantly different density ratios, the profiles collapse to similar shapes. At this intermediate momentum flux ratio, the $X/D = 2$ profiles show steep gradients of θ at the surface. The steep gradients above the wall at $X/D = 2$ indicate either a conduction effect from the plate or a slightly detached jet with an influx of warm air under the jet. The thermal contours discussed below show that the shape of the profile at $X/D = 2$ can be attributed to detachment of the jet with an influx of warm under the jet, and not due to a conduction effect from the plate. At $X/D = 6$, it is difficult to determine whether the jet has reattached to the surface or is still detached, while at $X/D = 10$ the non-dimensional temperature profiles are similar to those of an attached jet.

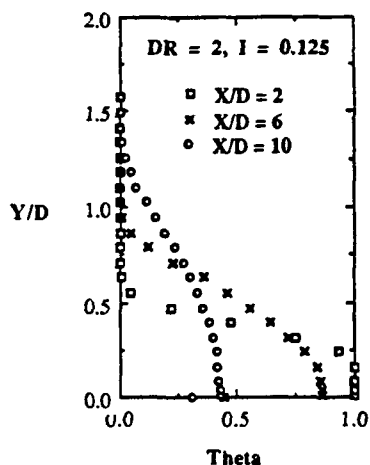


FIGURE 3. Dimensionless temperature profiles at three streamwise locations, $X/D = 2$, $X/D = 6$, and $X/D = 10$, for $I = 0.125$, $DR = 2$, $VR = 0.25$, $M = 0.5$.

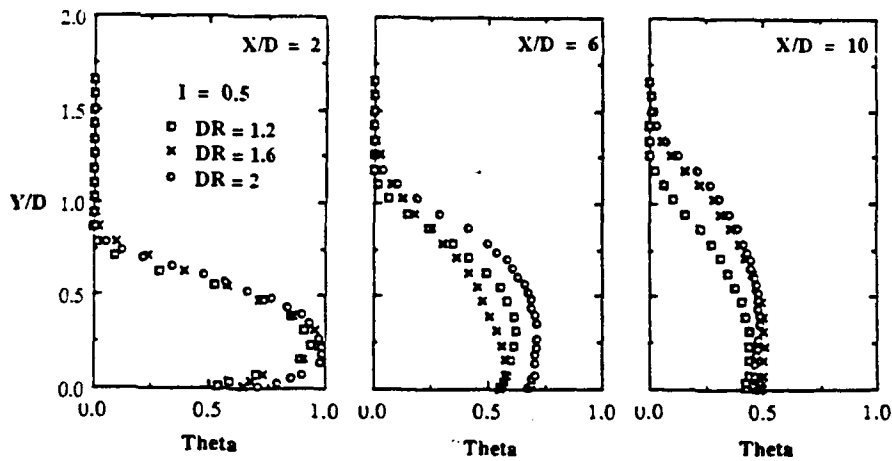


FIGURE 4. Dimensionless temperature profiles at three streamwise locations, $X/D = 2$, $X/D = 6$, and $X/D = 10$ for a constant momentum flux ratio ($I = 0.5$).

To determine whether the jet remains attached or detaches, contours of the complete thermal field were analyzed. Figures 5, 6, and 7 show the thermal fields for a series of experiments in which the density ratio was held constant at $DR = 2.0$ and the momentum flux ratio was varied such that the jet remains attached, detaches and then reattaches, and detaches and stays detached, respectively. Note that the θ contours in Figures 5 and 6 are for the same conditions as the θ profiles shown in Figures 3 and 4, respectively.

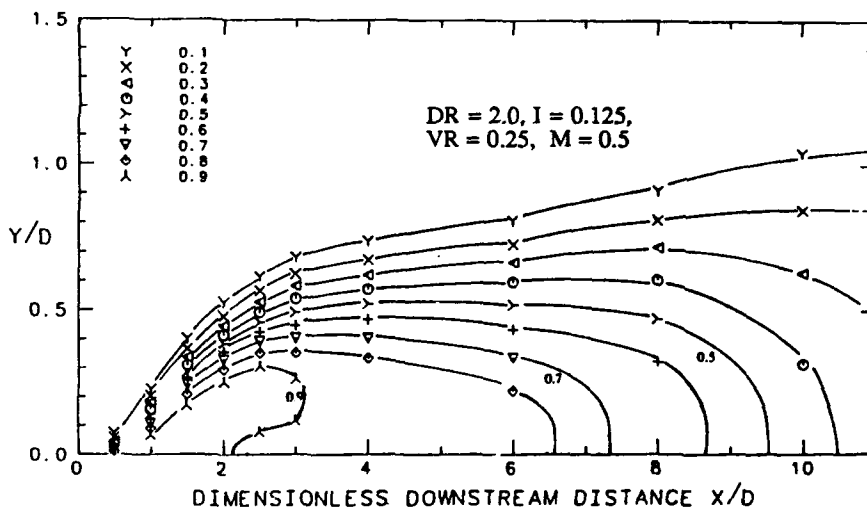


FIGURE 5. Dimensionless temperature contours along the jet centerline for $I = 0.125$, $DR = 2.0$, $VR = 0.25$, $M = 0.5$.

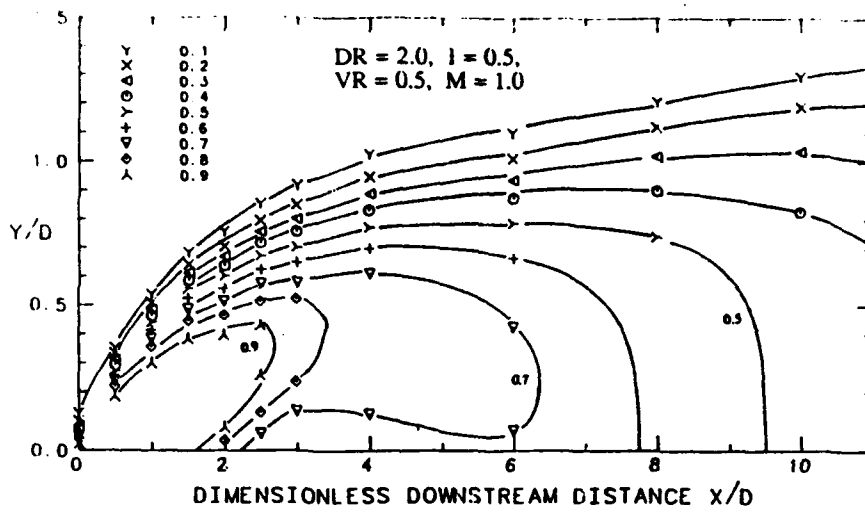


FIGURE 6. Dimensionless temperature contours along the jet centerline for $I = 0.5$, $DR = 2.0$, $VR = 0.50$, $M = 1.0$.

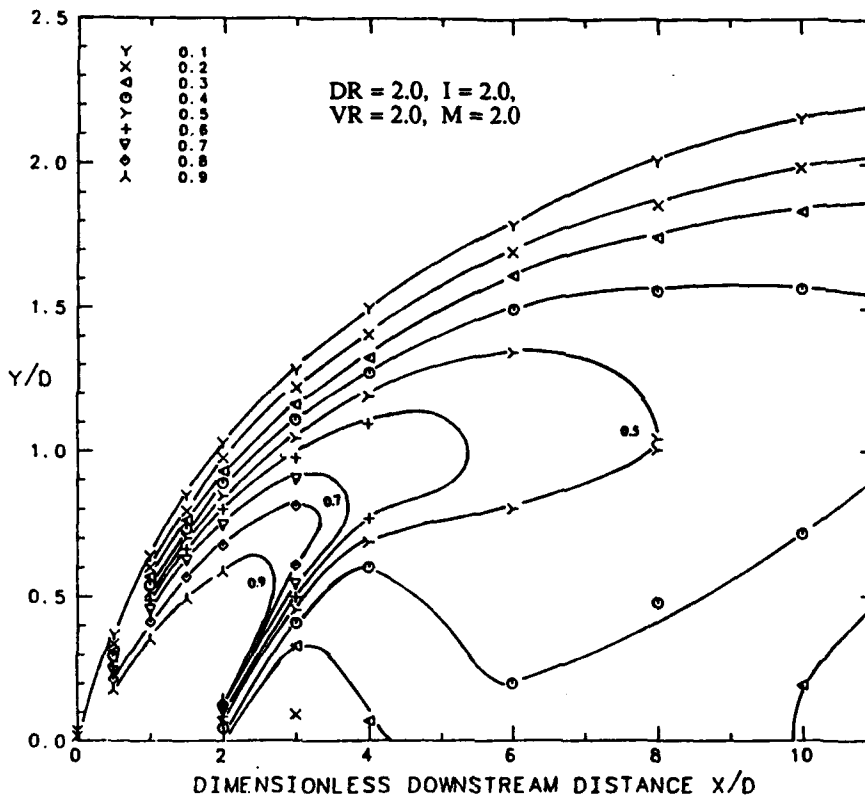


FIGURE 7. Dimensionless temperature contours along the jet centerline for $I = 2.0$, $DR = 2.0$, $VR = 1.0$, $M = 2.0$.

At low momentum flux ratios the jet remains attached to the surface as indicated by the contours shown in Figure 5 for a jet with $I = 0.125$. All of the contour levels less than $\theta = 0.9$ are perpendicular to the surface with the peak level (coldest temperature) at any given X/D position occurring at the wall. In contrast, Figure 6 shows an example of a higher momentum flux jet ($I = 0.5$) which has detached and then reattached to the surface. The $\theta = 0.7$ contour level in Figure 6 has been pushed over by the mainstream consequently being deflected toward the surface. The "curl" of the $\theta = 0.7$ contour is representative of the jet which initially detaches and then is deflected towards the surface and consequently reattaches to the surface. The contours indicate that the coldest temperature does not occur at the surface until slightly before $X/D = 8$ where the $\theta = 0.6$ contour level does not fold back on itself, and is instead perpendicular to the surface. For a jet with a still higher momentum flux ratio, $I = 2$, the contours shown in Figure 7 clearly indicate that the jet remains detached from the surface. Note that the contour levels from $\theta = 0.9$ to 0.5 close back on themselves and the maximum θ occurs much above the surface indicating a large warm air region under the jet. Given that the center of the jet is represented by the maximum θ level at each streamwise position, the jet appears to level out a little above $Y/D = 1$ and does not come back towards the surface.

Penetration of the jet into the mainstream also varies with momentum flux ratio. Because the low momentum jet shown in Figure 5 is flattened onto the surface and remains attached to the surface, the vertical penetration distance of the $\theta = 0.1$ contour of the jet at $X/D = 10$ is only slightly greater than $Y/D = 1$. Figure 6 shows that for an intermediate momentum flux ratio the jet has penetrated the mainstream to a height of $Y/D = 1.3$ by $X/D = 10$. Finally, Figure 7 shows the detached jet to have the largest penetration distance of $Y/D = 2.2$ at $X/D = 10$.

Although changes in jet conditions described above were attributed to changes in momentum flux ratio, scaling of the thermal field with respect to the velocity ratio or mass flux ratio has not been addressed. In the following sections we will show that the detachment-reattachment characteristics of the jets scale with the momentum flux ratio and not the velocity ratio, nor the mass flux ratio.

Momentum Flux Ratio Scaling

Three distinct ranges of momentum flux ratios were identified from the analysis of the non-dimensional temperature contours. The three ranges will be referred to as the low momentum flux ratio range ($I < 0.4$), the intermediate momentum flux ratio range ($0.4 < I < 0.8$), and the high momentum flux ratio range ($I > 0.8$). A discussion of each of the momentum flux ratio ranges follows.

In the low I range, the low momentum jets are flattened on to the plate causing the jets to remain attached to the surface as seen by the temperature contours shown in Figures 5, and 8. The momentum flux ratios for Figures 5 and 8 are $I = 0.125$ and 0.35 , respectively. The thermal field shown in Figure 5 shows that all of the temperature contours greater than 0.9 come into the surface perpendicular indicating the jet is attached to the surface. However, Figure 8, which has a slightly greater momentum flux ratio, shows that between the exit of the hole ($X/D = 1.74$) and $X/D = 3.5$, the 0.8 contour level is not perpendicular to the surface. Thus, the coldest temperature does not occur at the surface indicating a slight separation region very near the exit of the hole. This low range of momentum flux ratio is of special relevance for film cooling applications because the surface is getting the most "effective" cooling by the jet at the particular streamwise location.

For momentum flux ratios in the intermediate range $0.4 < I < 0.8$, the thermal fields in both

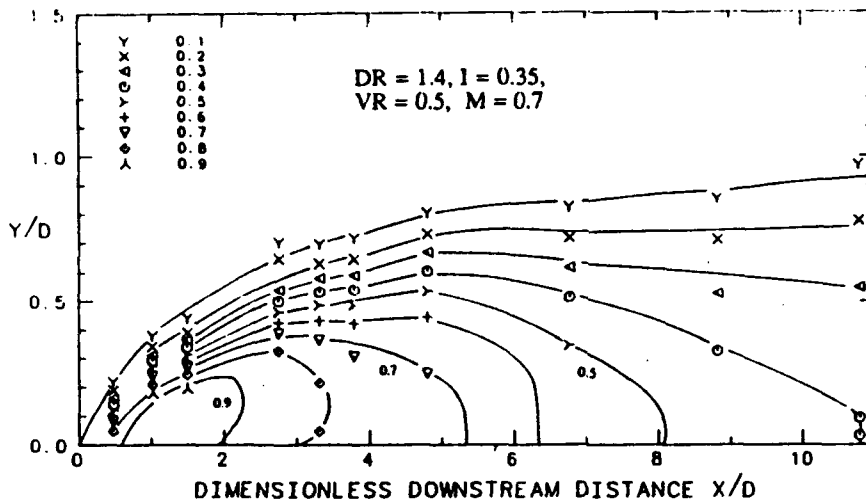


FIGURE 8. Dimensionless temperature contours along the jet centerline for $I = 0.35$, $DR = 1.4$, $VR = 0.5$, $M = 0.7$.

the near and the far fields appear quite similar which is indicated by the contours shown in Figures 9, 6, 10, 11, and 12 (stated in order of increasing momentum flux ratio). In the thermal field for a momentum flux ratio of $I = 0.4$, shown in Figure 9, the $\theta = 0.7$ contour is curling back toward the surface indicating jet reattachment, similar to that previously shown in Figure 6. Further downstream the $\theta = 0.5$ and 0.6 contour levels in Figure 9 are perpendicular to the surface indicating a reattached jet.

The non-dimensional temperature contours for a constant momentum flux ratio ($I = 0.5$) are

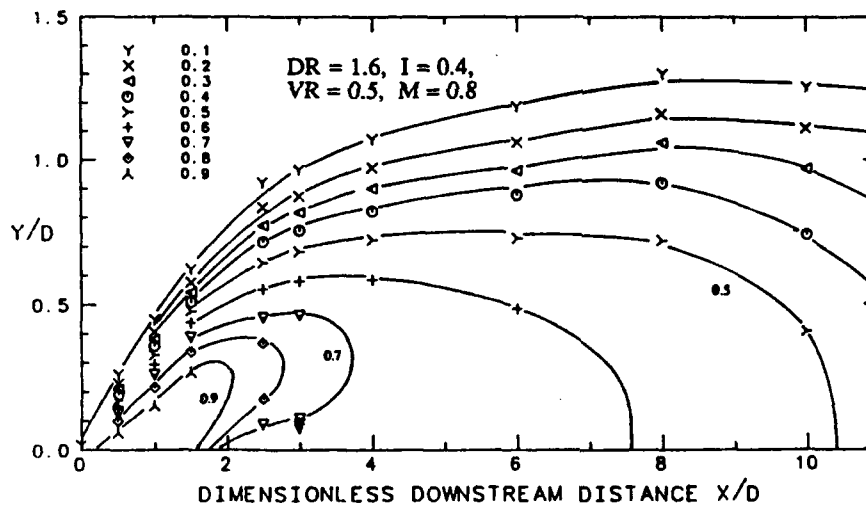


FIGURE 9. Dimensionless temperature contours along the jet centerline for $I = 0.40$, $DR = 1.6$, $VR = 0.5$, $M = 0.8$.

shown in Figures 6, 10 and 11. As stated previously, the corresponding profiles for $I = 0.5$, shown in Figure 4, collapse quite well for the full density ratio range studied in these experiments. All three of the jets at this intermediate momentum flux ratio ($I = 0.5$) show the curl over of the contour levels downstream of the film cooling hole, which is characteristic of the detaching/reattaching jet. The $\theta = 0.7$ contour level in Figures 6, 10, and 11 best exhibits this curling over. Figures 10 and 11 show a $\theta = 0.6$ contour "bubble" appearing because of the warm air nestled below the separated jet. The appearance of this bubble, representing higher temperatures (lower θ contours) below the jet also occurs in

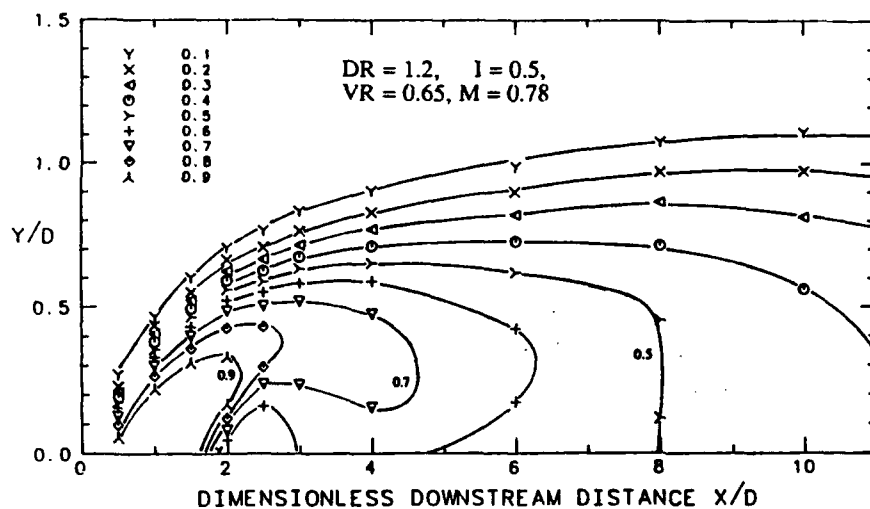


FIGURE 10. Dimensionless temperature contours along the jet centerline for $I = 0.5$, $DR = 1.2$, $VR = 0.65$, $M = 0.775$.

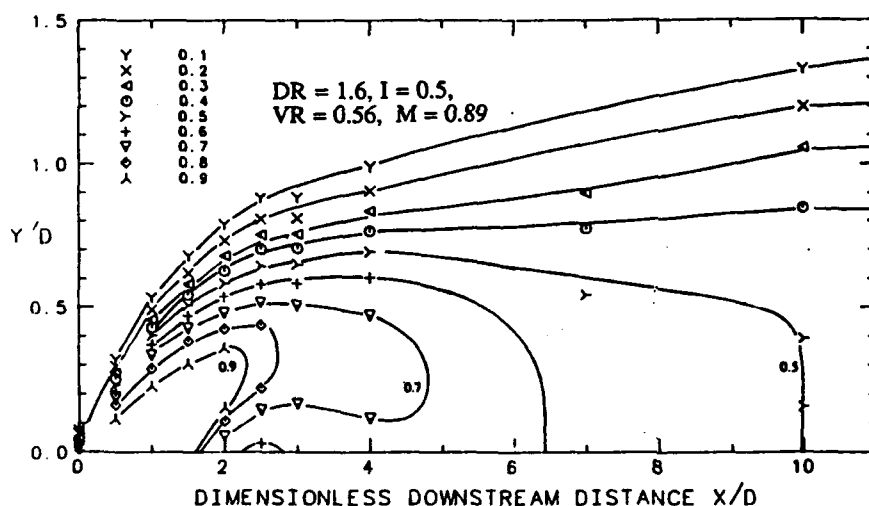


FIGURE 11. Dimensionless temperature contours along the jet centerline for $I = 0.5$, $DR = 1.6$, $VR = 0.56$, $M = 0.89$.

Figure 12 which shows the thermal field for a slightly greater momentum flux ratio ($I = 0.63$). This warm air bubble is also characteristic of a jet which has detached and then reattached. The warmer temperatures existing in this bubble next to the surface are detrimental to surface cooling, and hence the streamwise length of this warm region is significant.

In the high I range, the jet has enough momentum as it leaves the hole to penetrate far into the mainstream and remain detached from the surface as seen in Figures 13 and 7 (stated in

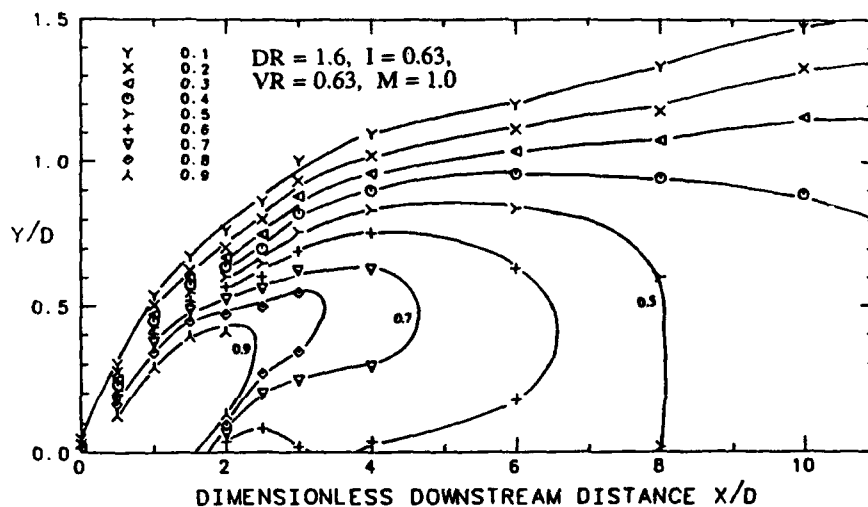


FIGURE 12. Dimensionless temperature contours along the jet centerline for $I = 0.63$, $DR = 1.6$, $VR = 0.63$, $M = 1.0$.

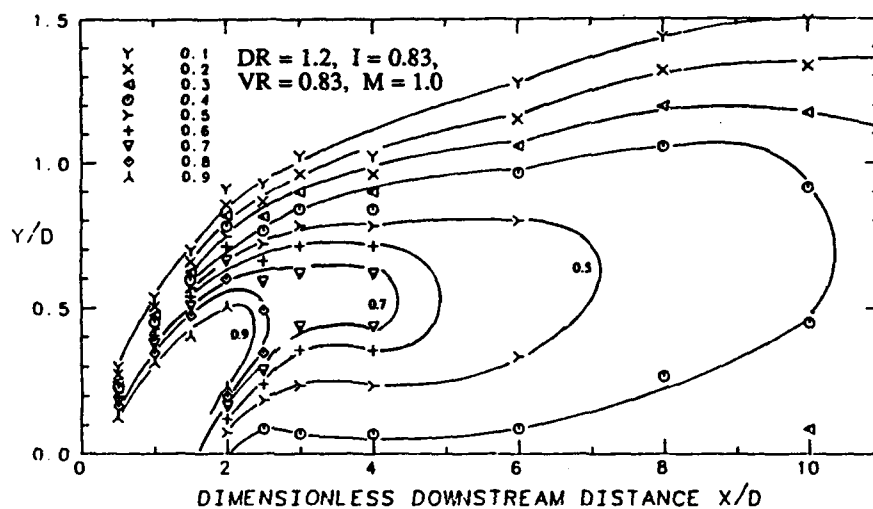


FIGURE 13. Dimensionless temperature contours along the jet centerline for $I = 0.83$, $DR = 1.2$, $VR = 0.83$, $M = 1.0$.

increasing I). Figure 13 shows that peak temperatures are displaced away from the wall. Immediately above the wall the θ levels are less than $\theta = 0.4$ and as a consequence the "effectiveness" of the film cooling has degraded.

Temperatures for a fully detached jet can be compared to temperatures for a jet which remains attached to the surface by looking at the $\theta = 0.5$ contours in Figures 5 and 7 for the lowest and highest momentum flux ratio jets, respectively. Even though in both cases the $\theta = 0.5$ temperature contour is sustained close to the same downstream location ($X/D = 9.5$ for the attached jet and $X/D = 8$ for the detached jet), the $\theta = 0.5$ level for the detached jet occurs much above the surface, thereby not protecting the surface. Although, the fully detached jet spreads towards the surface, the jet is not very useful in helping protect the surface because it is diluted by the mainstream air before reaching the surface.

Velocity Ratio Scaling

The scaling of the overall thermal field with momentum flux ratio is far better than that with velocity ratio. The velocity ratio parameter might appear to be a good scaling parameter when comparing the characteristics of the thermal fields presented in Figures 10 and 12 which have nearly the same velocity ratios (0.65 and 0.625, respectively). However, the velocity ratio parameter clearly fails to scale the thermal fields presented in Figures 6, 8, and 9 which also have a constant velocity ratio ($VR = 0.5$).

Scaling of the thermal field immediately above the hole exit was also examined in terms of momentum flux ratio and velocity ratio. Pietrzyk (1989) showed that the velocity field at the hole exit scaled with the velocity ratio. Pietrzyk deduced that a separation region occurred at the entrance to the hole which caused the jet to skew towards the upstream side hole at a high velocity ratio and towards the downstream side at a low velocity ratio. Thus, it is reasonable to expect the thermal field just above the exit of the hole to also scale with velocity ratio. However, when comparing the θ profiles above the film cooling hole (at $X/D = 1.5$) for constant velocity ratio, Figure 14, and constant momentum flux ratio, Figure 15, better

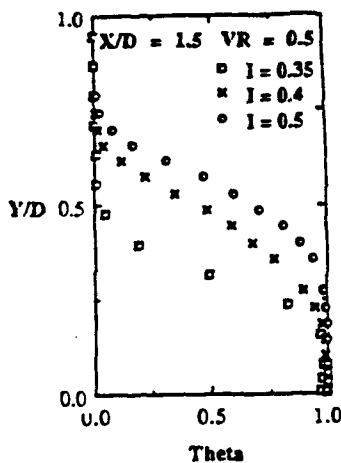


FIGURE 14. Dimensionless temperature profiles at a streamwise location of $X/D = 1.5$ for a constant velocity ratio ($VR = 0.5$).

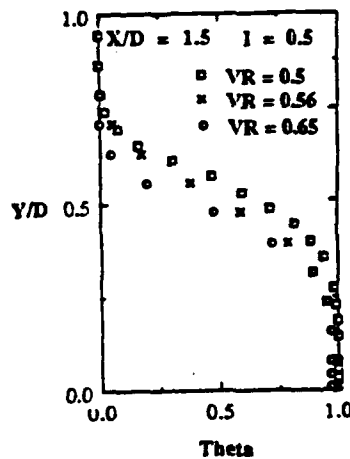


FIGURE 15. Dimensionless temperature profiles at a streamwise location of $X/D = 1.5$ for a constant momentum flux ratio ($I = 0.5$).

scaling is found for the momentum flux ratio. There is a relatively good collapse of the temperature profiles for a range of density ratios from $DR = 1.2$ to 2.0 at constant momentum flux, but there is approximately a 50% variation in the thickness of the profiles for constant velocity ratio. Evidently the thermal field above the hole is more strongly influenced by the deflection of the jet which depends on the momentum flux ratio, even though the velocity field at the jet exit scales with velocity ratio.

Mass Flux Ratio

The mass flux ratio was also investigated as a scaling parameter for the thermal field. Figures 6, 12, and 13 give the θ contours at a constant mass flux ratio ($M = 1$) for the full range of density ratios. Figures 9 and 10 also give θ contours for approximately the same mass flux ratio ($M \approx 0.8$). It is apparent that the mass flux ratio does not scale the detachment/reattachment scenarios. At the same mass flux ratio the thermal fields in Figures 6 and 12 show a detaching/reattaching jet while Figure 13 shows a detached jet. Similarly, the jet in Figure 9 is not as severely detached as the jet shown in Figure 10. Although the vertical penetration depths are similar for the $M \approx 0.8$ cases as seen in Figures 9 and 10, the vertical penetration depths are significantly different when comparing Figure 6 to Figures 12 and 13 for the $M = 1$ cases. Thus, the penetration depth does not scale with mass flux ratio.

Relevance to Previous Research

This phenomenon of the jet detaching and then reattaching to the surface was deduced in the past by Ko et. al. (1982), who observed a peak in the adiabatic wall effectiveness downstream of the hole. However, in the absence of a wide parameter range, they attributed the reattachment distance of the jet to changes in the mass-flux ratio. The measurements conducted in this study establish that the reattachment distance is a function of the momentum-flux ratio.

Detachment and reattachment of the film cooling jet was also deduced by Sinha et. al. (1990) based on adiabatic effectiveness measurements. The results of Sinha et. al. were in agreement with the present results in that the detachment and reattachment of the jet scaled with momentum flux ratio.

SUMMARY AND CONCLUSIONS

A detailed study of the thermal fields at different density, mass, velocity, and momentum flux ratios was carried out. The thermal fields were analyzed in terms of non-dimensional temperature profiles and contours. The governing characteristics of the thermal field were identified by whether the film cooling jet remained attached to the surface; detached and then reattached to the surface; or remained fully detached from the surface.

The momentum flux ratio was proven to be the scaling parameter which dictated the attached/detached state of the jet. The following three distinct ranges of the momentum flux ratio were identified: $I < 0.4$ where the jet remains attached to the surface; $0.4 < I < 0.8$ where the jet detaches and then reattaches to the surface; and $I > 0.8$ where the jet remains detached from the surface. Penetration of the jet into the mainstream was also found to scale with the momentum flux ratio.

The mass flux ratio and velocity ratio parameters were inadequate in scaling the thermal characteristics of the film cooling jets investigated.

ACKNOWLEDGEMENT

The authors gratefully acknowledge Wright-Patterson Research and Development Center and the Garrett Engine Division of the Allied-Signal Aerospace Company for support of this research. We also appreciate the assistance from David Dotson, Keith Matocha, and Kenneth Leonore.

REFERENCES

- Demuren, A.O., Rodi, W., Schonung, B., 1985, "Systematic Study of Film Cooling with a Three-Dimensional Calculation Procedure," 1985 Beijing International Gas Turbine Symposium and Exposition, ASME Paper 85-IGT-2.
- Foster, N.W., and Lampard, D., 1978, "The Flow and Film Cooling Effectiveness Following Injection Through a Row of Holes," *Journal of Engr. for Power*, Vol. 100, p. 303.
- Ko, S-Y, Liu, D-Y, Yao, Y-Q, Li J., and Tsou, F.K., 1982, "Film Cooling Effectiveness of Discrete Holes Measured by Mass Transfer and Laser Interferometer," Seventh Annual International Heat Transfer Conference.
- Pederson, D.R., Eckert, E.R.G., and Goldstein, R.J., 1977, "Film Cooling with Large Density Differences between the Mainstream and Secondary Fluid Measured by the Heat-Mass Transfer Analogy," *ASME Journal of Heat Transfer*, Vol. 99, pp. 620-627.
- Pietrzyk, J.R., 1989, "Experimental Study of the Interaction of Dense Jets with a Crossflow for Gas Turbine Applications," Ph.D. Dissertation, University of Texas at Austin.
- Pietrzyk, J.R., Bogard, D.G., and Crawford, M.E., 1989a, "Hydrodynamic Measurements of Jets in Crossflow for Gas Turbine Film Cooling Applications", *Journal of Turbomachinery*, Vol. 111 pp. 139-145.
- Pietrzyk, J.R., Bogard, D.G., and Crawford, M.E., 1989b, "Effects of Density Ratio on the Hydrodynamics of Film Cooling," ASME Paper No. 88-GT-194.
- Ramsey, J.W., and Goldstein, R.J., 1971, "Interaction of A Heated Jet with a Deflecting Stream," *ASME Journal of Heat Transfer*, Vol. 93, p. 365.
- Sinha, A.K., Bogard, D.G., and Crawford, M.E., 1989, "Film Cooling Effectiveness Downstream of a Single Row of Holes with Variable Density Ratio," Submitted for presentation at the International Gas Turbine Conference, Brussels, Belgium.
- Yosida, T., and Goldstein, R.J., 1984, "On the Nature of Jets Issuing From a Row of Holes into a Low Reynolds Number Mainstream Flow," *Journal of Engineering for Gas Turbines and Power*, Vol. 106, p. 612.

Appendix B

Generation of Very High Freestream Turbulence Levels and the Effects on Heat Transfer

by

K. A. Thole, J. Whan-Tong, and D. G. Bogard

**Presented at the *Eighth Symposium on Turbulent Shear Flows*
Munich, Germany
September, 1991**

Generation of Very High Freestream Turbulence Levels and the Effects on Heat Transfer

by

Karen A. Thole, Janine Whan-Tong, and David G. Bogard

Mechanical Engineering Department
The University of Texas at Austin
Austin, TX 78712

ABSTRACT

Attempts at establishing reliable correlations for the effects of high freestream turbulence on heat transfer have been hampered by the relatively low turbulence levels used in most studies, or the complex flow fields when using free jets to obtain high freestream turbulence. In the present study a new freestream turbulence generator was developed which produced a freestream turbulence field with larger turbulence levels and significantly smaller length scales than have been previously possible in a uniform flow test section. Significant enhancement of heat transfer was found to occur due to high freestream turbulence levels. The effect on heat transfer was found to correlate best using a parameter based on the turbulence level, integral length scale, and the enthalpy thickness Reynolds number.

NOMENCLATURE

C_f	Friction coefficient
C_{f0}	Friction coefficient for a standard boundary layer
HB	Hancock/Bradshaw parameter
L_u^e	Dissipation length scale
Re_Δ	Enthalpy thickness Reynolds number
Re_θ	Momentum thickness Reynolds number
St	Stanton number
St_0	Stanton number for a standard boundary layer
St'	Stanton number based on u'_{max}
TLR	Turbulence scaling parameter
TA_{xR}	Turbulence scaling parameter
Tu	Turbulence intensity, u'/U_∞
u'	Fluctuating velocity in streamwise direction
U_∞	Mainstream velocity in streamwise direction
v'	Fluctuating velocity in normal direction
x	Streamwise distance measured from virtual origin
x_h	Streamwise distance measured from the start of the heater plate
y	vertical distance

β	Low Re_θ function
Δ	Enthalpy thickness
δ_{99}	Velocity boundary layer thickness
δ_{th}	Thermal boundary layer thickness
Λ_x	Integral turbulent length scale
θ	Momentum thickness

INTRODUCTION

The goals of this study were to develop a highly turbulent freestream flowfield (turbulence levels of nominally 20%) and then study the effects of this highly turbulent freestream on heat transport. The development of the turbulent boundary layer with a highly turbulent freestream is relevant in predicting convective heat transfer in many flow geometries. High freestream turbulence levels have dramatic effects on heat transfer in such devices as heat exchangers, combustors, and gas turbine blades. For example, typical freestream turbulence levels which occur in gas turbines have been measured by Koutmos and McGuirk (1989) to be greater than 20%. Dunn et al. (1986) compared the heat transfer data taken in a real turbine to those predictions based on turbulent heat transfer correlations. They reported the correlations underpredicted their measured heat transfer by as much as 100 percent on the blade pressure side and 30 percent on the suction side.

There are several heat transfer correlations reported throughout the literature which have been developed to account for the enhancement of high freestream turbulence effects on both the wall shear stress and wall heat transfer. These correlations have been developed from both grid-generated turbulence, where the levels are 7% or lower, and high freestream turbulence studies, where the highest levels, to date, have been reported at 60% by Maciejewski and Moffat (1989a). The enhancement of heat transfer is typically measured by a ratio of Stanton numbers, St/St_0 where St_0 is for a standard boundary layer at either the same momentum or enthalpy thickness Reynolds number as for the measured high freestream turbulence St . These correlations, as will be discussed below, are typically based on either the velocity boundary layer characteristics, such as thickness (δ_{99}), momentum thickness (θ), and momentum Reynolds number (Re_θ); or

thermal boundary layer characteristics, such as thickness (δ_{th}), enthalpy thickness (Δ), and enthalpy thickness Reynolds number (Re_Δ). In addition, some of the correlating parameters include the turbulence levels (Tu), the integral length scale (Λ_x), and the dissipation length scale (L_u^E) defined by Simonich and Bradshaw (1978) as

$$L_u^E = - \frac{\overline{(u^2)^2}}{U_\infty \frac{d(u^2)^2}{dx}} \quad (1)$$

Most of the heat transfer data reported in the literature is for grid-generated turbulent freestreams where levels are typically less than 7%. Early grid-generated turbulence studies showed that the only effect that grid-generated turbulence had was to move the transition location upstream (Kestin et al. (1961)). Later, Simonich and Bradshaw (1978), showed that heat transfer enhancement increases with increasing turbulence intensities. Simonich and Bradshaw found a relatively weak dependence on the L_u^E/δ_{99} ratio, with a decrease in heat transfer enhancement as L_u^E/δ_{99} increased. Simonich and Bradshaw evaluated the St/St_0 ratio at a constant Re_θ .

Hancock and Bradshaw (1983) studied the effect of grid-generated turbulence only on velocity boundary layers. They correlated their skin friction coefficient ratio (C_f/C_{f0}), where C_{f0} is for a standard boundary layer at the same Re_θ , with a parameter they defined as,

$$HB = \frac{Tu}{(\frac{L_u^E}{\delta_{99}} + 2)} \quad (2)$$

Hereafter, we will refer to this parameter as the HB parameter. They found the C_f/C_{f0} ratio was a nonlinear function of the HB parameter. The range of the HB parameter which they investigated was between $HB = 0.5$ and $HB = 2$.

Blair found a low Re_θ effect where the skin friction enhancement is dampened. Blair developed an empirical relation, $\beta = (3 e^{-Re_\theta/400} + 1)$ to account for this damping. This damping term is significant at low Re_θ , i.e. at $Re_\theta = 700$, $\beta = 1.5$, but asymptotes to unity near $Re_\theta = 2000$ where $\beta = 1.02$. Later, Blair (1983) applied the Hancock/Bradshaw correlation to evaluate whether it would also collapse the enhancement of grid-generated turbulence on heat transfer, namely St/St_0 , evaluated at the same Re_θ . Blair modified the Hancock/Bradshaw correlation by using Reynolds analogy factor, $2St/C_f = 1.3$ and also applied β to the heat transfer results.

Baskaran, Abdellatif, and Bradshaw (1989) also applied the Hancock/Bradshaw correlation to their grid-generated turbulence results between $HB = 0.2$ and 1 where they evaluated St/St_0 at a constant Re_θ . Their measured heat transfer enhancement was significantly underpredicted. Baskaran et al. suggested changing the denominator of the HB parameter which would give a better fit to their data.

The very high freestream turbulence studies to date, where the turbulence production used techniques other than a grid (studies where turbulence levels greater than 7%), include MacMullin, Elrod and Rivir (1989), Maciejewski and Moffat (1989a,b), and Ames and Moffat (1990a,b). MacMullin et al. generated turbulence levels up to 20% using a wall jet with a characteristic highly non-uniform vertical mean velocity. Maciejewski and Moffat were able to achieve turbulence levels up to 60% using a free jet facility with a constant temperature plate positioned off-axis and several jet diameters downstream of the jet exit plane. Similar to MacMullin et al., Maciejewski and Moffat also had a highly nonuniform mean flowfield. Ames and Moffat achieved high turbulence levels (up to 16%) by simulating an annular combustor by injecting the flow through a series of wall slots and jet holes prior to the wind tunnel contraction.

MacMullin et al. applied the HB scaling parameter using the integral length scale as opposed to the dissipation length scale and evaluated the St/St_0 ratio at a constant Re_θ . Even though they applied Blair's low Re_θ function, there was a large scatter in the data. For example at an $HB = 3.25$, the St/St_0 ratio ranged from 1.48 to 1.8.

Maciejewski and Moffat (1989b) found that their data best scaled with a parameter they defined as St' which uses the maximum fluctuating streamwise velocity component as the velocity scale. They proposed that St' was a function of turbulence level alone with a maximum St' occurring near a turbulence level of 11%. Maciejewski and Moffat were able to collapse their data and some of the data available in the literature at lower turbulence levels, such as Blair, to within $\pm 15\%$ of their correlation.

Ames and Moffat (1990a) compared their St data to the Hancock/Bradshaw correlation using the thermal boundary layer thickness and comparing the St/St_0 ratio at a constant Re_Δ . Ames and Moffat found that their St/St_0 ratio agreed well with the original correlation (not corrected using the Reynolds analogy factor). They also proposed a scaling parameter (Ames and Moffat, 1990b) which they call TLR, defined as

$$TLR = Tu \left(\frac{\Delta}{L_u^E} \right)^{0.33} \left(\frac{Re_\Delta}{1000} \right)^{0.25} \quad (3)$$

The TLR parameter showed promise in scaling both their own data as well as the data from Maciejewski and Moffat. However, Λ_x instead of L_u^E was used for Maciejewski and Moffat's data. In addition, the TLR parameter uses enthalpy thickness as opposed to boundary layer thicknesses which, as Ames and Moffat point out, are difficult to measure in highly turbulent fields.

As indicated above, in evaluating the different scaling parameters for high turbulence heat transfer and the correlations that have been proposed in the literature, we have found that these correlations have been applied in a variety of different and sometimes contradictory ways. For instance, the integral length scale and dissipation length scales have been interchanged as well as interchanging whether the Stanton number ratio, St/St_0 , is evaluated at a constant Re_θ or Re_Δ . In particular, the ratio

of integral length scale to dissipation length scale is quite different for different turbulence fields, e.g. $L_u^E/\Lambda_x = 1.1$ for Simonich and Bradshaw (1978) and $L_u^E/\Lambda_x = 1.5$ for Blair (1983). Based on these variations in the L_u^E/Λ_x ratio for different flowfields, it is imperative in applying scaling parameters based on a turbulence length scale that a consistent length scale be used. The interchanging of these parameters throughout the literature has confounded the interpretation of the correlations and may well contribute to the large scatter in the existing data.

In this paper, we have addressed generating high freestream turbulence levels of nominally 20% and the effects on heat transfer. We were particularly interested in determining which of the turbulence length scales, that is the dissipation or the integral scale, serve as a better scaling parameter for high freestream turbulence effects. We have used the thermal boundary layer parameters in evaluating the HB and TLR scaling parameters. The remainder of the paper discusses the experimental facility and data acquisition techniques used; quantifies the highly turbulent flowfield; and gives the surface heat transfer results for the highly turbulent case.

EXPERIMENTAL FACILITIES AND DATA ACQUISITION

This section of the paper describes the experimental facilities which includes the wind tunnel, the turbulence generator, and constant heat flux plate as well as the instrumentation used to measure the velocity and surface temperatures. Details of the facility and instrumentation were presented by Whan-Tong (1991).

Experiments were conducted in a closed-loop boundary layer wind tunnel driven by a 5 Hp fan. Heat exchangers, located downstream of the fan, maintained the mainstream flow temperature. The test section was 180 cm long, 61 cm wide and 15.2 cm high. A suction loop was added to the tunnel to remove the upstream boundary layer.

High freestream turbulence levels were produced by normal jets injected from both the floor and roof of the wind tunnel at the inlet of the test section. The turbulence generator, shown in figure 1, consisted of a top and a bottom row of opposing jets, each with a row of 35 holes having a diameter 5.08 mm and spaced 3 diameters apart. The test plate was located 40 cm downstream of the jet holes. Flow for the turbulence generator was diverted from upstream of the wind tunnel fan and was driven by a 7.5 Hp blower. The temperatures of the wind tunnel mainstream and turbulence generator jets were matched by cooling the turbulence generator flow loop by injecting small amounts of low temperature nitrogen. After being cooled, the flow was equally split between two plenums located on the roof and floor of the wind tunnel. The velocity ratio of the jets-to-mainstream dictated the turbulence level. For these experiments, a velocity ratio of 11 was used with a mainstream velocity of nominally 8 m/s.

Downstream of the suction slot, shown in figure 1, was an unheated, sharp leading edge followed by a

constant heat flux test surface. The unheated sharp leading edge was 12 cm long with a 2.4 mm trip wire mounted 2 cm from the start of the plate. The constant heat flux plate which consisted of a serpentine, monel heating element was sandwiched between two Kapton films. The length and width of the plate were 1.4 m and 0.6 m, respectively. The heater plate was bonded to a 12.7 mm thick fiberglass composite (G-10). Below the plate were several layers of insulation to minimize conduction losses.

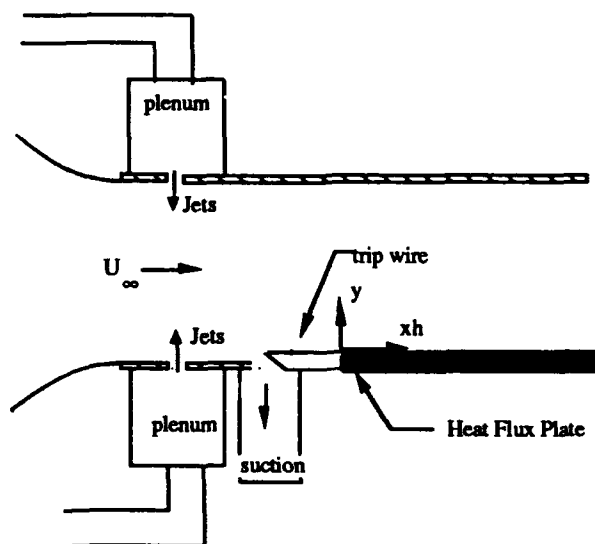


Figure 1. Schematic of the turbulence generator and heat flux plate assembly.

The total heat flux for these experiments was approximately 260 W/m^2 which resulted in a temperature differential of nominally 10°C . Low temperature differentials were used to avoid property variation effects. A DC power supply was used as the supply to the resistive heater. A significant radiation correction was required to obtain the net convective heat flux. The radiation correction was based on the radiation exchange between the heat flux plate and the wind tunnel roof. Surface temperatures of the wind tunnel roof were measured so that an accurate measure of the surrounding radiative temperatures could be made. The radiative heat flux was at most 17% of the total heat flux.

A two-component laser Doppler velocimeter (LDV) was used to measure the streamwise and vertical velocity components. The signal was processed by counters and then input to a computer. Velocity bias corrections were done using residence time weighting. The flow was seeded using smoke which was generated from burning incense sticks. The tar from the smoke was filtered out by using steel wool and then cooled before being injected into the tunnel.

Single sensor hot-wire measurements were made to determine the integral scales. Integral length scales, Λ_x , were deduced from the integral time scales based on Taylor's hypothesis of "frozen turbulence". The integral

length scales discussed in this paper were measured at a lower freestream velocity (~ 4 m/s) but at the same turbulence levels, the same physical turbulence generator configuration, and the same ratio of jet-to-mainstream velocity.

The surface temperatures were measured using Type E surface thermocouple ribbons, described by Sinha et al. (1991) that were glued to the constant heat flux plate. Output from 63 thermocouples was multiplexed into a data acquisition computer where it was processed on-line to indicate Stanton number distributions.

TURBULENCE FIELD

The streamwise decay of u'/U_∞ and v'/U_∞ is shown in figure 2 with respect to the streamwise distance measured from the start of the heater plate. At 25 cm downstream of the start of the heater plate, at which point where the unheated starting length effects are negligible, $Tu = u'/U_\infty = 21\%$. Tu decays to 11% at 90 cm downstream which was the furthest point at which heat transfer effects were evaluated.

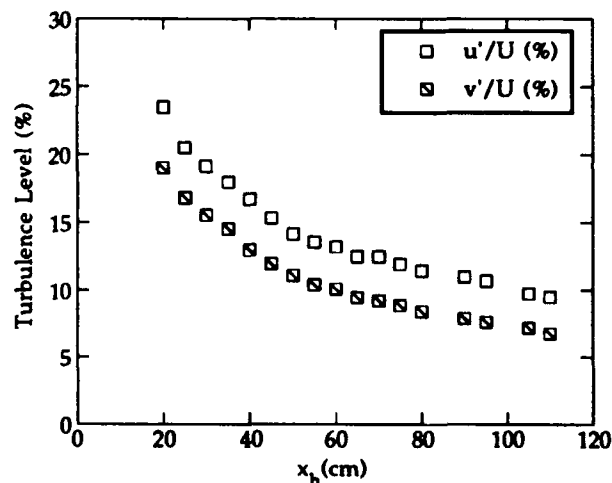


Figure 2. Streamwise turbulent decay for the highly turbulent flowfield along the heat flux plate.

The turbulent dissipation length scales, L_u^ϵ , were deduced from the u'^2 decay and the u' and U_∞ measurements. The ratio of dissipation to boundary layer thickness decreased from $L_u^\epsilon/\delta_{99} = 3.4$ at $x_h = 25$ cm downstream to $L_u^\epsilon/\delta_{99} = 3.0$ at $x_h = 90$ cm downstream. The Λ_x/δ_{99} ranged from 1.8 at $x_h = 25$ cm to 1.4 at $x_h = 90$ cm. Integral scales were only measured at a nominal freestream velocity of $U_\infty = 4$ m/s. The ratio of the dissipation scale to the integral scale was a relatively constant value of $L_u^\epsilon/\Lambda_x = 3.1$.

Inherent in generating very high turbulence levels is the difficulty of maintaining a uniform mean flowfield. The mean flow uniformity of the highly turbulent field in the streamwise, lateral, and vertical directions were measured. The streamwise variation of freestream

velocity increased by 4.5 % between $x_h = 25$ cm and 70 cm but then remained within $\pm 1.5\%$ beyond $x_h = 70$ cm. The lateral variation in the mean velocity was nominally $\pm 10\%$ at $x_h = 25$ cm downstream, but improved further downstream. The vertical non-uniformity at $x_h = 25$ cm was $\pm 2.5\%$. Although this does not appear to be large, the vertical velocity profile had a continuous gradient which made defining the boundary layer edge difficult. In order to identify the boundary layer edge at this location, the boundary layer was heated and the air temperature profile was measured and then used to identify the boundary layer edge. Further downstream, at 60 cm and 75 cm, the vertical profile was flat within $\pm 1\%$.

HIGH TURBULENCE HEAT TRANSFER RESULTS

The enhancement of heat transfer for the highly turbulent flowfield as compared with the standard boundary layer benchmark data and correlation (given by Kays and Crawford, 1980) is shown in figure 3. The Stanton number distributions are given as a function of Reynolds number based on streamwise distance, Re_x , where x is measured from the virtual origin located 0.36 m upstream of the heat flux plate. The virtual origin was deduced from the measured momentum thickness. The Stanton numbers shown in figure 2 for both the standard boundary layer and the high freestream turbulence cases show the effect of the unheated starting length. To avoid the unheated starting length effect, only the Stanton number data downstream of this region ($Re_x > 3 \times 10^5$, $x_h = 25$ cm), and in the centerline of the plate, were analyzed in this study. For the highly turbulent case, the spanwise variation of surface temperature and freestream velocity was $\pm 6\%$ and $\pm 10\%$, respectively which resulted in a $\pm 9\%$ variation in Stanton number. Further downstream at 50 cm, where the velocity field was more uniform, the spanwise variation in surface temperature reduced to $\pm 4\%$.

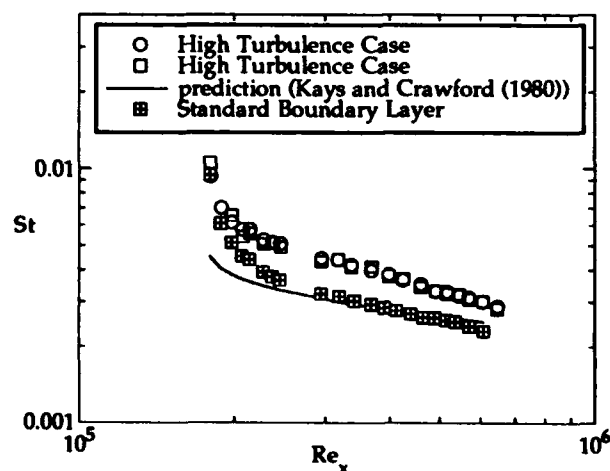


Figure 3. Stanton number distribution for both the standard boundary layer benchmark test and high freestream turbulence case.

In applying the Hancock and Bradshaw correlation as well as the Ames and Moffat correlation, St/St_0 is found at a constant enthalpy thickness Reynolds number, Re_Δ . The enthalpy thickness, Δ , can be quantified by either measuring both the velocity and temperature profiles directly or can be found by using an energy balance which results in $\Delta = St \cdot x_h$ where x_h is the distance along the heater plate. The velocity and temperature profiles were measured at 25 cm and 60 cm downstream of the start of the heater. The enthalpy thicknesses deduced from the profiles were 36% and 52% lower than those calculated using the $St \cdot x_h$. This discrepancy was attributed to the difficulty of accurately measuring the enthalpy thickness for the thin boundary layer, and to effects due to the additional energy flux by turbulent fluctuations which become significant at high turbulence levels. Similar difficulties in directly measuring enthalpy thickness were encountered by Ames and Moffat (1990b) who found deviations as much as 30% from the $St \cdot x_h$ value. Ames and Moffat attributed this result to the spanwise variation of enthalpy thickness. Because of the difficulty in directly measuring the enthalpy thickness, in this study the enthalpy thickness was deduced from $St \cdot x_h$ values.

The measured Stanton number distribution for the standard boundary layer shown in figure 3 follows the correlation for the most part, but decreases at a greater rate resulting in a 7 % deviation at an $Re_x = 6.1 \times 10^6$. Also shown in figure 3 are two experimental data sets, under nominally the same conditions, for the high freestream turbulence showing the enhancement of heat transfer with the high freestream turbulence. The freestream velocity for the standard boundary layer was 7.8 m/s while the freestream velocity for the highly turbulent case ranged from 7.6 m/s at $x_h = 25$ cm to 8.2 m/s at the end of the plate, $x_h = 90$ cm. The experimentally measured Stanton numbers were used as the reference St_0 in evaluating freestream turbulence effects. The experimentally measured Stanton numbers were used rather than the values from the correlation so that any experimental bias errors would be nullified.

Figure 4 shows the measured St/St_0 ratio based on the same streamwise location. Also shown in figure 4 is the Ames and Moffat (1990a) data. Although our data shows a larger effect on the heat transfer enhancement, between $x = 25$ cm and 70 cm, both sets of data are asymptotically approaching $St/St_0|_{x_h} = 1.25$ beyond $x = 70$ cm.

Of particular interest in figure 4 is the reduced enhancement of the heat transfer at the start of the heat flux plate. Our data, as well as the Ames and Moffat data, show that at the start of the heat flux plate, where the turbulence levels are the highest, there is essentially no enhancement of the heat transfer. This suppression of the enhancement effect could be due to either a low Re_Δ effect or a large ratio of turbulence length scale to thermal boundary layer thickness, Λ_x/Δ . In both data sets the enhancement increases in the downstream direction until there is a peak in the enhancement. If we assume that the

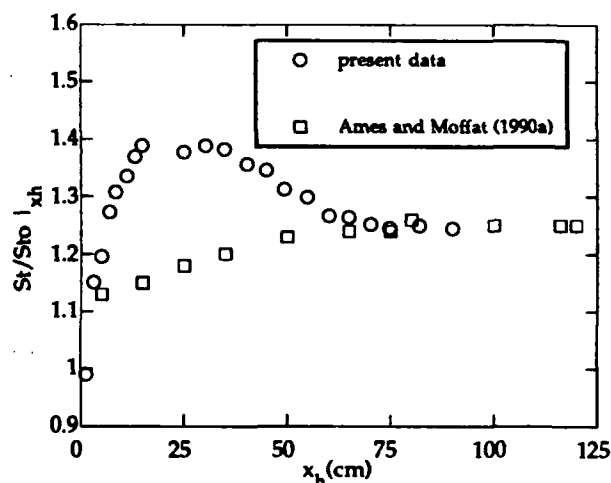


Figure 4. Ratio of high freestream turbulence St to the standard boundary layer St_0 at the same streamwise locations.

suppression of the heat transfer has become negligible at this peak, it is of interest to contrast Re_Δ and Λ_x/Δ for the two data sets at the peak. These values are $Re_\Delta = 520$ and $\Lambda_x/\Delta = 29$ and 36 for our data and Ames and Moffat, respectively. Clearly, the Re_Δ values are quite different, but the Λ_x/Δ are very close indicating that the suppression of the heat transfer enhancement at the beginning of the plate is due to a length scale ratio effect.

Figure 5 compares our data as well as the Ames and Moffat data with the Hancock/Bradshaw correlation originally developed to scale C_f/C_{f0} as well as the Reynolds analogy modified Hancock/Bradshaw correlation. Data taken by Ames and Moffat agree reasonably well for $1.25 < HB < 2$ with the original Hancock/Bradshaw correlation. Beyond $HB = 2$, which is also beyond the original correlation, the Ames and Moffat St/St_0 continues to follow the same trend. Our data extends between $1.9 < HB < 3.8$, but is significantly above both the Ames and Moffat data, as well as an extrapolation of the original Hancock/Bradshaw and modified correlations.

Our data was taken at relatively low Re_Δ , i.e. $704 < Re_\Delta < 1054$, which suggests the use of Blair's (1983) low Re_Δ correction. However, the low Re_Δ correction reduces the HB parameter which leads to worse agreement with the correlation.

The Stanton number correlation, given by Maciejewski and Moffat (1989b), based on the fluctuating streamwise velocity component is shown in figure 6. Our data shows a consistent trend in this format and falls on the lower bounds of the correlation with a maximum value near a turbulence level of 10%. However, there are clear differences in terms of the St' parameter between our data and that of Ames and Moffat (1990b) and the Maciejewski and Moffat (1989b) correlation.

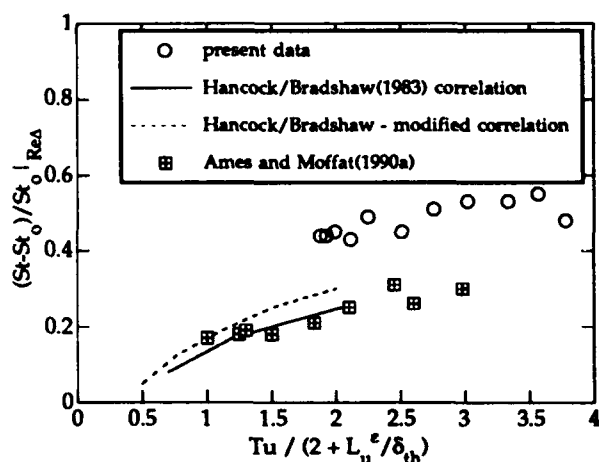


Figure 5. Comparison of present data with the Hancock/Bradshaw(1983) correlation.

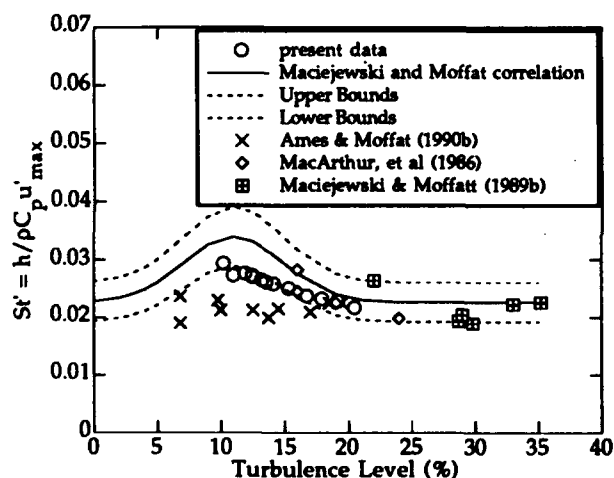


Figure 6. Comparison of present data with the Maciejewski and Moffat (1989b) correlation.

A new parameter for correlating high turbulence effects on heat transfer was suggested by Ames and Moffat (1990b) as described in the introduction. The Ames and Moffat TLR parameter is based on the turbulence level, dissipation length scale, and Re_Δ . Figure 7 shows our data compared to that of Ames and Moffat. As is evident from figure 7, there is still a distinct difference between the two data sets in terms of the TLR parameter.

In an attempt to better collapse the data, we evaluated the TLR parameter using the integral length scale, TA_{XR} , as opposed to the dissipation length scale. For this analysis we assumed that the L_u^ϵ / Λ_x ratio measured at 4 m/s was valid at 8 m/s. Figure 8 shows results in terms of the TA_{XR} parameter for our data, the data of Ames and Moffat (1990b), and the data of Maciejewski and Moffat (1989b). In using the TA_{XR} parameter our data has been significantly shifted relative to Ames and Moffat's data

such that all three data sets fall nominally in line. This shift occurred because of the significant differences in the ratio of the dissipation length scale to the integral length scale for our experiments, $L_u^\epsilon / \Lambda_x \approx 3.1$, compared to Ames and Moffat, $L_u^\epsilon / \Lambda_x \approx 2.2$. The TA_{XR} parameter is the best parameter that has been investigated in this paper for collapsing all three high freestream turbulence data sets.

CONCLUSIONS

The new freestream turbulence generator developed as part this study produced a freestream turbulence field with larger turbulence levels and significantly smaller length scales than have been previously possible in a uniform

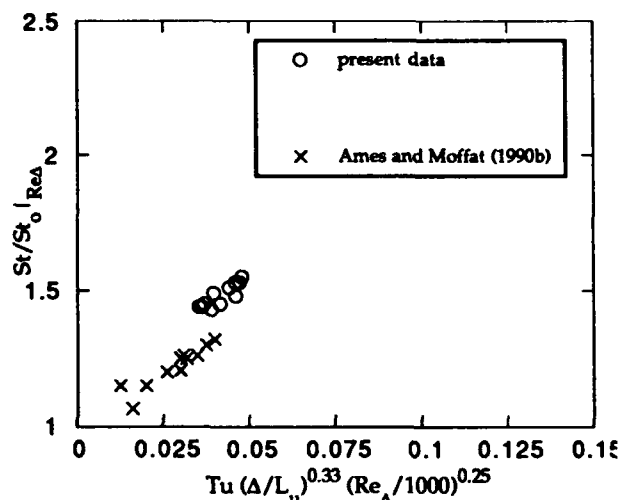


Figure 7. Comparison of present data to the Ames and Moffat (1990b) correlation using the turbulent dissipation scale.

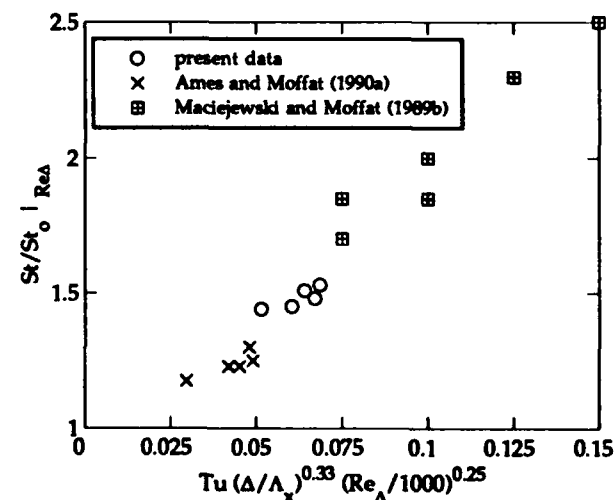


Figure 8. Comparison of present data to the Ames and Moffat (1990b) correlation using the turbulent integral scale.

flow test section. Effects of this high freestream turbulence on heat transfer were evaluated in terms of a variety of different correlations that have been published in the literature. Large enhancements to heat transfer were found at relatively low Re_θ which was somewhat contrary to the damping effect at low Reynolds number found for C_f by Blair (1983). However, significant suppression of the freestream turbulence effects was found to occur at the start of the heated surface which was attributed to the large turbulence length scale to thermal boundary layer thickness ratio at this location. Comparisons to the data of Ames and Moffat (1990b) were particularly revealing because similar turbulence levels were used, but the turbulence length scales were quite different. The TLR parameter suggested by Ames and Moffat was modified by using the integral length scale rather than the dissipation length scale. This $TA_{\lambda R}$ parameter was the best parameter investigated in this paper for collapsing all three high freestream turbulence data sets.

ACKNOWLEDGEMENTS

We gratefully acknowledge the support of the Wright-Patterson Research and Development Center and Allied-Signal Aerospace Corporation. We would also like to thank Dr. Michael Crawford for his helpful discussions.

REFERENCES

- Ames, F.E. and Moffat, R.J., (1990a) "Effects of Simulated Combustor Turbulence on Boundary Layer Heat Transfer," AIAA/ASME Thermophysics and Heat Transfer Conference, Seattle, pp. 11-17.
- Ames, F.E. and Moffat, R.J., (1990b) "Heat Transfer with High Intensity, Large Scale Turbulence: The Flat Plate Turbulent Boundary Layer and the Cylindrical Stagnation Point," Stanford University Report No. HMT-44.
- Baskaran, V., Abdellatif, O.E., and Bradshaw, P. (1989) "Effects of Free-stream Turbulence on Turbulent Boundary Layer with Convective Heat Transfer," Seventh Symposium on Turbulent Shear Flows, Stanford University, paper 20.1.
- Blair, M.F. (1983) "Influence of Free-Stream Turbulence on Turbulent Boundary Layer Heat Transfer and Mean Profile Development," Part I - Experimental Data, ASME J Heat Transfer, Vol. 105, pp. 33-40.
- Dunn M.G., Martin, H.L., Stenek, M.J. (1986) "Heat Flux and Pressure Measurements and Comparison with Prediction for a Low Aspect Ratio Turbine Stage," ASME Gas Turbine Conference, 86-GT-79, Dusseldorf, West Germany.
- Hancock, P.E. and Bradshaw, P. (1982) "The Effect of Free-Stream Turbulence Boundary Layer Development," ASME J Power Engineering.
- Kays, W. M.; Crawford M. E. (1980) *Convective Heat and Mass Transfer, Second Edition*, McGraw-Hill, New York.
- Kestin, J., Maeder, P.F. and Wang, H.E. (1961) "Influence of Turbulence on the Heat Transfer from Plates with and without a Pressure Gradient," International Journal of Heat and Mass Transfer, Vol. 3, p. 133.
- Koutmos, P. and McGuirk, J. J., (1989) "Isothermal flow in a Gas Turbine Combustor — a Benchmark Experimental Study," Experiments in Fluids, Vol. 7, p. 344.
- MacArthur, C.D. (1986) "Fluid Dynamics and Heat Transfer of the Circular Tangential Wall Jet," Ph.D. Thesis, University of Dayton, Dayton, Ohio.
- Maciejewski, Paul K. and Moffat, Robert J. (1989a) "Effects of Very High Turbulence on Heat Transfer," Seventh Symposium on Turbulent Shear Flows, Stanford University, August 21-23, 1989.
- Maciejewski, P. K. and Moffat, R. J. (1989b) "Heat Transfer with Very High Free Stream Turbulence," Stanford University, Report HMT-42.
- MacMullin, R., Elrod, W., and Rivir, R. (1989) "Free-Stream Turbulence From a Circular Wall Jet on a Flat Plate Heat Transfer and Boundary Layer Flow," Transactions of the ASME, Vol. 111, pp. 78-86.
- Simonich, J.C., Bradshaw, R. (1978) "Effect of Free Stream Turbulence on Heat Transfer through a Turbulent Boundary Layer," ASME J of Heat Transfer, Vol. 100, pp. 671-677.
- Sinha, A.K., Bogard, D.G., and Crawford, M.E. (1991) "Film Cooling Effectiveness Downstream of a Single Row of Holes with Variable Density Ratio," ASME Journal of Turbomachinery, Vol. 113, No.3.
- Whan-Tong, J. (1991) "The Development of a Very High Freestream Turbulence Generator for Use in Gas Turbine Studies," Master's Thesis, University of Texas at Austin, Turbulence and Turbine Cooling Research Laboratory.

Bibliography

Ames, F.E. and Moffat, R.J. (1990a), "Effects of Simulated Combustor Turbulence on Boundary Layer Heat Transfer," AIAA/ASME Thermophysics and Heat Transfer Conference, Seattle, pp. 11-17.

Ames, F.E. and Moffat, R.J. (1990b), "Heat Transfer with High Intensity, Large Scale Turbulence: The Flat Plate Turbulent Boundary Layer and the Cylindrical Stagnation Point," Stanford University Report No. HMT-44.

Baines, W.D. and Peterson E.G. (1951), "An Investigation of Flow Through Screens," *Transactions of the ASME*, Vol. 73, pp. 467-480.

Blair, M.F. (1983), "Influence of Free-Stream Turbulence on Turbulent Boundary Layer Heat Transfer and Mean Profile Development, Part I - Experimental Data," *ASME J Heat Transfer*, Vol. 105, pp. 33-40.

Blair, M.F. and Bennett, J. C. (1987), "Conventional and Conditional Prandtl Number in a Turbulent Plane Wake," *International Journal of Heat and Mass Transfer*, Vol. 30, No. 10, pp 2023-2030.

Comte-Bellot G., Corrsin S. (1966), "The Use of a Contraction to Improve the Isotropy of Grid-Generated Turbulence," *Journal of Fluid Mechanics*, Vol. 25, Part 4, pp. 657-682.

Coughran, M.T. and Bogard, D. G., (1986), "An Experimental Study of the Burst Structure in a LEBU-Modified Boundary Layer," Tenth Symposium on Turbulence, Rolla, Missouri.

Hancock, P.E. and Bradshaw, P. (1982), "The Effect of Free-Stream Turbulence Boundary Layer Development," *ASME J Power Engineering*.

Hinze, J. O. (1975), *Turbulence*, 2nd ed., McGraw-Hill.

Kays, W. M., and Crawford M. E. (1980), *Convective Heat and Mass Transfer, Second Edition*, McGraw-Hill, New York.

MacArthur, C.D. (1986), "Fluid Dynamics and Heat Transfer of the Circular Tangential Wall Jet," Ph.D. Thesis, University of Dayton, Dayton, Ohio.

Maciejewski, Paul K. and Moffat, Robert J. (1989a), "Effects of Very High Turbulence on Heat Transfer," Seventh Symposium on Turbulent Shear Flows, Stanford University, August 21-23, 1989.

Maciejewski, P. K. and Moffat, R. J. (1989b), "Heat Transfer with Very High Free Stream Turbulence," Stanford University, Report HMT-42.

Pietrzyk J. R., Bogard, D. G., and Crawford, M.E. (1989), "Hydrodynamic Measurements of Jets in Crossflow for Gas Turbine Film Cooling Applications," *Journal of Turbomachinery*, Vol. 111, pp. 139-145.

Simonich, J.C., and Bradshaw, R. (1978), "Effect of Free Stream Turbulence on Heat Transfer through a Turbulent Boundary Layer," *ASME J of Heat Transfer*, Vol. 100, pp. 671-677.

Sinha, A.K., Bogard, D.G., and Crawford, M.E. (1991), "Film Cooling Effectiveness Downstream of a Single Row of Holes with Variable Density Ratio," *ASME Journal of Turbomachinery*, Vol. 113, No.3.

Subramanian, C. S. and Antonia, R. A. (1981), "Effect of Reynolds Number on a Slightly Heated Turbulent Boundary Layer," *International Journal of Heat and Mass Transfer*, Vol. 24, No. 11, pp. 1833-46.

Thole, K. A., Sinha, A. K., Bogard, D. G., Crawford, M. E., (1990), "Mean Temperature Measurements of Jets in Crossflow for Gas Turbine Film Cooling Application," presented at the Third International Symposium on Transport Phenomena and Dynamics of Rotating Machinery, Honolulu, Hawaii.

Thole, K. A., Whan-Tong, J., and Bogard, D.G. (1991), "Generation of Very High Freestream Turbulence Levels and the Effects on Heat Transfer," Eighth Symposium on Turbulent Shear Flows, Munich, Germany.

Whan-Tong, J. (1991), "The Development of a Very High Freestream Turbulence Generator for Use in Gas Turbine Studies," Master's Thesis, University of Texas at Austin, Turbulence and Turbine Cooling Research Laboratory.